Modeling the Deformation and Failure Behavior of FCC and HCP Nanocrystalline Materials

by

Yujie Wei

Bachelor of Science, Mechanics
Beijing University, China, 1997

Master of Science, Mechanics
Institute of Mechanics, Chinese Academy of Sciences, 2000

Submitted to the Department of Mechanical Engineering
in partial fulfillment of the requirements for the degree of

Doctor of Philosophy

at the

MASSACHUSETTS INSTITUTE OF TECHNOLOGY

June 2006

Author .....
Department of Mechanical Engineering
Feburary 28, 2006

Certified by.. .....
Lallit Anand
Professor
Thesis Supervisor

Accepted by ....
Lallit Anand
Chairman, Department Committee on Graduate Students

Modeling the Deformation and Failure Behavior of FCC and HCP Nanocrystalline Materials

by

Yujie Wei

Submitted to the Department of Mechanical Engineering
on Feburary 28, 2006, in partial fulfillment of the
requirements for the degree of
Doctor of Philosophy

Abstract

As foreseen by Richard Feynman in his famous talk titled *There's Plenty of Room at the Bottom* in 1959, scientists nowadays are miniaturizing structures in materials to achieve better performance as concerned in technical applications. Reducing grain sizes in polycrystalline materials into the range of less than 100nm, for example, could achieve extraordinary high strength in these so called nanocrystalline (nc) materials. The reduced grain size gives rise to new deformation mechanisms in nc materials. It is now widely accepted that there is a strong interplay between dislocation-based deformation in the crystalline grain interiors and the inelastic deformation mechanisms operative in the grain-boundary regions. Grain-boundary regions play an increasingly significant role as the grain size decreases below the 100nm level. In this dissertation, constitutive models have been developed to investigate the deformation mechanisms of nc materials, with focus on modeling grain-boundary decohesion in nc materials. Two micromechanical models have been developed to capture the deformation in grain boundaries in nc materials. To the end, a phenomenological constitutive model has been developed for powder-processed nc materials, where the plastic flow could be pressure-dependent, plastically-dilatant, and non-normal.

To model the deformation in grain boundaries, we made the assumption that the mechanical behavior of a grain boundary is governed by the interaction of two coupled surfaces of neighboring grains. Mechanical response due to the relative sliding and separation between the two coupled surfaces is represented by traction-separation laws. An isothermal, rate-independent elastic-plastic interface model has been developed, which accounts for both reversible elastic, as well as irreversible inelastic separation-sliding deformations at the interface prior to failure. The interface model, which represents the deformation in grain boundaries, is coupled with an isothermal, rate-independent crystal-plasticity model for grain interiors, and to study the deformation and fracture response of nc nickel.

Secondly, motivated by the fact that the ultimate size limit for nc materials would be bulk amorphous materials, we treated the non-equilibrium, more or less disordered grain boundaries in nc material as amorphous layers with finite thickness of $\approx$ 1nm.

A viscoplastic amorphous constitutive model is applied to capture the deformation in grain-boundary regions. The model has been applied to predict the mechanical behavior of nc nickel with different grain sizes and subject to tensile deformation at different strain-rates.

Many nanocrystalline materials are made by powder-consolidation; and their macroscopic response is reminiscent of cohesive granular materials. Based on the deformation behavior observed on powder consolidated nc materials from different groups, we have formulated a model for the response of pressure-sensitive and plastically-dilatant elastic-viscoplastic powder consolidated nc materials; where the plastic flow could be pressure-dependent, plastically dilatant, and non-normal.

Thesis Supervisor: Lallit Anand
Title: Professor

Acknowledgements

I would like to express my sincere gratitude to professor *Lallit Anand* for his academic parenting during my Ph.D. study. I have benifited so much from his training and impeccable standards on research.

I would also like to thank professor *David Parks*, professor *Raul Radovitzky*, and professor *Subra Suresh* for serving on my thesis committee, their encouragement and valuable suggestions on my research.

Many thanks to *Leslie Regan* and *Raymond Hardin* for their support, which always far exceeded administrative details; to *Pierce Hayward* for his technical support all the time; to Michael King for being such a nice TA partner.

I have enjoyed so much from hanging out and discussing with my friends and colleagues relating to academic problems, cultures and so on. I would like to acknowledge with gratitude the names of *Regina Cheung, Nuo Sheng, Suvrat Lele, Chris Gethering, Rajdeep Sharma, Theodora Tzianetopoulou, Prakash Thamburaja, Brian Paul Gearing, Adam Mulliken, Vikas Srivastava, Deepti Tewari, Sauri Gudlavalleti, Jin Yi, Yin Yuan, Yu Qiao, Hang Qi* and *Steve Xia.*

To *Nicoli Ames* - thank you for pushing me to improve my spoken English and your kind help for my research relating to experiments and computational facilities.

To *Cheng Su* and *Oliver Diard*, it is a pleasure to cooperate with your guys.

To *Yong Li, Gang Tan, Ronggui Yang* and *Yuetao Zhang*, I will miss our great time in Boston. Cheers to our future.

To My wife, *Min*, thanks for your continual support. My mama didn't get a chance to see my graduation. I miss you so much, mama.

This research was supported by the Defense University Research Initiative on NanoTechnology (DURINT) on "Damage- and Failure-Resistant Nanocrystalline and Interfacial Materials" which is funded at MIT by the Office of Naval Research under grant N00014-01-1-0808. Powder-consolidated nc-Mg samples supplied by professor Li Lu from National University of Singapore is gratefully acknowledged.

Contents

List of Figures

List of Tables

Chapter 1

Introduction

Recent research on the mechanical properties of materials has been driven in the direction of design and synthesis of special microstructures, through which major improvements in strength and toughness may be achieved. In nanocrystalline (nc) materials, where average grain sizes are usually less than 100 nanometers, a substantial increase in strength and hardness can be obtained (e.g., Gleiter 1989; Suryanarayana 1995; McFadden et al. 1999; Lu et al. 2000; Jeong et al. 2001; Shuh et al. 2002). The consequentially increased grain boundary volume in nc materials attributes new mechanical deformation behavior in nc metals, which is distinct from that of their conventional coarse-grained counterparts.

- Grain boundaries, known as barriers for slips of dislocations and being an important hardening mechanism in coarse-grained metals, may facilitate inelastic deformation instead in nc metals due to the nature that they are more disordered and loosely bonded compared with structures in crystallites. Considering the high strength and inevitable stress concentration in regions like triple junctions in nc materials, there may be direct grain-boundary sliding while nc materials are subject to deformation.

- Dislocations, the main carrier for plastic deformation in conventional coarse-grained metals, now are difficult to reside or be produced in grain interiors due to the physical constraint. Plastic deformation in grain interiors has to be

accommodated by intermittent emissions of perfect or partial dislocations from grain boundaries (Van Swygenhoven et al. 1998, 1999a,b, 2002; Schiøtz et al. 1999; Farkas et al. 2002; Derlet and Van Swygenhoven 2002).

In general, these potential alternative inelastic deformations, grain boundary sliding and decohesion, as well as the new mechanism for grain interior plastic deformation, give rise to enhanced rate sensitivity in most f.c.c. nc metals, as well as remarkably reduced ductility.[1]

1.1 Operative deformation mechanisms in nc materials

Except these efforts having been input for the synthesis of nc materials and their mechanical property characterizations, researchers are trying to understand the deformation mechanisms in nc materials. In particular, better understanding for grain boundary mechanics is helpful for further tailoring the microstructures during material synthesis, through which better mechanical properties could be achieved. A broad picture of the operative micromechanisms of inelastic deformation in this class of materials at low homogeneous temperature range is beginning to emerge. The following features of the operative micromechanisms are now reasonably widely-accepted (Hirth and Lothe, 1992; Van Swygenhoven et al., 1999a,b, 2002, 1998; Derlet and Van Swygenhoven, 2002; Farkas et al., 2002; Schiøtz et al., 1999; Lagerlöf et al., 2002; Yamakov et al., 2002; Chen et al., 2003; Kumar et al., 2003; Van Vliet et al., 2003; Sansoz and Molinari, 2004; Farkas et al., 2005; Wolf et al., 2005; Meyers et al., 2006):

- There is a strong interplay between dislocation-based deformation in the crystalline grain interiors and the inelastic deformation mechanisms operative in the grain-boundary regions.

[1] A brief introduction on the synthesis and mechanical property of nanocrystalline materials is supplied in Appendix C.

- Grain boundaries act as both sources and sinks for dislocations.

- Let Γ denote the stacking fault energy of the fcc material, G its nominal shear modus, and b the magnitude of the Burgers vector of a perfect dislocation, then there exists a critical grain size d_c given by $d_c \approx \frac{2}{3}\left(\frac{Gb^2}{\Gamma}\right)$, above which plastic deformation in nanocrystalline grain interiors occurs by the emission of *complete dislocations* from grain boundaries (seen in Fig. 1-1), and below which the plastic deformation occurs by *partial dislocations*. The partial dislocations produce stacking faults as they glide through the grains (Asaro et al. 2003; Zhu et al. 2005). Fig. 1-2 shows the movement of such a partial dislocation from its emission to transverse the whole grain in a molecular dynamics simulation.

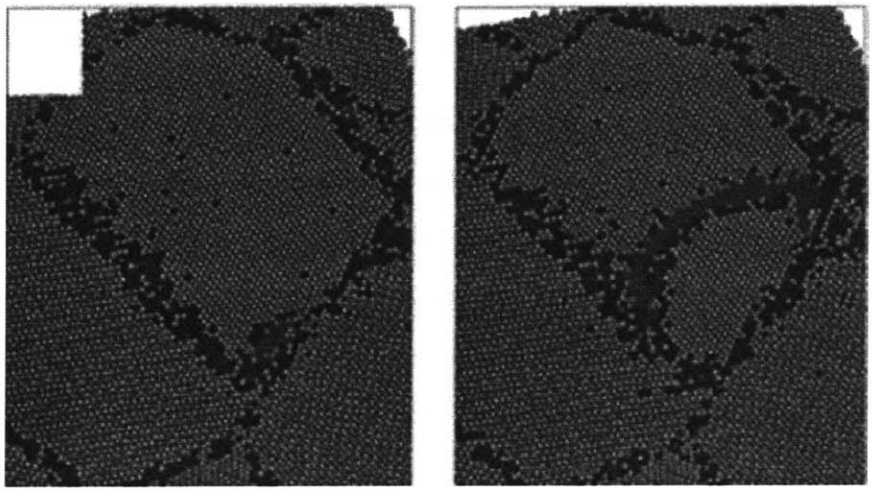

Figure 1-1: A full dislocation that nucleates locally at a grain boundary in nanocrystalline Al using the embedded atom potential for Al, Van Swygenhoven et al. (2004).

- The number of dislocations or stacking faults that need to traverse a typical grain in the nanocrystalline range to produce an overall strain of the order of 5% is quite small, typically less than 10 — 15. Thus, dislocation-based plasticity in the grain interiors is quite *discrete* in nature.

- When the grain size d becomes smaller than d_c, dislocation-based slip processes become less effective in producing overall inelastic deformation, and grain-boundary region based inelastic deformation mechanisms start to dominate.

(a) (b) (c)

Figure 1-2: MD simulation: 2D snapshots show the emission of a partial dislocation from the lower right triple junction and it swept the whole grain, Van Swygenhoven et al. (1999a).

- The grain-boundary inelastic deformation mechanisms are loosely called "grain-boundary sliding", but at low temperatures, atomistic simulations show this to be stress-activated *shear-shuffling* of atoms located in the intercrystalline regions, and the cooperative result of numerous such shear-shuffles leads to substantial overall shearing of the intercrystalline regions; the process is *not* dominated by thermal diffusion of atoms in the grain-boundary regions. As noted by Lund et al. (2004a), such a deformation mechanism is reminiscent of that in metallic glasses, where inelastic deformation occurs by local shearing of clusters of atoms — "shear transformation zones"; this shearing is accompanied by inelastic dilatation that produces strain-softening, which then leads to the formation of intense shear bands (Deng et al., 1989).

- Nanocrystalline fcc materials show a room-temperature strain-rate sensitivity which is almost an order of magnitude higher than their microcrystalline counterparts (Appendix C, Fig. C-5). The mechanisms underlying this enhanced strain-rate sensitivity are not fully understood at present, but it is probably due to the enhanced strain-rate sensitivity of the intercrsytalline grain-boundary regions, relative to the rate sensitivity of the crystalline grain interiors.

- The ductility of these materials, as measured by elongation in tensile experiments, is significantly reduced from the values observed for their microcrystalline counterparts, and seldom exceeds 5%. Since this occurs even for materials at the high end of grain sizes in the nanocrystalline range ($\sim$ 100 nm), one can infer that even though there is some accommodation of the overall imposed deformation by dislocation-mediated plasticity in the grain interiors, this accommodation is insufficient. Additional, *intergranular accommodation mechanisms* such as shear-failure, cavitation, and micro-cracking must be operative. It must be noted that widespread distributed grain-boundary damage prior to final macroscopic fracture has not been experimentally observed; however, atomistic simulation studies do show grain-boundary nano-void formation and decohesion leading to intergranular fracture in these materials (Farkas et al., 2002; Sansoz and Molinari, 2004; Farkas et al., 2005). Fig. 1-3 shows the snapshot of deformation in nc nickel using MD simulation. Grain boundary decohesion/cavitation is clearly observed.

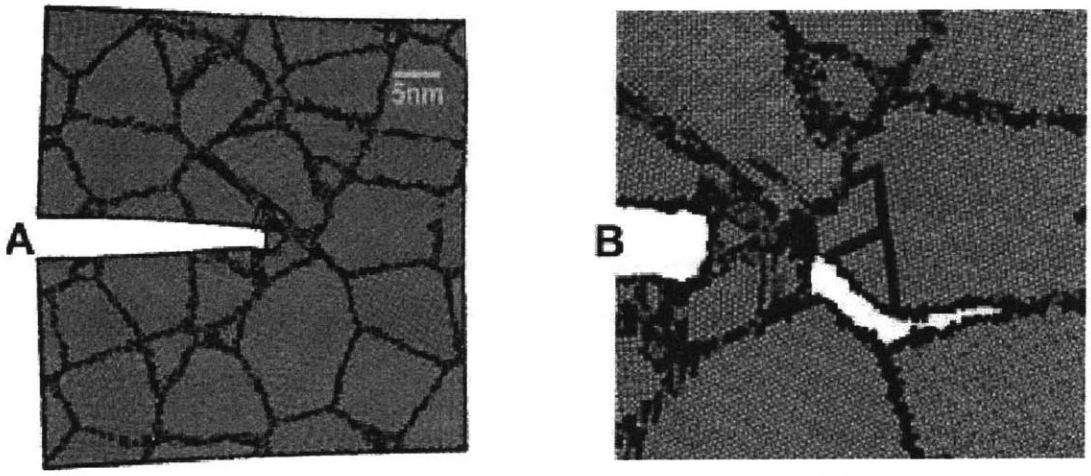

(a) (b)

Figure 1-3: Grain-boundary decohesion/cavitation in nanocrystalline nickel using MD simulation by Farkas et al (2002).

As reviewed in (Kumar et al., 2003; Wolf et al., 2005; Meyers et al., 2006), much of the understanding of the micromechanisms operative during the inelastic deformation of nanocrystalline materials has been obtained from the large-scale molecular

dynamics (MD) studies published in the past few years. Although such MD methods of studying atomic level mechanical response of materials are useful for gaining valuable insight, these methods are at present not suitable for carrying out simulations of deformation and failure under conditions similar to which physical experiments on nanocrystalline materials are carried out: i.e., macroscopic-sized specimens with complicated boundary conditions, involving realistic strain rates. MD simulations are inherently limited to small idealized microstructures and extremely high strain rates, typically $> 10^7/\text{s}$, which corresponds to a strain of 1% in 1 ns.

1.2 Modeling on nc materials: multiscale strategy

In contrast to MD methods, finite element methods (FEM) for simulation of micromechanical interactions and prediction of local as well as overall response of materials have been effectively used for a variety of composite material systems in recent years, and such methods do not possess the major limitations of the MD methods listed above. However, use of continuum-mechanical based FEM methods is contingent upon the assumptions of continuum mechanics — suitable smoothness of displacement fields, the notion of stress, and balance laws of linear and angular momentum — continuing to hold at the nanoscale. Further, just as the results from MD simulations depend crucially on the reliability of the interatomic potentials used in such studies, the results of FEM simulations depend crucially on the reliability of the continuum-level constitutive equations used in such analyses. While the concepts of continuum elasticity are expected to be approximately applicable at small scales approaching the nano-level, the concepts of classical continuum plasticity being applicable at this scale is highly questionable. Nevertheless, based on a *pragmatic engineering approach*, and bolstered by the success of (length-scale-independent) crystal-plasticity theories and attendant FEM simulation methodologies to represent grain-scale shear localization phenomena and texture evolution, a few investigators have recently carried out continuum-level FEM simulations of the inelastic deformation and failure response of nanocrystalline materials (Fu et al., 2001, 2004; Schwaiger et al., 2003;

Wei and Anand, 2004; Sansoz and Molinari, 2004). Although in their infancy, such FEM-based simulations provide valuable insights on the deformation and failure response of nanocrystalline materials, which cannot be obtained solely from atomistic simulations or experiments.

A plausible approach that can provide such quantitative predictions is to invoke the concept of a two-phase composite. This approach takes the view that, in a nano-grained material, the grain boundaries could occupy considerable volume and thus a nc material is more appropriately represented by a two-phase composite in which grains are represented by a single bulk phase and grain boundary by another phase. For example, Schwaiger et al. (2003) idealize a nanocrystalline material as a two-dimensional composite of hexagonal-shaped crystalline grain interiors, surrounded by grain boundary layers of finite thickness — a "core-and-mantle"-type model. In such a model, as the grain size is reduced, the ratio between the volume fractions of the grain boundary "mantle" and the crystalline "core" increases. The ratio of the finite grain boundary thickness to the grain diameter serves as the relative material length scale in the model, and gives rise to grain-size effects. Schwaiger et al. (2003) used an isotropic plasticity theory for the grain interiors as well as the grain-boundary regions. They assumed that (i) the thickness of the grain-boundary layer was $\sim$7 to 10 lattice parameters; (ii) the grain-boundary regions had a lower initial yield strength than the grain interiors; (iii) both the grain interior and grain-boundary regions were taken to strain harden isotropically; (iv) while the grain interior was modeled as rate-independent, the grain-boundary material was modeled to be strain-rate sensitive, with a strain-rate sensitivity parameter $m = 0.03$ in a standard power-law viscoplastic model. They also included a critical-plastic-strain-based criterion to model the initiation and progression of ductile failure. The focus of their study was the enhanced strain-rate sensitivity observed in nanocrystalline nickel relative to its microcrystalline counterpart, and their simple continuum level FEM model qualitatively reproduced the strain-rate sensitivity exhibited in the stress-strain curves from tension experiments on nanocrystalline Ni.[2]

[2]In passing we note that in light of the high resolution TEM micrographs of nanocrystalline

Fu et al. (2001, 2004) have also used a "core-and-mantle"-type model for nanocrystalline materials. In contrast to Schwaiger et al. (2003), in their most recent paper (Fu et al., 2004), in order to account for the elastic and plastic anisotropy in these materials, they model the grain interiors using a standard crystal-plasticity theory. Further, in order to represent the ease of dislocation generation at grain boundaries, the grain-boundary regions were modeled using either: (i) an isotropic plasticity model with a lower yield strength and more rapidly strain-hardening rate than the grain interior; and (ii) a crystal plasticity model with a lower initial crystal slip resistance, but a higher saturation shear strength than the slip resistance for the grain interior.[3] Their simulations show realistic looking distributions of inelastic deformation and shear localization in the polycrystalline aggregates. However, given the distinct diminution of dislocation activity in the nanocrystalline regime, their focus on variation of strain-hardening effects between grain interiors and grain-boundary regions, which can only arise when their are large number of dislocations to interact with each other, seems not to be physically well-founded for nanocrystalline materials, specially for the small grain-sizes in the nanocrystalline regime. Also, although they use a rate-dependent crystal-plasticity model, they do not report on the overall strain-rate sensitivity exhibited by their numerically-calculated stress-strain curves; however, this was not the focus of their study.

1.3 Thesis work

In this thesis work, I am going to present mesoscopic models we have developed to capture and further our understanding in the deformation mechanisms in nc materials. Two different strategies have been applied to model the competitive deformation in grain boundaries and grain interiors in nc materials.

materials, which show that for high-angle grain-boundaries, disordered grain-boundary regions are typically $\lesssim 1\,\text{nm}$ (Ranganathan et al., 2001), the use by Schwaiger et al. (2003) of a grain boundary affected zone of the order of 7 to 10 lattice parameter (lattice parameter of Ni $\equiv 0.352\,\text{nm}$), is not a realistic geometric representation of the microstructure of nanocrystalline materials.

[3]They also used a more complex model involving a continuous change in strain hardening from the grain interior to the grain boundary based on the spatial gradients in orientation of the maximum shear stress in the polycrystalline aggregate.

1.3.1 Single-crystal plasticity + Traction-separation law for GBs

In contrast to the "core-and-mantel"-type model, and given the uncertainties of ascribing a finite width to grain boundaries, We have developed an alternate modeling approach to account for the combined effects of grain-boundary-related deformation as well as dislocation-mediated plasticity within the grains. We have coupled a single-crystal plasticity constitutive model for the grain interior, with a new traction-separation constitutive model to account for grain-boundary sliding and separation phenomena. We recognized that a standard crystal plasticity model for the grain-interior deformation, which implicitly assumes enough dislocation nucleation and multiplication to result in a sufficiently smooth macroscopic response, is inadequate to represent the limited amount of inelastic deformation due to emission and eventual absorption of the relatively fewer (partial or complete) dislocations from grain boundaries in nanocrystalline materials. However, since elastic anisotropy and crystallographic texture effects are still important in nanocrystalline materials, and since the few dislocations in these materials are still expected to move on slip systems, the mathematical structure of a continuum crystal plasticity theory is still useful as an *indicator* of the limited inelasticity due crystalline slip within the nanocrystalline grains. Our cohesive interface model for grain boundaries accounts for both reversible elastic, as well irreversible inelastic sliding-separation deformations at the grain boundaries prior to failure. Details of the application is covered in Chap. 2.

1.3.2 Single-crystal plasticity + Amorphous GB

In our first modeling strategy, the tensile and shear properties of the cohesive grain boundaries were estimated by fitting results of numerical simulations to experimentally-measured stress-strain curves for electrodeposited nanocrystalline nickel. Unfortunately, such a fitting procedure makes it difficult to unambiguously characterize the grain boundary properties. In the published paper, we used a value for the shear strength of the grain boundaries which was very similar in magnitude to the tensile

strength of the boundaries; as is clear from the recent atomistic simulations of grain boundary response by Sansoz and Molinari (2004), this assumption is clearly unrealistic. Following the same methodology of us, Warner et al. (2006) have very recently used a continuum FEM method to model the plastic deformation of nanocrystalline copper by using crystal plasticity for the grain interiors and cohesive elements for grain boundaries. For the traction-separation relations for the grain boundaries, they obtained estimates for the shear and normal response of the boundaries from quasi-continuum atomistic calculations. Since their atomistic calculations were carried out at 0 K, they had to use apply a *large* ad-hoc *thermal-correction* (cf., their eq. (8)) to estimate the shear strength for the grain boundaries in Cu at room temperature. At this moment, all previous models have been restricted for the grain-interiors to be completely rate-independent.

As is clear from our brief statement, continuum-level FEM simulations of the inelastic deformation and failure response of nanocrystalline materials are still in their infancy. Much needs to be done to refine the constitutive models, specially for the grain boundary regions in "core-and-mantel"-type geometric representations of nanocrystalline materials, or the traction-separation relations in approaches using cohesive elements to represent grain-boundaries. Motivated by the fact that

- *amorphous metals are the ultimate limit for nanocrystalline metals, as the crystal grain size decreases to zero,*

and that

- *a new strain-rate-dependent continuum-plasticity theory for amorphous metals at low homologous temperatures is now available* (Anand and Su 2005; Su and Anand 2006),

we have developed slightly more refined constitutive models to represent the intercrystalline grain boundary regions, as well as the crystalline grain interiors in a "core-and-mantle" type approach to model the deformation and failure response of nanocrystalline materials. Specifically, we have

1. Developed a modified version of the rate-dependent amorphous plasticity model of Anand and Su (Anand and Su 2005; Su and Anand 2006) to account for cavitation and related-failure phenomena, and used such a model to represent the grain-boundary response of nanocrystalline materials.

2. Accounted for the transition from partial dislocation to complete dislocation mediated plasticity for the grain interiors. This development is based on the recent work of Zhu et al. (2005).

1.3.3 Powder consolidated nc materials

Impressive properties have also been recently been reported for powder-consolidated nanocrystalline Mg-based materials by Lu et al. (Lu et al., 2004a). [4] Samples of their nc-Mg-5%Al-1%Nd alloy were kindly provided to us by Prof. Li Lu of the National University of Singapore, and we conducted TEM microscopy, and performed some standard tension and compression experiments on their material. The nc-magnesium alloy produced in such a way has an average grain-size of around 90nm and shows significant increase in strength and an acceptable ductility compared with the conventional grain sized Mg alloys. The nc-magnesium also has an outstanding yield strength over density ratio, (σ_y/ρ), compared with most other nc-materials, as seen in Table 1.1. Comparison for mechanical and deformation behaviors between coarse-grained magnesium alloy AZ31B and the nanostructured magnesium alloy indicate that: The strength of this material is substantially increased due to grain refinement without loss of ductility; There is little initial texture in this materials. The strength asymmetry existing in extruded conventional grain sized magnesium alloy disappears. The powder consolidated nc magnesium could be treated as *isotropic material* reasonably. In the stress-strain curve, there is a hardening region followed by strain

[4]These authors have developed nanostructured Mg alloys of nominal composition Mg-5%Al-x%Nd, with x=0.5%, 1%, and 5% by weight. A typical processing schedule used by these authors is to first mechanically-alloy the Mg, Al and Nd powders. The mechanically-alloyed powders are then cold-compacted into cylinders of 35mm diameter, and sintered at 400 C or 500 C in a vacuum furnace for 2 hours. The sintered cylinders are then extruded at 400 C with an extrusion ratio of 25:1. For additional processing details see (Lu et al., 2004a).

nano-crystalline	ρ Mg/m^3	E (GPa)	σ_y (MPa)	E/ρ	σ_y/ρ	grain size (nm)
n-Cu	8.9	107±10	800	14	~ 90	20~40
n-Ni	8.7	192±20	1150	28	~130	28
ufg-Al	2.7	69±7	135	24	~ 50	250
n-Mg	1.8	43±5	400	25	~222	90

Table 1.1: Some mechanical properties of nc-metals

softening which might due to the free volume evolution in this material. Overall, the mechanical and deformation behavior in powder consolidated nc-Mg revealed by experiments are analogous to those of cohesive granular materials.

With the current synthesis capability, the emerging engineering applications of those powder consolidated nc materials necessitate the development of continuum models which could be applied at a design level for those materials. Motivated by the observed mechanical properties of powder-consolidated nc metals and their deformation mechanisms from literature, as well as our own experiments on powder consolidated nc magnesium , we have develop a thermodynamically-consistent and frame-indifferent (Anand and Gurtin, 2003) model for the large deformation (Weber and Anand, 1990) response of pressure-sensitive and plastically-dilatant elastic-viscoplastic materials which may be idealized to be isotropic, and apply the model to represent the response of powder-consolidated nc metals.

1.3.4 Application of the interface model to adhesively bonded structure

The new interface model that we have developed accounts for both reversible elastic, *as well as irreversible inelastic separation-sliding* deformations at the interface prior to failure. It could be applied to lots of mechanical structures with embedded *interfaces*. As one application of the model, we have considered the widely studied problem of modelling the behavior of adhesively-bonded components. We show that our new model, when suitably calibrated against a suite of experiments to deter-

mine the constitutive parameters in the interface model for aluminum components bonded by a polymeric adhesive, is able to reasonably-well predict the macroscopic load-displacement curves of several different verification experiments: four-point bend tests, peel tests, and single- and double-lap joint tests. This part of work has included in Appendix A.

1.4 Summary

In this thesis, we have developed two micromechanical modeling strategies to capture the competing deformation in grain interiors and grain boundaries of nc materials. In the first method, mechanical response due to the relative sliding and separation between two grains is represented by traction-separation laws. An isothermal, rate-independent elastic-plastic interface model has been developed, which accounts for both reversible elastic, as well as irreversible inelastic separation-sliding deformations at the interface prior to failure. Secondly, motivated by the fact that the ultimate size limit for nc materials would be bulk amorphous materials, we treated the non-equilibrium, more or less disordered grain boundaries in nc material as amorphous layers with finite thickness of $\approx$ 1nm. A viscoplastic amorphous constitutive model is applied to capture the deformation in grain-boundary regions.

The micromechanical models have been applied to investigate the deformation behavior in fcc nc materials. To the end,

(i) we have developed critical understanding on the deformation of nanocrystalline materials: the competing deformation mechanism in grain boundaries and grain interiors, the influence of microstructure and testing condition upon the mechanical response. Investigation is focusing on grain sizes where grain interior plastic deformation and grain boundary deformation contribute competitively to accommodate applied boundary conditions.

(ii) The micromechanical models bridged the modeling from atomistic scale to macroscopic continuum level. In the foreseen future, such a modeling strat-

egy should be the main methods in the modeling of nanocrystalline materials with the laboratory attainable time and length scales.

(iii) The developed micromechanical models could be applied to many mechanical structures with interface/grain boundary embedded, where the interfaces/grain boundaries might be the main issue for the mechanical or thermal liability of the integrated systems.

The capability to produce bulk nc materials makes the engineering application of these material to be possible. It is hence desired to develop macroscopic continuum model which could be applied for the design of structures made from bulk nc materials. Many nanocrystalline materials are made by powder-consolidation; and their macroscopic response is reminiscent of cohesive granular materials. We have formulated a model for the response of pressure-sensitive and plastically-dilatant elastic-viscoplastic powder-consolidated nc materials; where the plastic flow could be pressure-dependent, plastically dilatant, and non-normal. The model captures the mechanical and deformation behavior of such type of materials quite well and could be applied for the engineering design of powder-consilidated nc materials.

Chapter 2

Grain-boundary sliding and separation in polycystalline metals: application to nc f.c.c. metals

2.1 Introduction

It is well known that in polycrystalline metals, a substantial increase in strength and hardness can be obtained by reducing the grain size to the nanometer scale (e.g., Gleiter 1989; Suryanarayana 1995; McFadden et al. 1999; Jeong et al. 2001; Shuh et al. 2002; Lu et al. 2000). These attributes have generated considerable interest in the use of nanocrystalline (nc) metallic materials (grain sizes less than $\approx$ 100 nm), for a wide variety of structural applications. The hardness, stiffness, strength and ductility of some nc-fcc metals (e.g., Cu, Ni), as measured by microindentation and simple tension experiments, have been reported in the recent literature, (Nieman et al. 1989; Sanders et al. 1997; Ebrahami et al. 1998, 1999; Legros et al. 2000; Lu et al. 2001; Torre et al. 2002). Typically, relative to their microcrystalline counterparts, nc metals exhibit a high yield strength and a high strain-hardening rate leading to a very high tensile strength, but at the expense of a much reduced tensile ductility.

[1]The work in this chapter is published in *J. Mech. Phys. Solids*, by Wei and Anand, 2004, **52**, 2587.

The limited ductility is of major concern. For example, while the ultimate tensile strength levels approach $\approx$ 1500 MPa in electro-deposited nc Ni, the ductility that can be obtained in this material is generally low and usually does not exceed $\approx$ 3%, Torre et al. (2002). The reduced ductility at room temperature is observed in many, if not most, of the nc metals synthesized using existing methods, which include (a) gas-phase condensation of particulates and consolidation, (b) mechanical alloying and compaction, (c) severe plastic deformation, and (d) electrodeposition. The reduced ductility is believed to be mainly due to pre-existing flaws, such as impurities and porosity introduced during the processing of nc materials. Nc metals produced by

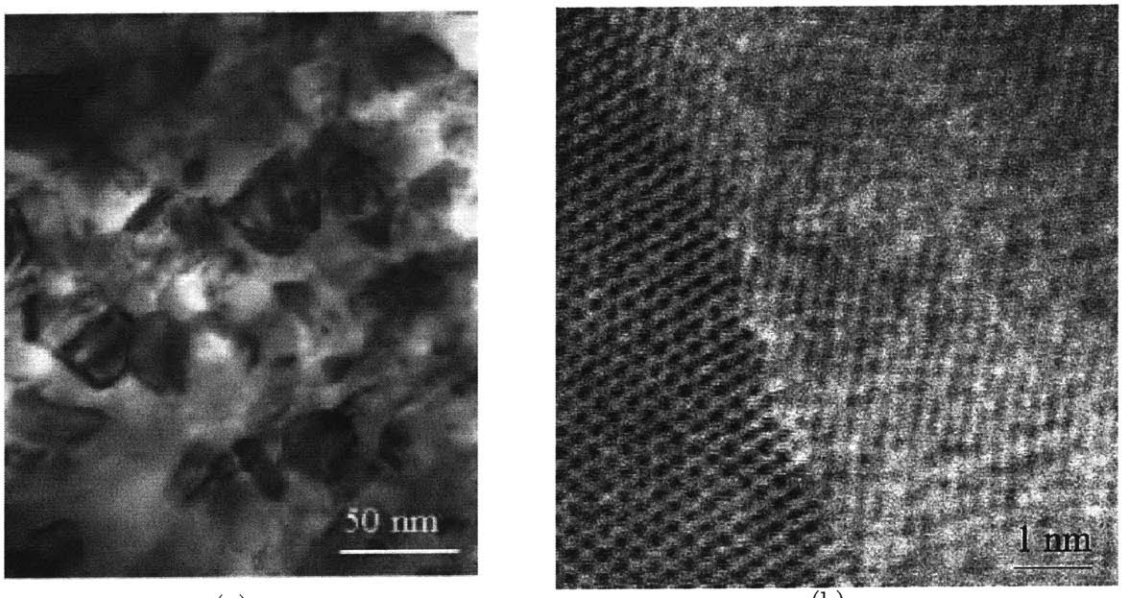

(a) (b)

Figure 2-1: As-received electrodeposited nc-Ni: (a) Bright field TEM image showing nc grain structure. (b) Image showing a clean atomically-faceted grain boundary. From Kumar et al. (2003).

electrodeposition methods are expected to have a fully-dense as-deposited structure, but as mentioned above, this material also shows a limited ductility (Torre et al., 2002). Kumar et al. (2003) have recently reported on an extensive set of experiments that they conducted to observe the deformation mechanisms in electro-deposited nc Ni both after and during deformation using transmission electron microscopy (TEM). Briefly, they concluded

- That the grain interiors of their as-received electro-deposited nc Ni (average

grain size of 30 nm) were clean and (almost) devoid of dislocations, and that the grain boundaries did not contain any amorphous layers or second-phase particles, or nano-scale voids; Fig. 2-1.

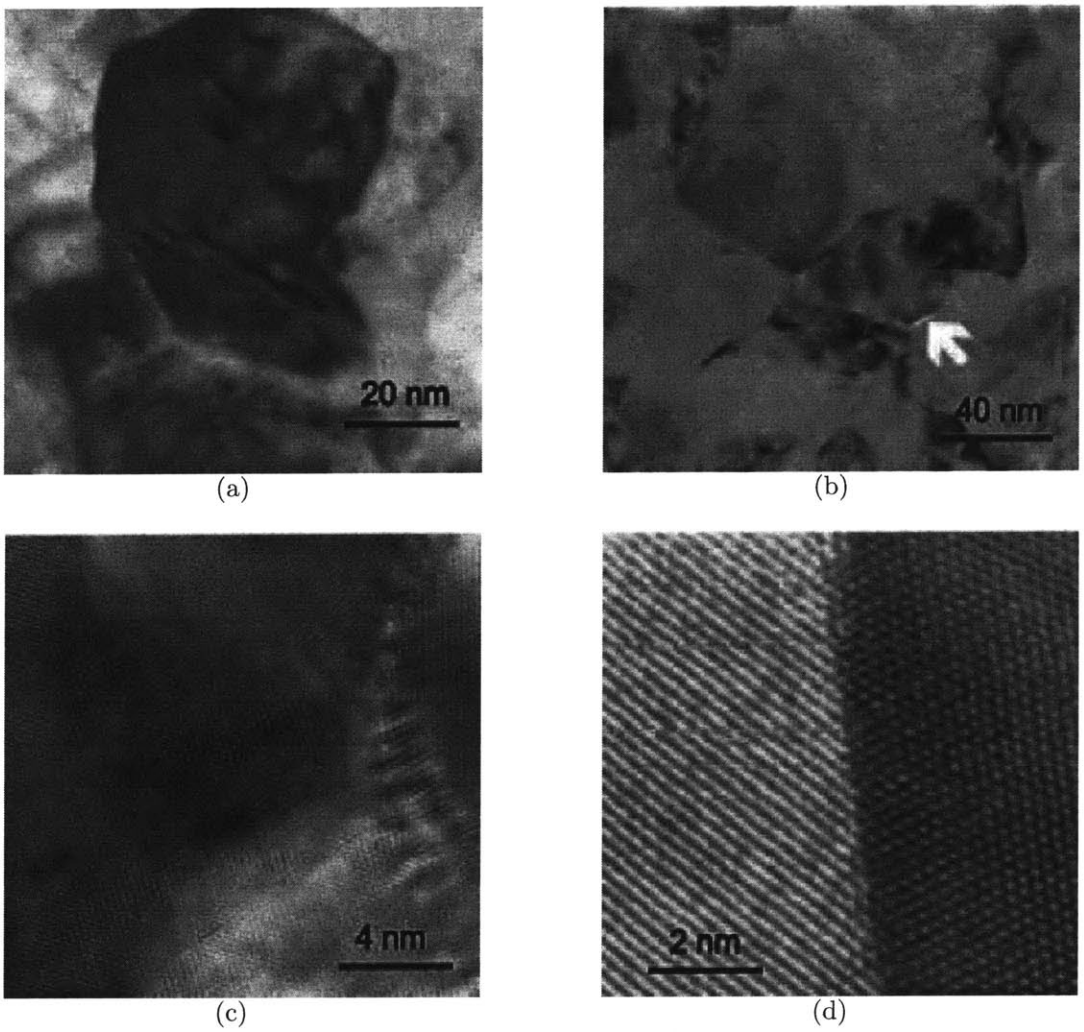

Figure 2-2: Microstructure of nc-Ni after 4% plastic strain in compression: (a) Bright field TEM image showing a few dislocations within a grain. (b) A possible crack at a grain-boundary triple junction. (c) Substantially dislocation-free grains and possibly a low-angle grain boundary. (d) Clean grain boundaries with no evidence of residual dislocation debris left after the deformation. From Ḳumar et al. (2003).

- Observations of specimens which were first deformed by compression, rolling or nano-indentation, and then examined by TEM indicated that while isolated dislocations, infrequent dislocation networks, and some dislocation debris were seen within grains, the density of dislocations visible in the specimens after the

deformation could not account for the macroscopically-imposed plastic strains; Fig. 2-2 shows the microstructure of nc-Ni after 4% strain in compression.

- Observations of tensile specimens which contained perforations in the center of their gage sections and which were incrementally strained in discrete steps in-situ in a transmission electron microscope, provided evidence of nucleation and growth of grain-boundary cracks and triple junction voids ahead of a growing crack (which had nucleated from the perforation), as well as substantial dislocation activity in the interiors of the grains adjacent to the crack front; Fig. 2-3. That is, *the nucleation and growth of grain-boundary slip and separation, together with dislocation-based plasticity in the interior of grains adjacent to the propagating crack, are the dominant mechanisms of inelastic deformation in the "process-zone" associated with the tip of a crack in nc Ni.* As a caution, it is worth noting that in-situ deformation of a perforated thin foil specimen in a TEM is not always representative of mechanical response of a bulk specimen.

Atomistic computer simulations of nc metals (particularly for Ni and Cu) have also been widely reported in the recent literature, e.g., El-Sherik and Erb 1995; Schiøtz et al. 1998; Van Swygenhoven et al. 1998; Schiøtz et al. 1999; Van Swygenhoven et al. 1999a,b; Yamakov et al. 2001; Farkas et al. 2002; Van Swygenhoven et al. 2002. *These atomistic simulations collectively show that as the grain size decreases, intragranular plasticity driven by dislocation mechanisms becomes more difficult at nanometer-scale grain sizes, and that the macroscopically-imposed deformation is accommodated by grain-boundary sliding and separation.* Again, we note that since atomistic calculations involve only a limited number of grains and nearly instantaneous (in a matter of picoseconds) loading, they only provide a qualitative understanding of the real mechanical response of materials at laboratory length and time-scales.

Thus, from the physical experiments and atomistic simulations reported in the literature, it is clear that grain-boundary-related slip and separation phenomena begin to play an important role in the overall inelastic response of a polycrystalline material when the grain-size decreases to diameters under $\approx 100\,\text{nm}$, and dislocation activity

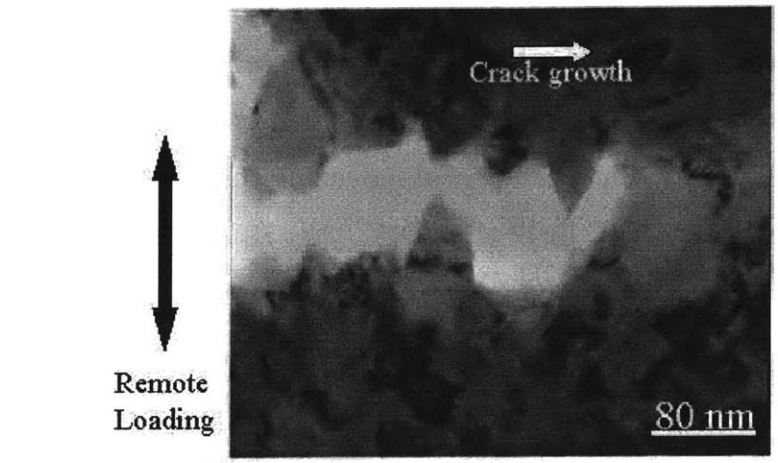

(a)

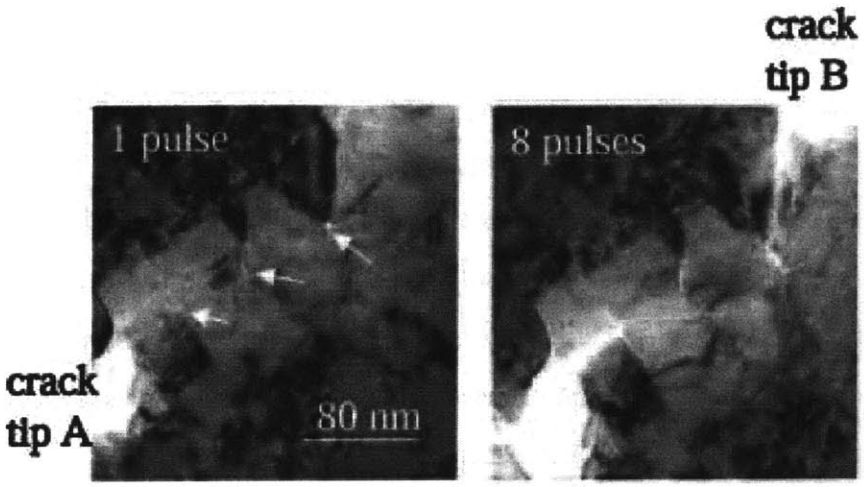

(b)

Figure 2-3: Microstructure of a perforated nc-Ni tensile specimen deformed in-situ in an electron microscope: (a) A bright field image of an advancing crack. The image shows a saw-tooth crack which runs along grain boundaries, and also often across grains that have necked-down plastically. (b) A pair of "freeze-frame" images showing the microstructural evolution and progression of damage with increases in the applied displacement pulses; grain-boundary cracks and triple junction voids are indicated by arrows. These cracks and voids have grown after 8 pulses. Subsequent images (not shown here) also indicate dislocation emission from the tip of crack B. From Kumar et al. (2003).

within the grain interiors becomes more difficult. One possible computationally-tractable modelling approach to account for the combined effects of grain-boundary-related deformation as well as plasticity within the grains, is to couple a single-crystal plasticity constitutive model for the grain interior with an appropriate cohesive interface constitutive model to account for grain-boundary sliding and separation phenomena. The only other numberical modelling that includes grain boundary slip on the continuum level is by Fu et al. (2001). They idealized a polycrystalline material as a composite with isotropic flow stress in grain interiors and a grain boundary layer with high hardening rate behavior. By varying the volume fraction of grain boundaries with the variance of grain size, their model can account for the Hall-Petch effect.

The purpose of this chapter is to couple the isothermal, rate-independent elastic-plastic interface model (Appendix A) which accounts for both reversible elastic, as well as irreversible inelastic separation-sliding deformations at the interface prior to failure with an isothermal, rate-independent crystal-plasticity model for the grain interior, and to use the new computational capability to study the deformation and fracture response of an aggregate of crystals. [1] Such a computational capability may serve as a *meso-scale simulation tool* to study the deformation and fracture response of polycrystals whose individual crystals may be in the $\leq 100\,\text{nm}$ size range. Since our model will not contain an inherent length scale, it may of course also be used for polycrystals with grains in any other larger size range.

The plan of this chapter is as follows. In § 2.2 we develop our rate-independent *interface constitutive model.* In § 2.3 we summarize the crystal-plasticity model that we shall use in this chapter. In § 2.4 we first estimate the material parameters in the model for nc Ni from the limited stress-strain curves available in the literature, and then show some representative simulations of the deformation and damage evolution in a quasi-three-dimensional columnar-grained textured polycrystalline aggregates. The effects of a variation of the grain-size on the macroscopic stress-strain curve, as predicted by the continuum model, are discussed in § 2.5. Results from a numerical

[1] Nc metallic materials do exhibit a rate-sensitive response at room temperature, but it is typically quite small for nc nickel at strain rate ranging from $5.5 \times 10^{-5} - 5.5 \times 10^{-2}/\text{s}$, (Torre et al., 2002).

experiment showing the development of fracture in a notched nc-Ni specimen are shown in § 2.6. We close in § 2.7 with some final remarks.

2.2 Interface constitutive model

Cohesive interface modelling of fracture started more than 40 years ago with the work of Barenblatt (1959) and Dugdale (1960). In recent years, cohesive surface models have been widely used to numerically simulate fracture initiation and growth by the finite-element method (cf., e.g., Needleman 1990; Xu and Needleman 1994; Camacho and Ortiz 1996), for a recent review see Hutchinson and Evans (2000). Typically, a cohesive interface is introduced in a finite element discretization of the problem by the use of special interface elements which obey a non-linear interface traction-separation constitutive relation which provides a phenomenological description for the complex microscopic processes that lead to the formation of new traction-free crack faces. The loss of cohesion, and thus of crack nucleation and extension, occurs by the progressive decay of interface tractions. The interface traction-separation relation usually includes a cohesive strength and cohesive work-to-fracture. Once the local strength and work-to-fracture criteria across an interface are met, decohesion occurs naturally across the interface, and traction-free cracks form and propagate along element boundaries. Although substantial progress has been made in recent years, there are still several key issues that need to be addressed in the modelling of cohesive interfaces. Specifically: (i) Most previous interface models are of the *non-linear reversible elastic* type. For example, in Xu and Needleman (1994), with $\boldsymbol{\delta}$ denoting the displacement jump across the cohesive surface, and $\mathbf{t}$ the work-conjugate traction vector on the surface, the constitutive equation for the cohesive surfaces is expressed in terms of a potential function φ, such that the traction $\mathbf{t} = \partial\varphi/\partial\boldsymbol{\delta}$. The specific form for φ chosen by Xu and Needleman (1994) is history- and rate-independent, and this leads to a traction-displacement relation which is fully reversible. There exists a need to develop interface constitutive models which allow for *inelasticity* at the interface prior to failure, much in the spirit of elastic-plastic constitutive equations which gov-

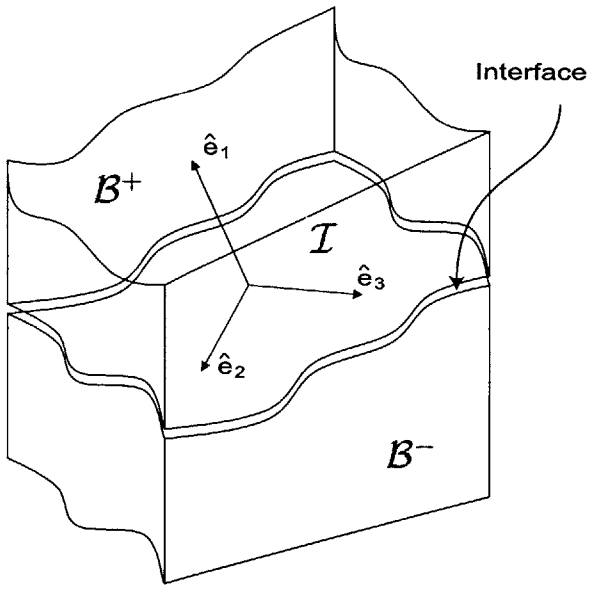

Figure 2-4: Schematic of interface between two bodies $\mathcal{B}^+$ and $\mathcal{B}^-$.

ern the deformation of the bulk material.[2] (ii) While it is relatively straightforward to construct a traction-separation relation for normal separation across an interface, appropriate relations for combined opening and sliding are less well-developed. With a view towards modeling grain-boundary interface response, in what follows we develop an elastic-plastic interface model which accounts for both reversible elastic, as well irreversible inelastic separation-sliding deformations at the interface prior to failure. We consider two bodies $\mathcal{B}^+$ and $\mathcal{B}^-$ separated by an interface $\mathcal{I}$ (Fig. 2-4). Let $\{\hat{\mathbf{e}}_1, \hat{\mathbf{e}}_2, \hat{\mathbf{e}}_3\}$ be an orthonormal triad, with $\hat{\mathbf{e}}_1$ aligned with the normal $\mathbf{n}$ to the interface, and $\{\hat{\mathbf{e}}_2, \hat{\mathbf{e}}_3\}$ in the tangent plane at the point of the interface under consideration.

Let $\boldsymbol{\delta}$ denote the displacement jump across the cohesive surface, and $\mathbf{t}$ the power-conjugate traction, such that $\mathbf{t} \cdot \dot{\boldsymbol{\delta}}$ gives the power per unit area of the interface in the reference configuration.

We assume that the displacement jump may be additively decomposed as

$$\boldsymbol{\delta} = \boldsymbol{\delta}^e + \boldsymbol{\delta}^p, \tag{2.1}$$

[2]Camacho and Ortiz (1996) do allow for a form of inelasticity. They consider interface constitutive equations in which the initial cohesive response is rigid, and there is a finite traction at which softening occurs; they also allow loading/unloading irreversibility, with linear unloading to the origin.

where $\boldsymbol{\delta}^e$ and $\boldsymbol{\delta}^p$, respectively, denote the elastic and plastic parts of $\boldsymbol{\delta}$. Then,

$$\mathbf{t} \cdot \dot{\boldsymbol{\delta}} = \mathbf{t} \cdot \dot{\boldsymbol{\delta}}^e + \mathbf{t} \cdot \dot{\boldsymbol{\delta}}^p. \tag{2.2}$$

Let φ denote a free-energy per unit surface area in the reference configuration. We consider a purely mechanical theory based on the following local energy imbalance that represents the first two laws of thermodynamics under isothermal conditions,

$$\dot{\varphi} \leq \mathbf{t} \cdot \dot{\boldsymbol{\delta}}. \tag{2.3}$$

Then, using (2.2), the field

$$\Gamma = \mathbf{t} \cdot \dot{\boldsymbol{\delta}}^e + \mathbf{t} \cdot \dot{\boldsymbol{\delta}}^p - \dot{\varphi} \geq 0 \tag{2.4}$$

represents the *dissipation rate* per unit area.

We assume that the free-energy φ is given by

$$\varphi = \hat{\varphi}(\boldsymbol{\delta}^e). \tag{2.5}$$

Then, using standard arguments, (2.4) gives

$$\mathbf{t} = \frac{\partial \hat{\varphi}(\boldsymbol{\delta}^e)}{\partial \boldsymbol{\delta}^e}, \tag{2.6}$$

and

$$\Gamma = \mathbf{t} \cdot \dot{\boldsymbol{\delta}}^p \geq 0. \tag{2.7}$$

We are concerned with interfaces in which the elastic displacement jumps are small. For these conditions we assume a simple quadratic free-energy φ

$$\varphi = \frac{1}{2} \boldsymbol{\delta}^e \cdot \mathbf{K} \boldsymbol{\delta}^e, \tag{2.8}$$

with $\mathbf{K}$, the interface elastic stiffness tensor, taken to be positive definite. In this case

(2.6) gives

$$\mathbf{t} = \mathbf{K}\boldsymbol{\delta}^e = \mathbf{K}(\boldsymbol{\delta} - \boldsymbol{\delta}^p). \tag{2.9}$$

We consider an interface model which is *isotropic* in its tangential response, and take $\mathbf{K}$ to be given by

$$\mathbf{K} = K_N \mathbf{n} \otimes \mathbf{n} + K_T(\mathbf{1} - \mathbf{n} \otimes \mathbf{n}), \tag{2.10}$$

with $K_N > 0$ and $K_T > 0$ normal and tangential elastic stiffness moduli.

The interface traction $\mathbf{t}$ may be decomposed into normal and tangential parts, $\mathbf{t}_N$ and $\mathbf{t}_T$, respectively, as

$$\mathbf{t} = \mathbf{t}_N + \mathbf{t}_T, \quad \mathbf{t}_N \equiv (\mathbf{n} \otimes \mathbf{n})\, \mathbf{t} = (\mathbf{t} \cdot \mathbf{n})\, \mathbf{n} \equiv t_N \mathbf{n} \quad \mathbf{t}_T \equiv (\mathbf{1} - \mathbf{n} \otimes \mathbf{n})\, \mathbf{t} = \mathbf{t} - t_N \mathbf{n}. \tag{2.11}$$

The quantity t_N represents the *normal stress* at the interface. We denote the magnitude of the tangential traction vector $\mathbf{t}_T$ by

$$\bar{\tau} \equiv \sqrt{\mathbf{t}_T \cdot \mathbf{t}_T}\,, \tag{2.12}$$

and call it the *effective tangential traction*, or simply the *shear stress*.

We take the elastic domain in our rate-independent elastic-plastic model to be defined by the interior of the intersection of two convex yield surfaces. The yield functions corresponding to each surface are taken as

$$\Phi^{(i)}(\mathbf{t}, s^{(i)}) \leq 0, \qquad i = 1, 2, \tag{2.13}$$

and henceforth we indentify the index $i = 1$ with a "normal" mechanism, and the index $i = 2$ with a "shear" mechanism. The scalar internal variable $s^{(1)}$ represents the deformation resistance for the normal mechanism, and $s^{(2)}$ represents the deformation resistance for the shear mechanism. In particular, we consider the following simple

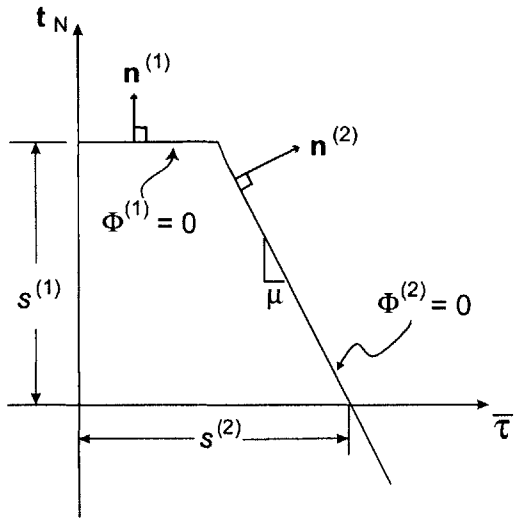

Figure 2-5: Schematic of yield surfaces for the normal and shear mechanisms.

specific functional form for the yield functions:

$$\Phi^{(1)} = t_N - s^{(1)} \leq 0, \qquad \Phi^{(2)} = \bar{\tau} + \mu t_N - s^{(2)} \leq 0, \tag{2.14}$$

where μ represents a *friction coefficient.* The surface $\Phi^{(i)} = 0$ denotes the ith yield surface in traction space, and

$$\mathbf{n}^{(1)} = \frac{\partial \Phi^{(1)}}{\partial \mathbf{t}} = \mathbf{n}, \qquad \mathbf{n}^{(2)} = \frac{\partial \Phi^{(2)}}{\partial \mathbf{t}} = \frac{1}{\sqrt{1+\mu^2}}\left(\frac{\mathbf{t}_T}{\bar{\tau}} + \mu \mathbf{n}\right) \tag{2.15}$$

denote the outward unit normals to the yield surface at the current point in traction space; see Fig. 2-5.

The equation for $\dot{\boldsymbol{\delta}}^p$, the *flow rule*, is taken to be representable as a sum of the contribution from each mechanism

$$\dot{\boldsymbol{\delta}}^p = \sum_{i=1}^{2} \nu^{(i)} \mathbf{m}^{(i)}, \qquad \nu^{(i)} \geq 0, \qquad \nu^{(i)} \Phi^{(i)} = 0, \quad \text{with} \tag{2.16}$$

$$\mathbf{m}^{(1)} = \mathbf{n}, \qquad \text{and} \qquad \mathbf{m}^{(2)} = \frac{\mathbf{t}_T}{\bar{\tau}}. \tag{2.17}$$

Note that since $\mathbf{m}^{(2)} \neq \mathbf{n}^{(2)}$, we have a *non-normal* flow rule for the shear response.

The evolution equations for the internal variables $s^{(i)}$ are taken as a pair of ordinary differential equations

$$\dot{s}^{(i)} = \sum_{j=1}^{2} h^{(ij)} \nu^{(j)}, \tag{2.18}$$

where the coefficients $h^{(ij)}$ denote hardening/softening moduli.

Finally, during inelastic deformation, an active mechanism must satisfy the *consistency condition*

$$\nu^{(i)} \dot{\Phi}^{(i)} = 0 \qquad \text{when} \qquad \Phi^{(i)} = 0. \tag{2.19}$$

The consistency condition serves to determine the inelastic deformation rates $\nu^{(i)}$ when inelastic deformation occurs. Straightforward calculations using (2.9) – (2.18) give

$$\dot{\Phi}^{(i)} = \mathbf{n}^{(i)} \cdot \mathbf{K}\dot{\boldsymbol{\delta}} - \sum_{j} \left[\mathbf{n}^{(i)} \cdot \mathbf{K}\mathbf{m}^{(j)} + h^{(ij)} \right] \nu^{(j)}.$$

For $\nu^{(i)} > 0$, when $\Phi^{i} = 0$ the consistency condition requires that $\dot{\Phi}^{(i)} = 0$. This gives the following system of linear equations for $\nu^{(i)} > 0$:

$$\sum_{j=1}^{2} A^{(ij)} \nu^{(j)} = b^{(i)}, \qquad A^{(ij)} = \mathbf{n}^{(i)} \cdot \mathbf{K}\mathbf{m}^{(j)} + h^{(ij)}, \qquad b^{(i)} = \mathbf{n}^{(i)} \cdot \mathbf{K}\dot{\boldsymbol{\delta}}. \tag{2.20}$$

We assume that *the matrix A is invertible*, so that the $\nu^{(j)}$ are uniquely determined.

Specific form for the evolution equations

Let

$$\gamma^{(1)} \stackrel{\text{def}}{=} \int_0^t \nu^{(1)}(\xi)\, d\xi, \tag{2.21}$$

$$\gamma^{(2)} \stackrel{\text{def}}{=} \int_0^t \nu^{(2)}(\xi)\, d\xi, \tag{2.22}$$

define equivalent relative plastic displacements for the two individual mechanisms, and

$$\bar{\gamma} \stackrel{\text{def}}{=} \sqrt{(\gamma^{(1)})^2 + \alpha\,(\gamma^{(2)})^2} \tag{2.23}$$

defines a combined *equivalent relative plastic displacement*, where α represents a *coupling parameter* between the normal and shear mechanisms.

A simple set of evolution equations for $s^{(1)}$ and $s^{(2)}$ which represent strain-hardening response until a critical value of $\bar{\gamma} = \bar{\gamma}_c$ is reached, and a *softening response* thereafter is

$$s^{(1)} = \hat{s}^{(1)}(\bar{\gamma}), \qquad \text{with} \qquad \hat{s}^{(1)}(\bar{\gamma}) = \begin{cases} \hat{s}^{(1)}_{hard}(\bar{\gamma}) & \text{if } \bar{\gamma} \le \bar{\gamma}_c, \\ \hat{s}^{(1)}_{soft}(\bar{\gamma}) & \text{if } \bar{\gamma} > \bar{\gamma}_c \text{ and } s^{(1)} > 0. \end{cases} \tag{2.24}$$

Similarly,

$$s^{(2)} = \hat{s}^{(2)}(\bar{\gamma}), \qquad \text{with} \qquad \hat{s}^{(2)}(\bar{\gamma}) = \begin{cases} \hat{s}^{(2)}_{hard}(\bar{\gamma}) & \text{if } \bar{\gamma} \le \bar{\gamma}_c, \\ \hat{s}^{(2)}_{soft}(\bar{\gamma}) & \text{if } \bar{\gamma} > \bar{\gamma}_c \text{ and } s^{(2)} > 0. \end{cases} \tag{2.25}$$

In this case

$$\dot{s}^{(1)} = \frac{\partial\,\hat{s}^{(1)}}{\partial\,\bar{\gamma}}\dot{\bar{\gamma}} = \frac{1}{\bar{\gamma}}\frac{\partial\,\hat{s}^{(1)}}{\partial\,\bar{\gamma}}\Big(\gamma^{(1)}\nu^{(1)} + \alpha\gamma^{(2)}\nu^{(2)}\Big), \tag{2.26}$$

$$\dot{s}^{(2)} = \frac{\partial\,\hat{s}^{(2)}}{\partial\,\bar{\gamma}}\dot{\bar{\gamma}} = \frac{1}{\bar{\gamma}}\frac{\partial\,\hat{s}^{(2)}}{\partial\,\bar{\gamma}}\Big(\gamma^{(1)}\nu^{(1)} + \alpha\gamma^{(2)}\nu^{(2)}\Big), \tag{2.27}$$

so that

$$h^{(11)} = \frac{\gamma^{(1)}}{\bar{\gamma}}\frac{\partial\,\hat{s}^{(1)}}{\partial\,\bar{\gamma}}, \quad h^{(12)} = \frac{\alpha\gamma^{(2)}}{\bar{\gamma}}\frac{\partial\,\hat{s}^{(1)}}{\partial\,\bar{\gamma}}, \quad h^{(21)} = \frac{\gamma^{(1)}}{\bar{\gamma}}\frac{\partial\,\hat{s}^{(2)}}{\partial\,\bar{\gamma}}, \quad h^{(22)} = \frac{\alpha\gamma^{(2)}}{\bar{\gamma}}\frac{\partial\,\hat{s}^{(2)}}{\partial\,\bar{\gamma}}. \tag{2.28}$$

A simple explicit constitutive time-integration procedure for the rate-independent interface model is summarized in the Appendix. The model, using this time-integration procedure has been implemented in the finite element program ABAQUS/Explicit

(ABAQUS, 2002) by writing a USER INTERFACE subroutine.

2.3 Constitutive model for single-crystals

We shall employ the (now classical) single-crystal plasticity theory (e.g., Taylor 1938; Mandel 1965, 1972; Hill 1965; Teodosiu 1970; Teodosiu and Sidoroff 1976; Rice 1971; Asaro 1983; Asaro and Needleman 1985; Bronkhorst et al. 1992). A rate-independent version of the single-crystal plasticity model is summarized below.

Single-crystal plasticity is based on the hypothesis that plastic flow takes place through slip on prescribed slip systems $\alpha = 1, 2, \ldots, N$, with each system α defined by a *slip direction* $\mathbf{s}^\alpha$ and a *slip-plane normal* $\mathbf{m}^\alpha$, where

$$\mathbf{s}^\alpha \cdot \mathbf{m}^\alpha = 0, \qquad |\mathbf{s}^\alpha|, |\mathbf{m}^\alpha| = 1, \qquad \mathbf{s}^\alpha, \mathbf{m}^\alpha = \text{constant}. \tag{2.29}$$

For a material with *slip systems* $\alpha = 1, 2, \ldots, N$ defined by orthonormal vector pairs $(\mathbf{m}_0^\alpha, \mathbf{s}_0^\alpha)$, the constitutive equations relate the following basic fields:

ψ,		free energy density per unit referential volume,
$\mathbf{F}$,	$J = \det \mathbf{F} > 0$,	deformation gradient,
$\mathbf{T}$,		Cauchy stress,
$\mathbf{F}^p$,	$\det \mathbf{F}^p = 1$,	plastic part of the deformation gradient,
$\boldsymbol{\sigma} = \{s^1, s^2, \cdots, s^N\}$,	$s^\alpha > 0$,	slip resistances,
$\mathbf{F}^e = \mathbf{F}\mathbf{F}^{p-1}$,	$\det\mathbf{F}^e > 0$,	elastic part of the deformation gradient,
$\mathbf{C}^e = \mathbf{F}^{eT}\mathbf{F}^e$,		elastic right Cauchy-Green strain,
$\mathbf{E}^e = \frac{1}{2}(\mathbf{C}^e - \mathbf{1})$,		elastic strain,
$\mathbf{T}^e = (\det\mathbf{F}^e)\mathbf{F}^{e-1}\mathbf{T}\mathbf{F}^{e-\top}$,		stress conjugate to $\mathbf{E}^e$.

The constitutive theory, intended to characterize small elastic strains, is summarized below.

The *free energy* is given by

$$\psi(\mathbf{E}^e) = \frac{1}{2}\,\mathbf{E}^e \cdot \boldsymbol{\mathcal{C}}[\mathbf{E}^e], \tag{2.30}$$

where $\boldsymbol{\mathcal{C}}$ is the elasticity tensor. The *elastic stress-strain relation* has the form

$$\mathbf{T}^e = \boldsymbol{\mathcal{C}}[\mathbf{E}^e], \tag{2.31}$$

while the *resolved stress* on the αth slip system is given by

$$\tau^\alpha = \mathbf{s}_0^\alpha \cdot (\mathbf{C}^e\mathbf{T}^e)\mathbf{m}_0^\alpha. \tag{2.32}$$

The condition for slip on the αth slip system is taken as

$$\phi^\alpha = |\tau^\alpha| - s^\alpha \le 0, \tag{2.33}$$

where s^α is the slip system deformation resistance.

The *flow rule* is defined by an evolution equation for $\mathbf{F}^p$ of the form

$$\dot{\mathbf{F}}^p = \mathbf{L}^p\mathbf{F}^p, \qquad \mathbf{L}^p = \sum_{\alpha=1}^{N} \nu^\alpha\, \mathbf{s}_0^\alpha \otimes \mathbf{m}_0^\alpha, \quad \nu^\alpha \ge 0, \quad \text{and} \quad \nu^\alpha\,\phi^\alpha = 0, \quad \mathbf{F}^p(0) = \mathbf{1}, \tag{2.34}$$

The *evolution equations* for the internal variables s^α are

$$\dot{s}^\alpha = \sum_{\beta=1}^{N} h^{\alpha\beta}(\boldsymbol{\sigma}|\nu^\beta|, \qquad s^\alpha(0) = s_0^\alpha. \tag{2.35}$$

During plastic flow the following *consistency conditions* must be satisfied:

$$\nu^\alpha\,\dot{\phi}^\alpha = 0 \quad \text{if} \quad \phi^\alpha = 0. \tag{2.36}$$

The consistency conditions serve to determine the shearing rates $\nu^\alpha \ge 0$ on the slip systems.

To complete the constitutive model for a given ductile single crystal, the material parameters/functions that need to be specified are the slip-systems $(\mathbf{m}_0^\alpha, \mathbf{s}_0^\alpha)$ and their *initial orientations*, as well as

$$\left\{\boldsymbol{\mathcal{C}}, s_0^\alpha, h^{\alpha\beta}\right\}.$$

A constitutive time-integration procedure for the rate-independent crystal plasticity model has been previously detailed in Anand and Kothari (1996), and for brevity is not repeated here. The single-crystal plasticity model using this time-integration procedure has been implemented in the finite element program ABAQUS/Explicit (ABAQUS, 2002) by writing a USER MATERIAL subroutine.

2.4 Application to nc nickel

Experimentally-measured stress-strain curves in simple tension from specimens of electrodeposited nc nickel with grain sizes ranging from 15nm to 40nm from different groups show a highly nonlinear stress-strain response up to an ultimate tensile strength between $\approx$ 1.3 to 1.7 GPa, and final fracture at strain levels ranging from $\approx$ 2.5% to 5% (e.g., Wang et al. 1997; Yin and Whang 2001; Xiao et al. 2001; Torre et al. 2002). We shall use this representative experimental information to *estimate* the material parameters for the grain interiors as well as the grain boundaries by judiciously adjusting the values of the material parameters in our constitutive model to approximately match these stress-strain curves. We recognize that such a procedure for material parameter estimation is *not unique*. However, the values for the material parameters, so estimated, serve reasonably well the primary objective of this work, which is to *qualitatively study* the competition between the grain interior and grain boundary deformation modes in nc f.c.c. materials.

For reasons of computational efficiency, in our simulations we have used a *quasi-three-dimensional* polycrystalline aggregate consisting of a collection of columnar grains. Actually, the electrodeposited nc nickel does possess an approximately columnar grain structure (see Fig. 1c of Kumar et al. 2003). However, the grain structure with only one grain through the thickness used in the calculations does not quite

approach the actual columnar grain structure. The numerical grain structure is more suitable for modelling *fine-grained polycrystalline thin films* which show a similar macroscopic stress-strain response. An aggregate consisting of 50 such grains is shown in Fig. 2-6 a. This initial microstructure was generated by first using a (more or less) standard Voronoi construction in two-dimensions, and then extruding it to obtain the third direction. Instead of using a totally random set of seeds to generate the voronoi tesselation, which occasionally results in extremely small grains, we numerically imposed a minimum distance between the possible "random seeds." This helps to increase the quality of the microstructural geometry for finite element computations. After determining the vertices of each grain and its neighbors, the geometry is imported into in ABAQUS/CAE (ABAQUS, 2002) for generating the finite element mesh, Fig. 2-6 b, and specifying the single crystal constitutive model described in § 3 for the grain interiors, as well as the interaction between neighboring grains using the interface model described in §2. Nc nickel produced by electrodeposition typically possesses a strong crystallographic texture. Fig. 2-6 c shows the (111) pole figure for such a material (Xiao et al., 2001); the pole figure projection direction is normal to the plane of the sheet specimen. In our numerical simulations the lattices of the individual grains were assigned a set of orientations that approximate this initial texture, Fig. 2-6 d. For the grain interiors, the anisotropic elasticity tensor $\boldsymbol{\mathcal{C}}$ is specified in terms of three stiffness parameters, C_{11}, C_{12} and C_{44}. The values of the elastic parameters for nickel are taken as Simmons and Wang (1971):

$$C_{11} = 247\,\text{GPa}, C_{12} = 147\,\text{GPa}, C_{44} = 125\,\text{GPa}.$$

For f.c.c. crystals, crystallographic slip is assumed to occur on the twelve $\{111\} < 110 >$ slip systems. The components of the slip-plane normals $\mathbf{m}_0^\alpha$ and slip directions $\mathbf{s}_0^\alpha$ with respect to an orthonormal basis associated with the crystal lattice are listed in Table 2.1.

The interface stiffnesses, K_N and K_T in the normal and tangential directions, are estimated as $K_N \approx E/g$ and $K_T \approx G/g$ where E and G are, respectively, nominal

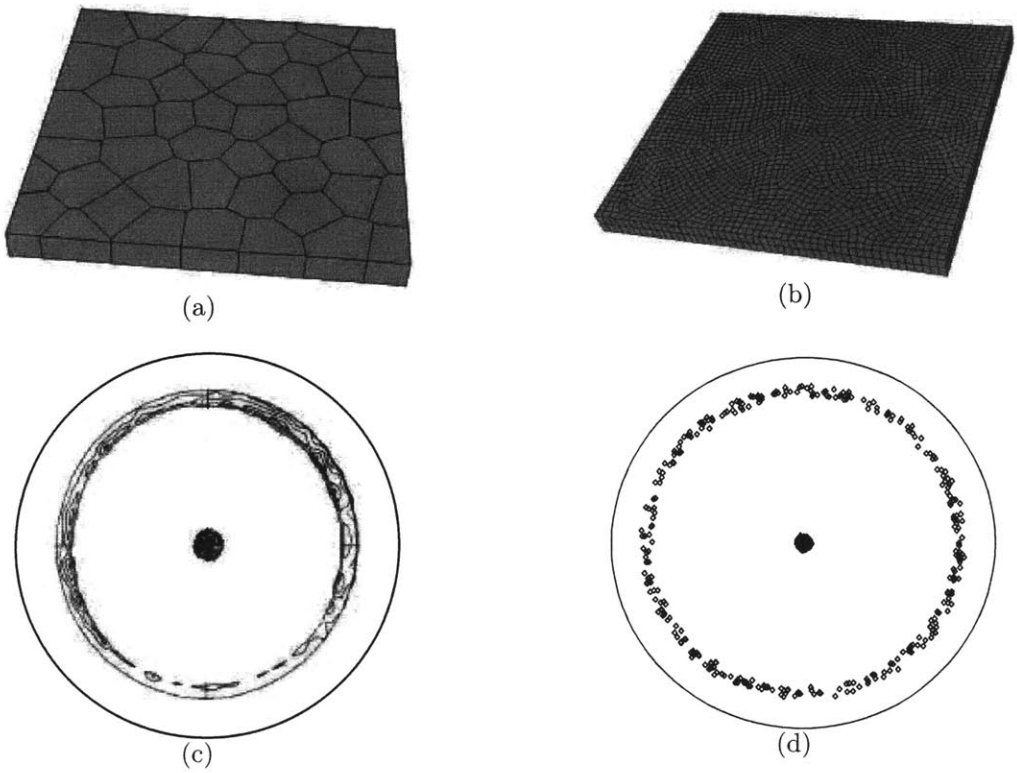

Figure 2-6: (a) Initial microstructure represented by 50 columnar grains. (b) Finite-element mesh. (c) Experimental (111) pole figure of as-received electrodeposited nc-nickel from Xiao et al. (2001); pole figure projection direction is normal to the plane of the sheet specimen. (d) (111) pole figures corresponding to the grain orientations used in the polycrystal simulation.

values of isotropic polycrystalline Young's modulus and shear modulus, and g is an estimate of a "grain-boundary thickness." *Our continuum model has no inherent length scale. However, in this application we use a scale in which the average grains in our finite element mesh are taken to be* $\approx 30\,nm$*, and assume that the grain-boundary thickness is* $g \approx 1\,nm$. For nickel, using representative values of E and G and $g = 1\,\text{nm}$ gives an estimate of

$$K_N = 200\,\text{GPa/nm}, \qquad K_T = 76\,\text{GPa/nm}. \tag{2.37}$$

In the simulations to follow, we take the resistance of an interface in tangential direction to be independent of the normal stress on that interface, i.e., $\mu = 0$, so that associated flow is recovered.

α	$\mathbf{m}_o^\alpha$			$\mathbf{s}_o^\alpha$		
1	$\frac{1}{\sqrt{3}}$	$\frac{1}{\sqrt{3}}$	$\frac{1}{\sqrt{3}}$	$\frac{1}{\sqrt{2}}$	$-\frac{1}{\sqrt{2}}$	0
2	$\frac{1}{\sqrt{3}}$	$\frac{1}{\sqrt{3}}$	$\frac{1}{\sqrt{3}}$	$-\frac{1}{\sqrt{2}}$	0	$\frac{1}{\sqrt{2}}$
3	$\frac{1}{\sqrt{3}}$	$\frac{1}{\sqrt{3}}$	$\frac{1}{\sqrt{3}}$	0	$\frac{1}{\sqrt{2}}$	$-\frac{1}{\sqrt{2}}$
4	$-\frac{1}{\sqrt{3}}$	$\frac{1}{\sqrt{3}}$	$\frac{1}{\sqrt{3}}$	$\frac{1}{\sqrt{2}}$	0	$\frac{1}{\sqrt{2}}$
5	$-\frac{1}{\sqrt{3}}$	$\frac{1}{\sqrt{3}}$	$\frac{1}{\sqrt{3}}$	$-\frac{1}{\sqrt{2}}$	$-\frac{1}{\sqrt{2}}$	0
6	$-\frac{1}{\sqrt{3}}$	$\frac{1}{\sqrt{3}}$	$\frac{1}{\sqrt{3}}$	0	$\frac{1}{\sqrt{2}}$	$-\frac{1}{\sqrt{2}}$
7	$\frac{1}{\sqrt{3}}$	$-\frac{1}{\sqrt{3}}$	$\frac{1}{\sqrt{3}}$	$-\frac{1}{\sqrt{2}}$	0	$\frac{1}{\sqrt{2}}$
8	$\frac{1}{\sqrt{3}}$	$-\frac{1}{\sqrt{3}}$	$\frac{1}{\sqrt{3}}$	0	$-\frac{1}{\sqrt{2}}$	$-\frac{1}{\sqrt{2}}$
9	$\frac{1}{\sqrt{3}}$	$-\frac{1}{\sqrt{3}}$	$\frac{1}{\sqrt{3}}$	$\frac{1}{\sqrt{2}}$	$\frac{1}{\sqrt{2}}$	0
10	$-\frac{1}{\sqrt{3}}$	$-\frac{1}{\sqrt{3}}$	$\frac{1}{\sqrt{3}}$	$-\frac{1}{\sqrt{2}}$	$\frac{1}{\sqrt{2}}$	0
11	$-\frac{1}{\sqrt{3}}$	$-\frac{1}{\sqrt{3}}$	$\frac{1}{\sqrt{3}}$	$\frac{1}{\sqrt{2}}$	0	$\frac{1}{\sqrt{2}}$
12	$-\frac{1}{\sqrt{3}}$	$-\frac{1}{\sqrt{3}}$	$\frac{1}{\sqrt{3}}$	0	$-\frac{1}{\sqrt{2}}$	$-\frac{1}{\sqrt{2}}$

Table 2.1: Components of slip plane normals $\mathbf{m}_0^\alpha$ and slip directions $\mathbf{s}_0^\alpha$ in the crystal basis for the twelve slip systems of an f.c.c. crystal.

Referring back to equations for slip resistances, we assume that the *hardening portion* of the traction-separation curves can be fit to the following special form of the evolution for the two resistances $s^{(i)}$:

$$\dot{s}^{(i)}_{hard} = h_0^{(i)} \left\{ 1 - \frac{s^{(i)}}{s^{*(i)}} \right\}^{a^{(i)}} \dot{\bar{\gamma}}, \qquad \text{with initial values} \quad s^{(i)}(0) = s_0^{(i)}, \quad \text{for} \quad \bar{\gamma} \leq \bar{\gamma}_c, \tag{2.38}$$

with $s^{*(i)} \geq s^{(i)}$. Recall that we have defined the equivalent relative plastic displacement by

$$\bar{\gamma} = \sqrt{(\gamma^{(1)})^2 + \alpha\,(\gamma^{(2)})^2};$$

we assume a value for the coupling parameter $\alpha = 0.25$, *and (guided by our assumption of a grain-boundary thickness* $g = 1$ *nm) a value of* $\bar{\gamma}_c = 1$ *nm when the interface starts to soften in any combination of tension or shear.* Thus, in pure tension $\bar{\gamma}_c = \gamma_c^{(1)} =$ 1nm, while in pure shear $\gamma_c^{(2)} = 2\,\text{nm}$. In our numerical simulations we allow for a softening branch to the interface traction-separation response, by *assuming* a simple linear softening from $\bar{\gamma}_c$ to a failure value $\bar{\gamma}_{fail}$:

$$\dot{s}^{(i)}_{soft} = -h^{(i)}_{soft}\dot{\bar{\gamma}} \quad \text{for} \quad \bar{\gamma}_c < \bar{\gamma} \leq \bar{\gamma}_{fail}. \tag{2.39}$$

	$s_0^{(i)}$ (MPa)	$h_0^{(i)}$ (GPa/nm)	$s^{*(i)}$ (MPa)	$a^{(i)}$	$\bar{\gamma}_c$ (nm)	$\bar{\gamma}_{fail}$ (nm)	$h_{soft}^{(i)}$ GPa/nm
$i = 1$, Tension	300.0	28.3	2400.0	5.0	1	1.1	15
$i = 2$, Shear	150.0	20.0	1200.0	5.0	1	1.1	15

Table 2.2: Parameters used for the inelastic response of an interface in nc nickel.

Next, considering that there is little or no dislocation activity in the grain interiors of nc materials, the slip resistances for the grain interiors s^α are assumed to be all equal to a *constant* s_0:

$$s^\alpha = s_0 \quad \cdots \quad \text{constant slip system resistance for grain interiors.} \tag{2.40}$$

For nc-Ni, the magnitude of s_0 for the grain interiors is estimated, together with the material parameters for the interface model, by fitting a stress-strain curve in tension.

Using our previously-listed assumptions, a value

$$s^\alpha = 800\,\text{MPa} \quad \cdots \quad \text{slip system resistance for grain interiors,} \tag{2.41}$$

and for the inelastic properties of the interface, we obtained the curve-fit shown in Fig. 2-7. The traction-separation curves corresponding to the values of K_N and K_T given in (2.37) and the the inelastic parameters for the interface given in Table 2 are shown in Fig. 2-7.

Fig. 2-8 shows contours of a measure of an *equivalent plastic strain in the grains*, defined by

$$\bar{\epsilon}^p = \int \dot{\bar{\epsilon}}^p dt, \quad \text{where } \dot{\bar{\epsilon}}^p = \frac{\sum_\alpha \tau^\alpha \nu^\alpha}{\bar{\sigma}} \quad \text{with} \quad \bar{\sigma} = \sqrt{(3/2)\mathbf{T}_0^e \cdot \mathbf{T}_0^e}, \quad \mathbf{T}_0^e \stackrel{def}{=} \mathbf{T}^e - \frac{1}{3}\text{tr}(\mathbf{T}^e)\,\mathbf{1}$$

corresponding to four different points, labelled a through d, on the stress-strain response, Fig. 2-8 a. For clarity, the maximum value of the $\bar{\epsilon}^p$ contours is set to 5% for all four contour plots. *Since Fig. 2-8 b shows essentially no plastic strain in the grain interiors, the nonlinearity in the macroscopic stress-strain curve up to point a is*

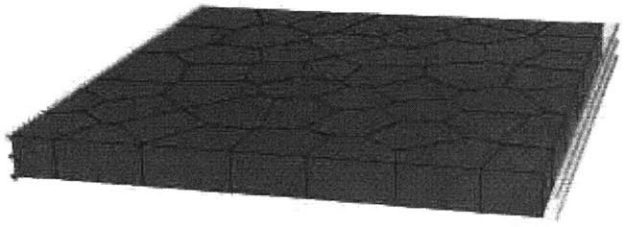

(a)

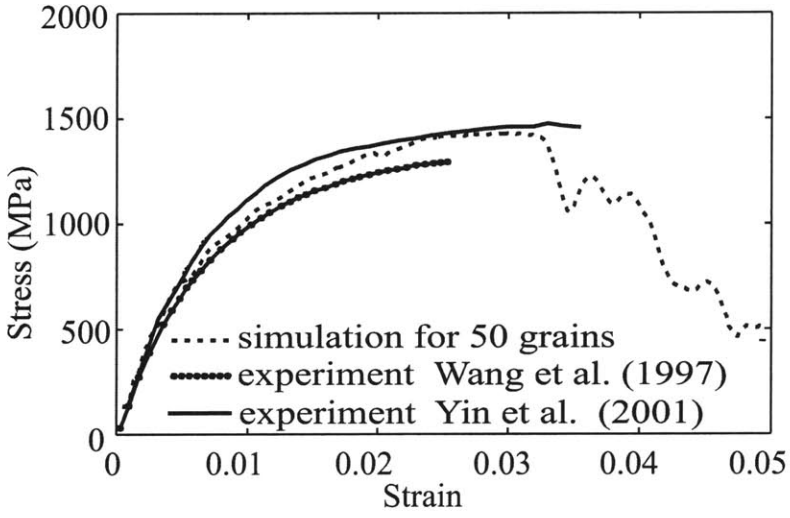

(b)

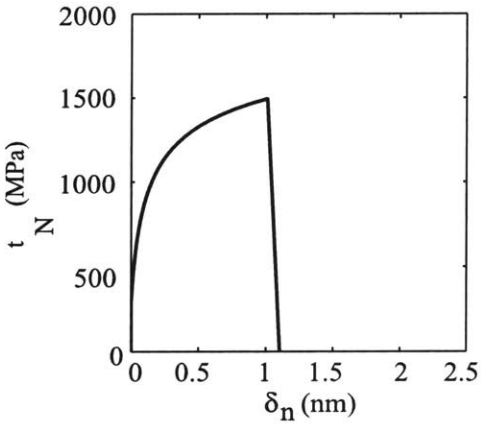

(c)

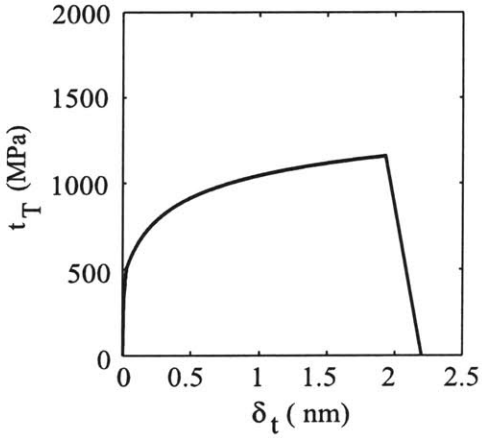

(d)

Figure 2-7: (a) Boundary conditions used in the numerical simulation, and comparison of stress-strain curve in tension from the numerical simulation against corresponding experimental data from the literature, Wang *et al.* (1997) and Yin *et al.* (2001). Traction-separation curves used for nano-crystalline nickel: (b) in the normal direction to an interface, and (c) in the tangential direction to an interface.

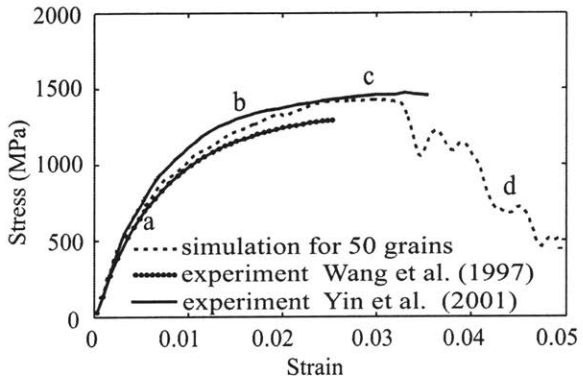

(a)

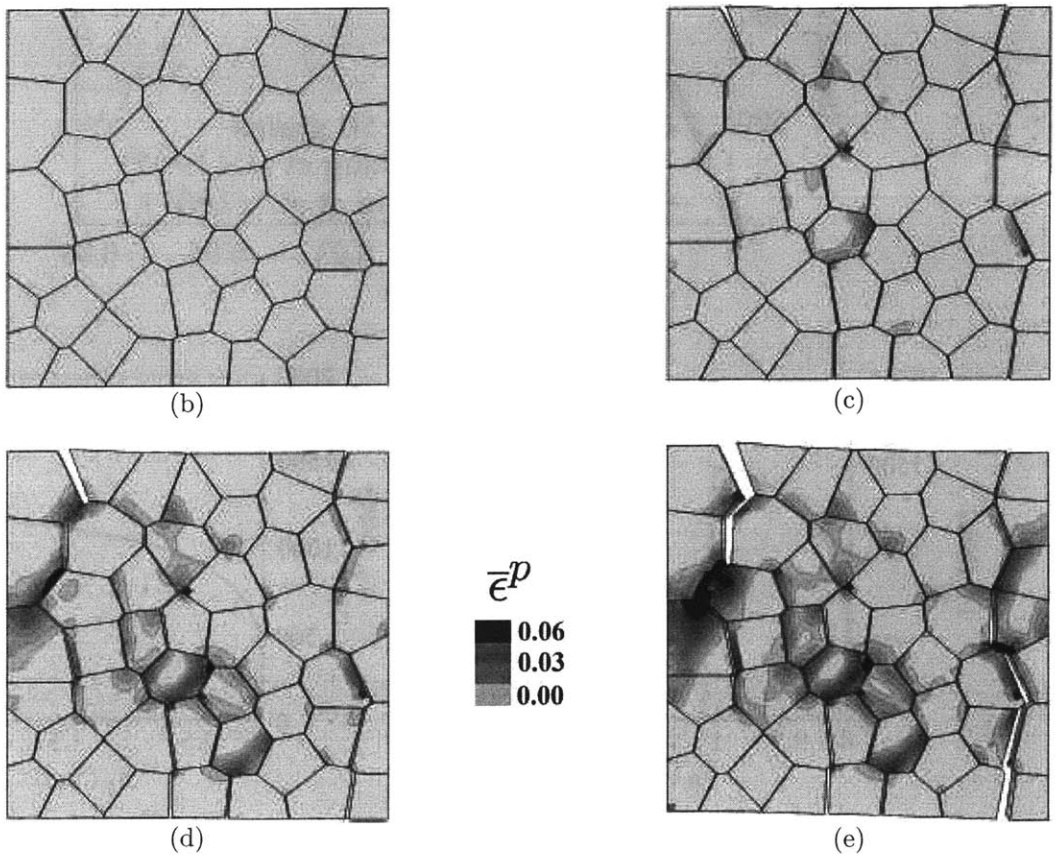

(b) (c) (d) (e)

Figure 2-8: (a) Stress-strain curve from the simulation and literatures. Contour plots (b) through (e) of the equivalent plastic strain *in the grain interiors* corresponding to different macroscopic strain level keyed to stress-strain curve.

due entirely to the nonlinear elastic-plastic interface response. By point b (Fig. 2-8 c) on the stress-strain curve, there is some plastic strain in the vicinity of a few grain-boundary triple junctions; however, the major cause for the macroscopic nonlinear stress-strain response is still the nonlinear interface response; indeed, by this stage a few of the interfaces have visibly failed. By point c (Fig. 2-8 d), near the peak of the stress-strain curve, there is a dominant macroscopic crack traversing along several grain boundaries (top left of Fig. 2-8 d), and substantial plastic strain within the interiors of the grains at the tip of the crack. By point d (Fig. 2-8 e) on the stress-strain curve at least three dominant interface cracks are clearly visible, and the material has lost a large fraction of its stress-carrying capacity. The propagation of grain-boundary cracks causes a substantial amount of plastic deformation in the interior of the grains blocking the crack-path, and in the boundary regions of the grains adjacent to the crack path.

In order to further understand the origin of the nonlinear stress-strain response of the nc nickel during tension, we numerically suppressed any plastic deformation in the grain interiors, so that the grain interiors deform elastically and the only source of inelastic deformation is due to grain-boundary sliding and separation. Fig. 2-9 compares the simulated stress-strain responses when the grain interiors deform elastically, against the response where the grain interiors are allowed to deform plastically with slip resistances set at $s^{\alpha} = 800\,\mathrm{MPa}$. From this figure it is clear that up to point b, the macroscopic stress-strain is dominated by the nonlinear grain-boundary response. From b to c, the local stress levels are high enough to cause plastic deformation in some of the grain interiors and soften the overall stress-strain response.

2.5 Grain-size effect

The effects of a variation of the grain-size on the macroscopic stress-strain curve, as predicted by the continuum model, are shown in Fig. 2-10. In these simulations, the role of grain-size on the macroscopic response of nc nickel was modelled in the following fashion: the material parameters for the grain-boundary response were *fixed*

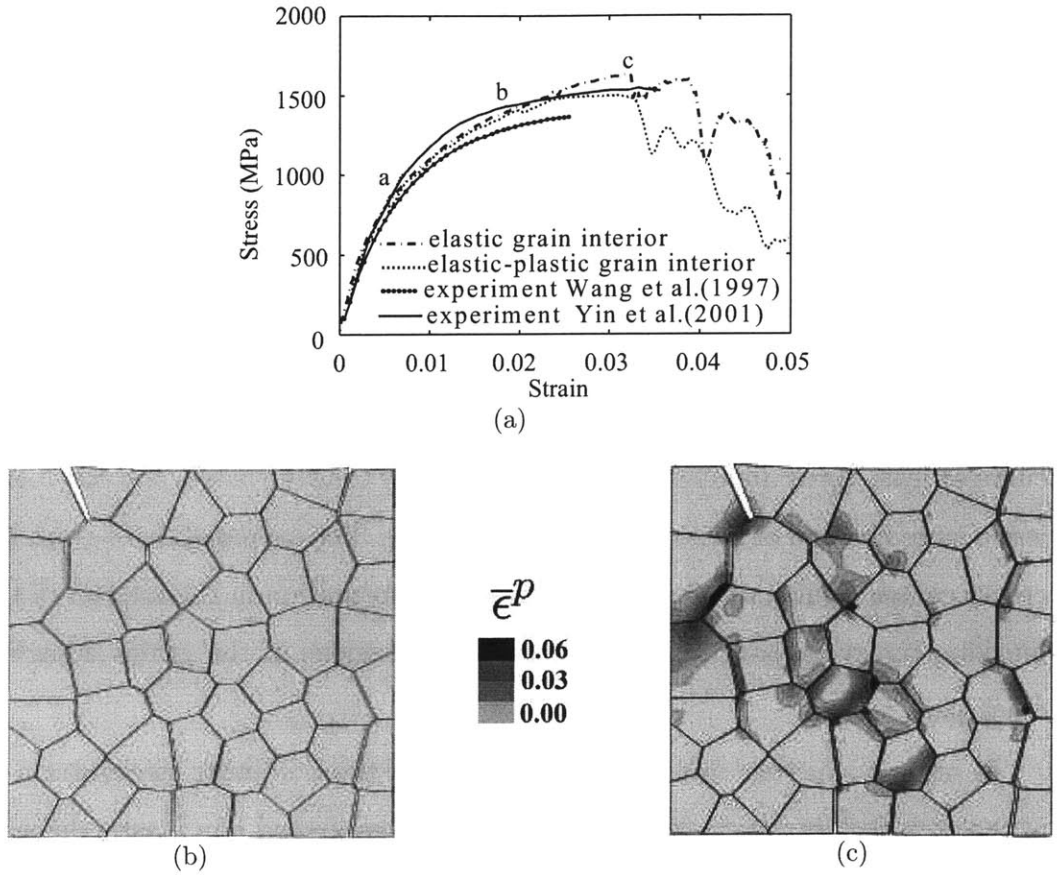

Figure 2-9: (a) Comparison of stress-strain curves in tension from a numerical simulation which uses a model in which the grain interiors that deform only elastically, against results from another simulation in which the grain interiors may also deform plastically. Corresponding contours of equivalent plastic strain plotted on the deformed geometry at strain levels approximately corresponding to point c on the stress-strain curves are shown in (b) for elastically-deforming grain interiors, and (c) for grain interiors which may also deform plastically.

once they were calibrated by using the 50-grain mesh and the experimental data, Fig. 2-7. Then, the number of grains in the same macroscopic volume as that of the mesh with 50 grains, was changed. 5 new meshes with 12, 28 , 39, 110 and 236[3] grains were considered. With the averaged grain-size of the 50-grain mesh is scaled to be around 30 nm, we can get the averaged grain size for the other five meshes (Table 3). The slip resistances for individual grains are assigned based on the relationship that $s \approx \frac{Gb}{d}$ with G the shear modulus, b the magnitude of a burgers vector and d the grain diameter. Recall that the ideal shear stress for fcc metal is approximated by $G/30$,

[3]The grain size in this mesh satisfies a log normal distribution Gross and Li 2002.

averaged grain size (nm)	averaged slip resistance (MPa)
61	396
40	599
34	710
30	800
20	1180
14	1730

Table 2.3: Averaged grain size and slip resistance for different meshes.

we use this upper bound (approximate $2.7GPa$ for nickel) as their slip resistance for those small grains whenever their calculated resistances are higher than the ideal one. Table 3 listed the averaged grain size and slip resistance for the 6 meshes we used.

The macroscopic stress-strain curves for meshes with different grains were shown in Fig. 2-10a. The unlitimate strength for each simulation versus the grain size was shown in the loglog plot Fig. 2-10b, which shows both a Hall-Petch at ultra fine grain size region and inverse Hall-Petch effect at very small grain size region . For the Hall-Petch effect, the slope is around -0.5. However, for the inverse Hall-Petch, we can see that the softening here is much slower than the hardening presented at the other side. The inverse Hall-Petch relation from this simulation has a slope around 0.1. With a decrease in the grain-size, and hence an increase in the grain-boundary fraction per unit volume, we also find from the macroscopic stress-strain curves that the ductility showed a transition with variance of grain size.

Plots in Fig. 2-10 (c) through Fig. 2-10 (h) show contours of the equivalent plastic strain *in the grain interiors* corresponding to the strain levels right after peak stress for each grain-size. Since the grain-boundary have been taken to be identical in all calculations, and the grain-interior strengths increase with decreasing grain size. At large grain sizes, as we see from the mesh with 12 grains, the plastic deformation in the grain interior dominates. As the further reduction of grain size, the observed macroscopic ductility will decrease. Because the increment of ductility from grain boundary slipping/opening couldn't compensate the loss when higher slip resistance constraints plastic slips in grain interiors, the net ductility decreases with decreasing

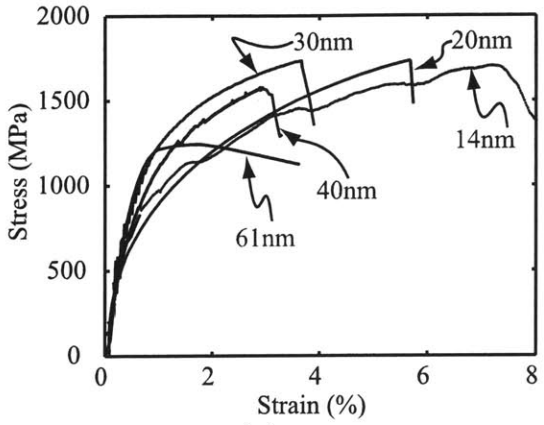

(a)

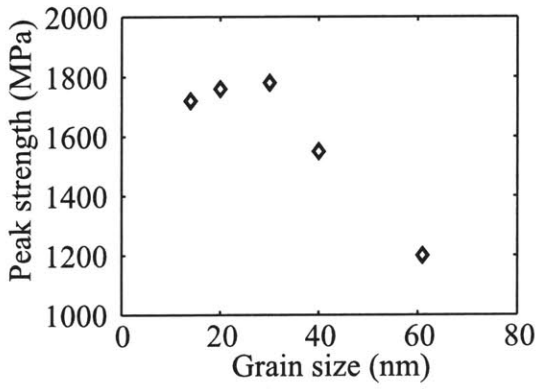

(b)

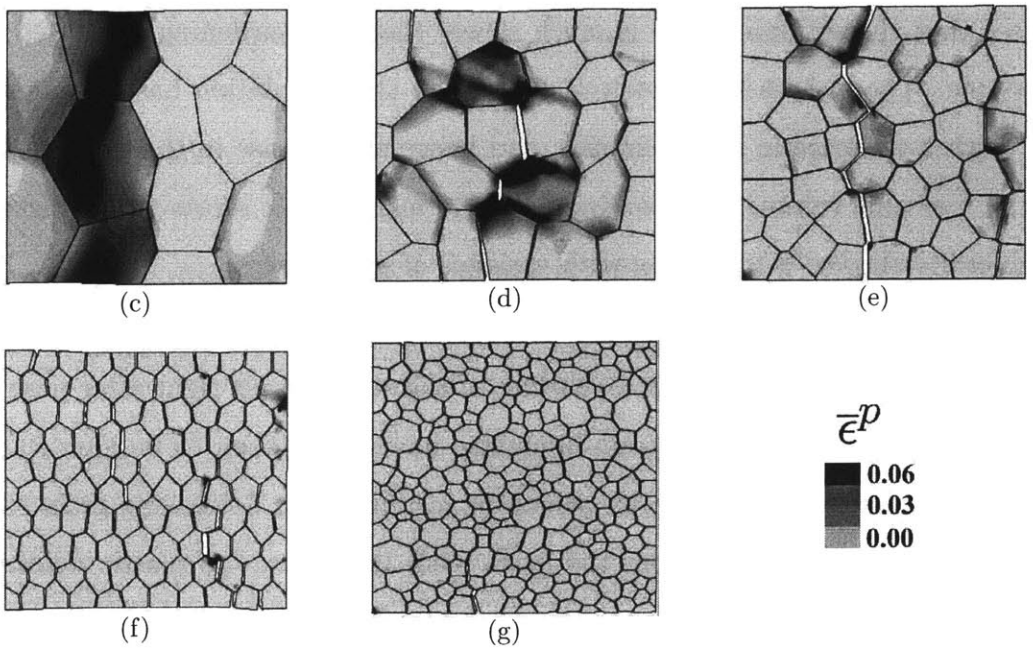

Figure 2-10: (a) Stress-strain curves for different grain sizes. (b) Peak strength versus grain size. Plots (c) through (g) show contours of the equivalent plastic strain *in the grain interiors* corresponding to the strain levels right after peak stress for the 61nm, 40nm, 30nm, 20nm and 14nm average grain-sized microstructures.

grain size. Nevertheless, once the grain size reduced to some extent, further decreasing of grain size results in an increased ductility shown in Fig. 2-10 (a) for meshes with 110 and 236 grains. The increasing of ductility at this stage is due entirely to the *more distributed nature of grain boundary deformation/damage with decreasing grain-size.* This is an example of the *inverse Hall-Petch effect* at very small grain-sizes, where the strength level of the grain-interiors is presumably fixed at a level comparable to the ideal shear strength of the material, while the softer overall response is due entirely to an increased amount of distributed grain-boundary sliding and separation as the grain-boundary area increases with a decreasing grain-size.

2.6 Fracture in a notched specimen

Finally, to numerically simulate the situation corresponding to a tension test on a perforated nano-nickel specimen, cf. Fig. 3, The mesh with 236 grain shown in Fig. 2-10 (h) was adopted and rescaled with a mean grain-size of 30 nm. The overall dimensions are $1000\,\mu\text{m} \times 1000\,\mu\text{m} \times 80\,\mu\text{m}$. An initial notch was generated by simply removing a few grains at right boundary (Fig. 2-11). Properties of the grain boundary and grain interior are taken as the same as we used for the calibration test for the 50 grain mesh (Fig. 2-8). The resulting macroscopic load-displacement curve is shown in Fig. 2-11(a). Contour plots of the equivalent plastic strain in the grain interiors corresponding to different macroscopic displacement levels keyed to load-displacement curve are shown in Fig. 2-11(b) through (e). These figures also show the nucleation and propagation of the intergranular crack(s) which give rise to the macroscopic failure.

A crack, labelled crack A, nucleates initially at the tip of the notch because of the high local stress concentration. Plastic deformation in the grain interiors at this stage is small, and mainly occurs in the vicinity of the newly-nucleated crack tip, Fig. 2-11(b). From the load-displacement we see that there is an approximate load-plateau from a to b. Microstructurally, at stage b the propagation of crack A is blocked by an unfavorably oriented grain G1, Fig. 2-11(c), and this results in a significant

plastic deformation within the interior of this grain. Upon further increase of the macroscopically-applied displacement, the local conditions between grains G2 and G3 cause the nucleation of a new crack, labelled crack B, Fig. 2-11(d). Upon further application of the macroscopic deformation, cracks A and B further extend toward each other, and the macroscopic load drops. The region in Fig. 2-11(e) surrounded by a dotted line shows that by this stage the remaining ligament between the two cracks exhibits both interface cracking, as well as substantial plastic deformation within the grain interiors — much in accord with experimental observations of Kumar et al. (2003).

2.7 Concluding remarks

To model the effects of grain boundaries in polycrystalline materials we have coupled a standard crystal-plasticity model for the grain interiors with a new elastic-plastic grain-boundary interface model which accounts for both reversible elastic, as well irreversible inelastic sliding-separation deformations at the grain boundaries prior to failure. We have used this new computational capability to study the deformation and fracture response of nc nickel in simple tension. The results from the simulations capture the experimentally-observed stress-strain curves (Wang et al. 1997; Yin and Whang 2001; Xiao et al. 2001; Torre et al. 2002), and the dominant fracture mechanisms in this material (Kumar et al., 2003). The macroscopically-observed nonlinearity in the stress-strain response is mainly due to the inelastic response of the grain-boundaries. Plastic deformation in the interior of the grains prior to the formation of grain-boundary cracks was rarely observed. The stress concentrations at the tips of the distributed grain-boundary cracks, and at grain-boundary triple junctions, cause a limited amount of plastic deformation in the high-strength grain interiors. The competition of grain-boundary deformation with that in the grain-interiors determines the observed macroscopic stress-strain response, and the overall ductility. In nc nickel, the high yield strength of the grain interiors and relatively weaker grain-boundary interfaces account for the low ductility of this material in

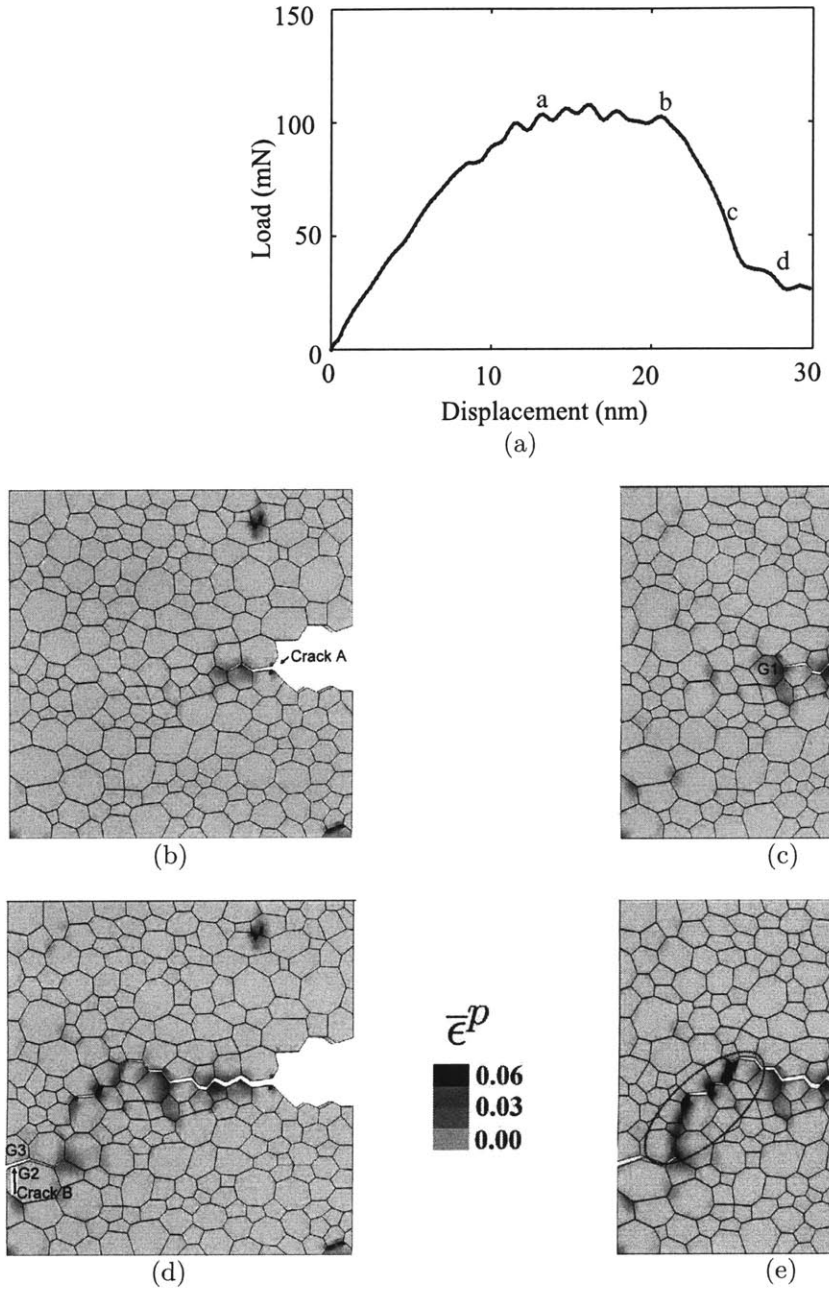

Figure 2-11: Fracture in a notched-tensile specimen. (a): Load versus displacement. Contour plots in (b) through (e) show the equivalent plastic strain *in the grain interiors* corresponding to different macroscopic displacement levels keyed to load-displacement curve.

tension.

Chapter 3

Modeling of the mechanical behavior of fcc nanocrystalline metals with disordered, rate-sensitive GBs

3.1 Introduction

Nanocrystalline metals are polycrystalline metallic materials with grain sizes typically less than 100 nm. These materials have been the subject of intense, world-wide research over the past two decades, and due to this research activity the micromechanisms governing their macroscopic mechanical behavior are now beginning to be better understood. Recent reviews on the topic, and references to the vast amount of literature, may be found in Kumar et al. (2003); Wolf et al. (2005); Meyers et al. (2006). Nanocrystalline metals contain a high volume fraction of "grain boundary"-intercrystalline regions. For example, idealizing a unit cell containing a crystalline grain interior and an intercrystalline grain boundary region as a sphere of diameter d, with an intercrystalline shell of thickness δ and a crystalline core of diameter $d - 2\delta$,

[1]The work in this chapter is submitted to Acta Materialia (2006) for publication.

the volume fractions of grain boundary regions for a fixed value of $\delta \sim 0.5\,\text{nm}$, and grain sizes d of 10 nm and 40 nm are 27.1 % and 7.3 %, respectively. Thus, a substantial fraction of the atoms in nanocrystalline materials lie in the intercrystalline grain-boundary regions, and these regions play an increasingly significant role as the grain size decreases below the 100 nm level. The nature of the intercrystalline grain boundary regions depends on how the material has been processed. High-resolution transmission electron microscopy (TEM) studies on nanocrystalline materials show that while many grain boundaries appear sharp and well-defined, others show considerable disorder, with the maximum disordered region (measured perpendicular to grain boundaries) being approximately 2 to 3 lattice spacings, i.e., less than 1 nm (Ranganathan et al., 2001).

In this chapter we focus our attention on continuum-level modeling of the low temperature mechanical response of nanocrystalline fcc metals. A broad picture of the operative micromechanisms of inelastic deformation in this class of materials in this temperature range is beginning to emerge. The following features of the operative micromechanisms are now reasonably widely-accepted (Kumar et al., 2003; Wolf et al., 2005; Meyers et al., 2006; Farkas et al., 2002; Sansoz and Molinari, 2004; Farkas et al., 2005):

- There is a strong interplay between dislocation-based deformation in the crystalline grain interiors and the inelastic deformation mechanisms operative in the grain-boundary regions.

- Grain boundaries act as both sources and sinks for dislocations.

- Let Γ denote the stacking fault energy of the fcc material, G its nominal shear modus, and b the magnitude of the Burgers vector of a perfect dislocation, then there exists a critical grain size d_c given by

$$d_c \approx \frac{2}{3}\Big(\frac{Gb^2}{\Gamma}\Big), \tag{3.1}$$

  above which plastic deformation in nanocrystalline grain interiors occurs by

the emission of *complete dislocations* from grain boundaries, and below which the plastic deformation occurs by *partial dislocations.* The partial dislocations produce stacking faults as they glide through the grains, Asaro et al. (2003); Zhu et al. (2005).

- The number of dislocations or stacking faults that need to traverse a typical grain in the nanocrystalline range to produce an overall strain of the order of 5% is quite small, typically less than 10 – 15. Thus, dislocation-based plasticity in the grain interiors is quite *discrete* in nature.

- When the grain size d becomes smaller than d_c, dislocation-based slip processes become less effective in producing overall inelastic deformation, and grain-boundary region-based inelastic deformation mechanisms start to dominate (Van Vliet et al., 2003; Yip, 2004; Yamakov et al., 2004).

- The grain-boundary inelastic deformation mechanisms are loosely called "grain boundary sliding," but at low temperatures atomistic simulations show this to be stress-activated *shear-shuffling* of atoms located in the intercrystalline regions, and the cooperative result of numerous such shear-shuffles leads to substantial overall shearing of the intercrystalline regions; this process is *not* dominated by thermal diffusion of atoms in the grain boundary regions. As noted by Lund et al. (2004b), such a deformation mechanism is reminiscent of that in metallic glasses, where inelastic deformation occurs by local shearing of clusters of atoms — "shear transformation zones"; this shearing is accompanied by inelastic dilatation that produces strain-softening, which then leads to the formation of intense shear bands (Deng et al., 1989).

- Nanocrystalline fcc materials show a room-temperature strain-rate sensitivity which is almost an order of magnitude higher than their microcrystalline counterparts, Fig.3-1. The mechanisms underlying this enhanced strain-rate sensitivity are not fully understood at present, probably due to the enhanced strain rate sensitivity of the intercrystalline grain boundary regions, relative to the

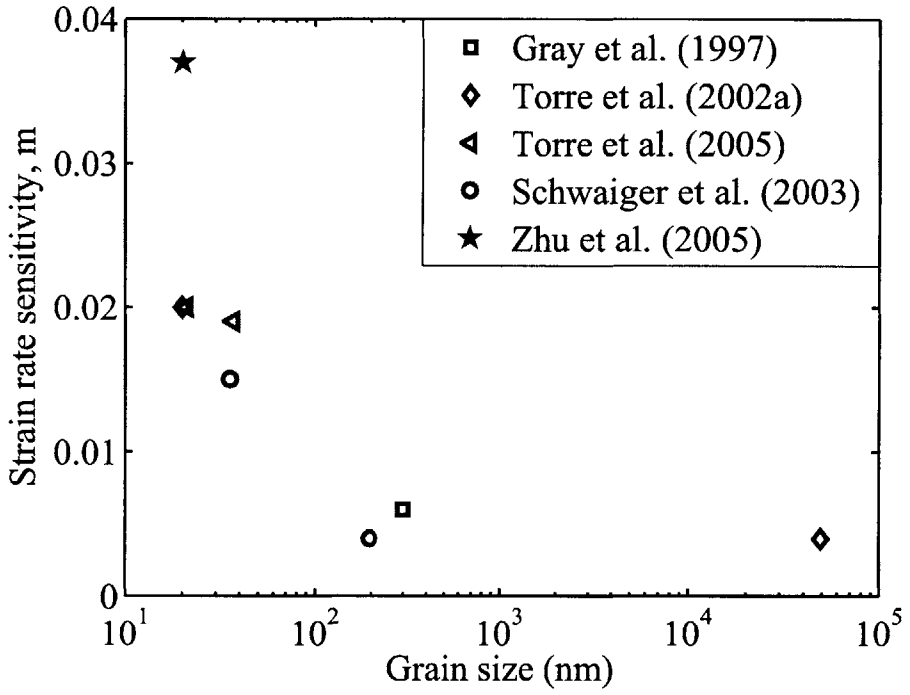

Figure 3-1: Strain-rate sensitivity parameter $m \stackrel{\text{def}}{=} \partial \ln \sigma / \partial \ln \dot{\epsilon}^p$ versus grain size for fcc nickel. The value of m increases as the grain size decreases in the nanocrystalline regime.

rate sensitivity of the crystalline grain interiors.

- The ductility of these materials, as measured by elongation in tensile experiments, is significantly reduced from the values observed for their microcrystalline counterparts, and seldom exceeds 5%. Since this occurs even for materials at the high end of grain sizes in the nanocrystalline range ($\sim 100\,\text{nm}$), one can infer that even though there is some accommodation of the overall imposed deformation by dislocation-mediated plasticity in the grain interiors, this accommodation is insufficient. Additionally, *intergranular accommodation mechanisms*, such as cavitation and micro-cracking, must be operative. It must be noted that widespread distributed grain boundary damage prior to final macroscopic fracture has not been experimentally observed; however, atomistic simulation studies do show grain-boundary nano-void formation and decohesion leading to intergranular fracture in these materials (Farkas et al., 2002; Sansoz and Molinari, 2004; Farkas et al., 2005).

As reviewed in (Kumar et al., 2003; Wolf et al., 2005; Meyers et al., 2006), much of the understanding of the micromechanisms operative during the inelastic deformation of nanocrystalline materials has been obtained from the large-scale molecular dynamics (MD) studies published in the past few years. Although such MD methods of studying atomic-level mechanical response of materials are useful for gaining valuable insight, these methods are at present not suitable for carrying out simulations of deformation and failure under conditions similar to those under which physical experiments on nanocrystalline materials are carried out: (i.e.) that is, macroscopic-sized specimens with complicated boundary conditions, involving realistic strain rates. MD simulations are inherently limited to small, idealized microstructures and extremely high strain rates, typically $> 10^7/\text{s}$, which corresponds to a strain of 1% in 1 ns.

In contrast to MD methods, finite element methods (FEM) for simulation of micromechanical interactions and prediction of local as well as overall response of materials have been effectively used to study the mechanical response of variety of composite material systems in recent years, and such methods do not possess the major limita-

tions of the MD methods listed above. However, use of continuum-mechanical-based FEM methods is contingent upon the assumptions of continuum mechanics – suitable smoothness of displacement fields, the notion of stress, and balance laws of linear and angular momentum — continuing to hold at the nanoscale. Further, just as the results from MD simulations depend crucially on the reliability of the interatomic potentials used in such studies, the results of FEM simulations depend crucially on the reliability of the continuum-level constitutive equations used in such analyses. While the concepts of continuum elasticity are expected to be approximately applicable at small scales approaching the nano-level, the concepts of classical continuum plasticity being applicable at this scale is highly questionable. Nevertheless, based on a *pragmatic engineering approach*, and bolstered by the success of (length-scale-independent) crystal-plasticity theories and attendant FEM simulation methodologies to represent grain-scale shear localization phenomena and texture evolution (cf., e.g, Anand and Kalidindi (1994)), a few investigators have recently carried out continuum-level FEM simulations of the inelastic deformation and failure response of nanocrystalline materials (Fu et al., 2001, 2004; Schwaiger et al., 2003; Wei and Anand, 2004; Sansoz and Molinari, 2004). Although in their infancy, such FEM-based simulations provide valuable insights on the deformation and failure response of nanocrystalline materials, which cannot be obtained solely from atomistic simulations or experiments.

For example, Schwaiger et al. (2003) idealize a nanocrystalline material as a two-dimensional composite of hexagonal-shaped crystalline grain interiors, surrounded by grain boundary layers of finite thickness — a "core-and-mantle" model. In such a model, as the grain size is reduced, the ratio between the volume fractions of the grain boundary "mantle" and the crystalline "core" increases. The ratio of the finite grain boundary thickness to the grain diameter serves as the relative material length scale in the model, and gives rise to grain-size effects. Schwaiger et al. (2003) used an isotropic plasticity theory for the grain-interiors as well as the grain boundary regions. They assumed that (i) the thickness of the grain boundary layer was $\sim$7 to 10 lattice parameters; (ii) the grain boundary regions had a lower initial yield strength than the grain interiors; (iii) both the grain interior and grain boundary

regions were taken to strain-harden isotropically; (iv) while the grain-interior was modeled as rate-independent, the grain boundary material was modeled to be strain-rate sensitive, with a strain-rate sensitivity parameter $m = 0.03$ in a standard power-law viscoplastic model. They also included a critical-plastic-strain-based criterion to model the initiation and progression of ductile failure. The focus of their study was the enhanced strain-rate sensitivity observed in nanocrystalline nickel relative to its microcrystalline counterpart, and their simple continuum level FEM model qualitatively reproduced the strain-rate sensitivity exhibited in the stress-strain curves from tension experiments on nanocrystalline Ni.[1]

Fu et al. (2001, 2004) have also used a "core-and-mantle" model for nanocrystalline materials. In contrast to Schwaiger et al. (2003), in their most recent paper (Fu et al., 2004), in order to account for the elastic and plastic anisotropy in these materials, model the grain interiors using a standard crystal-plasticity theory. Further, in order to represent the ease of dislocation generation at grain boundaries, the grain boundary regions were modeled using either: (i) an isotropic plasticity model with a lower yield strength and more rapidly strain-hardening rate than the grain interior; and (ii) a crystal plasticity model with a lower initial crystal slip resistance, but a higher saturation shear strength than the slip resistance for the grain interior.[2] Their simulations show realistic-looking distributions of inelastic deformation and shear localization in the polycrystalline aggregates. However, given the distinct diminution of dislocation activity in the nanocrystalline regime, their focus on variation of strain-hardening effects between grain interiors and grain boundary regions, which can only arise when there are large number of dislocations to interact with each other, seems not to be physically well-founded for materials with small grain-sizes in

[1]In passing, we note that in light of the high-resolution TEM micrographs of nanocrystalline materials, which show that for high-angle grain-boundaries, disordered grain-boundary regions are typically $\lesssim 1\,\text{nm}$ (Ranganathan et al., 2001), the use by Schwaiger et al. (2003) of a grain boundary-affected zone of the order of 7 to 10 lattice parameter (lattice parameter of Ni $\equiv 0.352\,\text{nm}$), is not a realistic geometric representation of the microstructure of nanocrystalline materials.

[2]They also used a more complex model involving a continuous change in strain hardening from the grain interior to the grain boundary based on the spatial gradients in orientation of the maximum shear stress in the polycrystalline aggregate. We do not quite comprehend the physical basis, nor the mathematical details of such a model.

the nanocrystalline regime. Also, although they use a rate-dependent crystal plasticity model, they do not report on the overall strain-rate sensitivity exhibited by their numerically-calculated stress-strain curves; however, this was not the focus of their study.

In contrast to the "core-and-mantle" type models, and given the uncertainties of ascribing a finite width to grain boundaries, Wei and Anand (2004) developed an alternate modeling approach to account for the combined effects of grain-boundary-related deformation as well as dislocation-mediated plasticity within the grains. They coupled a single-crystal plasticity constitutive model for the grain interior, with a new cohesive interface constitutive model to account for grain-boundary sliding and separation phenomena. They recognized that a standard crystal plasticity model for the grain-interior deformation, which implicitly assumes enough dislocation nucleation and multiplication to result in a sufficiently smooth macroscopic response, is inadequate to represent the limited amount of inelastic deformation due to emission and eventual absorption of the relatively fewer (partial or complete) dislocations from grain boundaries in nanocrystalline materials. However, since elastic anisotropy and crystallographic texture effects are still important in nanocrystalline materials, and since the few dislocations in these materials are still expected to move on slip systems, the mathematical structure of a continuum crystal plasticity theory is still useful as an *indicator* of the limited inelasticity due to crystalline slip within the nanocrystalline grains. Their cohesive interface model for grain boundaries accounts for both reversible elastic, as well irreversible inelastic sliding-separation deformations at the grain boundaries prior to failure. The tensile and shear properties of the cohesive grain boundaries were estimated by fitting results of numerical simulations to experimentally-measured stress-strain curves for nanocrystalline electrodeposited Ni. Unfortunately, such a fitting procedure makes it difficult to unambiguously characterize the grain boundary properties, and they used a value for the shear strength of the grain boundaries which was very similar in magnitude to the tensile strength of the boundaries; as is clear from the recent atomistic simulations of grain boundary response by Sansoz and Molinari (2004), this assumption is clearly unrealistic.

Also, Wei and Anand (2004) restricted their models for the grain-interiors and grain boundaries to be completely rate-independent.

Finally, following the methodology of Wei and Anand (2004), Warner et al. (2006) have very recently used a continuum FEM method to model the plastic deformation of nanocrystalline copper by using crystal plasticity for the grain interiors and cohesive elements for grain boundaries. For the traction-separation relations for the grain boundaries, they obtained estimates for the shear and normal response of the boundaries from quasi-continuum atomistic calculations. Since their atomistic calculations were carried out at 0 K, they had to use a *large* ad-hoc *thermal-correction* (cf., their eq. (8)) to estimate the shear strength for the grain boundaries in Cu at room temperature.

As is clear from our brief review, continuum-level FEM simulations of the inelastic deformation and failure response of nanocrystalline materials are still in their infancy. Much needs to be done to refine the constitutive models, specially for the grain boundary regions in "core-and-mantle"-type geometric representations of nanocrystalline materials, or the traction-separation relations in approaches using cohesive elements to represent grain-boundaries. Motivated by the fact that

- *amorphous metals are the ultimate limit for nanocrystalline metals, as the crystal grain size decreases to zero,*

and that

- *a new strain-rate-dependent continuum-plasticity theory for amorphous metals at low homologous temperatures is now available* (Anand and Su, 2005; Su and Anand, 2006),

we have developed slightly more refined constitutive models to represent the intercrystalline grain boundary regions, as well as the crystalline grain interiors in a "core-and-mantle"-type approach to model the deformation and failure response of nanocrystalline materials. It is the purpose of this chapter to report on our constitutive models and the results from our numerical simulations. Specifically, we have

1. Developed a modified version of the rate-dependent amorphous plasticity model of Anand and Su (Anand and Su, 2005; Su and Anand, 2006) to account for cavitation and related failure phenomena, and used such a model to represent the grain boundary response of nanocrystalline materials.

2. Accounted for the transition from partial dislocation to complete dislocation mediated plasticity for the grain interiors. This development is based on the recent work of Zhu et al. (2005).

The plan of this chapter is as follows. The amorphous plasticity model we have adopted to represent the rate-dependent deformation and failure of grain boundaries is outlined in Section 2. In Section 3, we outline the model that we have used to represent grain interior plasticity due to partial or perfect dislocations. In Section 4 we study the response of a prototypical grain-boundary as modelled by our theory for amorphous materials. Numerical representation of two-dimensional microstructures with different grain sizes is briefly discussed in Section 5. Applications of the model to represent the deformation and failure response of Ni over a range of grain sizes in the nanocrystalline regime are reported in Section 6. We close in Section 7 with some final remarks.

3.2 A constitutive model for the elastic-viscoplastic deformation of grain boundaries

Our continuum-mechanical constitutive model for the intercrystalline grain-boundary regions in nanocrystalline materials is based on a modification of the theory of Anand and Su (Anand and Su, 2005; Su and Anand, 2006) for amorphous metallic materials. It involves the following major kinematical ideas:[3]

[3] *Notation*: ∇ and Div denote the gradient and divergence with respect to the material point $\mathbf{X}$ in the *reference configuration*; grad and div denote these operators with respect to the point $\mathbf{x} = \boldsymbol{\chi}(\mathbf{X}, t)$ in the deformed configuration; a superposed dot denotes the material time-derivative. Throughout, we write $\mathbf{F}^{e-1} = (\mathbf{F}^e)^{-1}$, $\mathbf{F}^{p-\mathsf{T}} = (\mathbf{F}^p)^{-\mathsf{T}}$, etc. We write $\operatorname{sym}\mathbf{A}$, $\operatorname{skw}\mathbf{A}$, $\mathbf{A}_0$, and $\operatorname{sym}_0\mathbf{A}$ respectively, for the symmetric, skew, deviatoric, and symmetric-deviatoric parts of a tensor $\mathbf{A}$. Also, the inner product of tensors $\mathbf{A}$ and $\mathbf{B}$ is denoted by $\mathbf{A} : \mathbf{B}$, and the magnitude of $\mathbf{A}$ by $|\mathbf{A}| = \sqrt{\mathbf{A} : \mathbf{A}}$.

(i) the decomposition

$$\mathbf{F} = \mathbf{F}^e \mathbf{F}^p \tag{3.2}$$

of the deformation gradient $\mathbf{F} = \nabla \boldsymbol{\chi}$ into *elastic* and *plastic* parts $\mathbf{F}^e$ and $\mathbf{F}^p$ (Kröner, 1960; Lee, 1969); and

(ii) the evolution equation

$$\dot{\mathbf{F}}^p = \mathbf{D}^p \mathbf{F}^p, \qquad \mathbf{D}^p = \mathbf{D}^{p\top}, \tag{3.3}$$

for $\mathbf{F}^p$. The plastic stretching is taken to arise from a shearing contribution $\mathbf{D}_s^p$ controlled by the local shear stresses, and a cavitating/volumetric contribution $\mathbf{D}_c^p$ controlled by the local tensile principal stresses and the local mean normal stress:

$$\mathbf{D}^p = \mathbf{D}_s^p + \mathbf{D}_c^p \,. \tag{3.4}$$

(iii) We assume that $\mathbf{D}_s^p$ occurs by shearing relative to some orthonormal "slip systems," labelled by integers α; each slip system is specified by a slip direction $\mathbf{s}^\alpha$, and a slip plane normal $\mathbf{m}^\alpha$. For an amorphous isotropic material there are no preferred directions other than the principal directions of stress; accordingly we take these slip systems $(\mathbf{s}^\alpha, \mathbf{m}^\alpha)$ to be defined relative to the principal directions of stress $\{\hat{\mathbf{e}}_1, \hat{\mathbf{e}}_2, \hat{\mathbf{e}}_3\}$ (cf., eq. (3.15)). We emphasize that these slip systems are not the classical slip systems of crystal plasticity, but are related to the principal directions of the stress, and they change both spatially and temporally as the principal directions of stress change in a non-homogeneously deforming material. Thus, $\mathbf{D}_s^p$ is given by

$$\mathbf{D}_s^p = \sum_\alpha \nu^{(\alpha)} \operatorname{sym}\left(\mathbf{s}^{(\alpha)} \otimes \mathbf{m}^{(\alpha)}\right). \tag{3.5}$$

The constitutive equation for the scalar shearing rates $\nu^{(\alpha)}$ on each slip system

is taken in a simple power-law form

$$\nu^{(\alpha)} = \nu_0 \left\{ \frac{\tau^{(\alpha)}}{c + \mu\sigma^{(\alpha)}} \right\}^{1/m} > 0, \tag{3.6}$$

where $\tau^{(\alpha)}$ and $\sigma^{(\alpha)}$ are the resolved shear stress and compressive traction on each slip sytem; $c > 0$ and $\mu \geq 0$ are internal variables called the *cohesion* and *internal friction*, respectively; also, ν_0 is a *reference plastic shear strain rate*, and $m > 0$ is a *strain-rate sensitivity parameter.*

In the theory of Anand and Su (2005), the shearing (3.5) is accompanied by a small amount of shear-induced dilatation, which gives rise to a small change in the free-volume of the material. It is commonly believed that for amorphous materials the increase of the free-volume is the major reason for the post-yield strain-softening and formation of shear bands in metallic glasses. In Anand and Su (2005) this is accounted for by making the cohesion c decrease as the free volume increases. However, given the uncertainities in various aspects of continuum modeling of nanocrystalline materials, in the application of the amorphous plasticity theory to represent the behavior of narrow grain-boundary layers, we take c to be *constant.*

(iv) With $\{\sigma_1, \sigma_2, \sigma_3\}$, and $\{\hat{\mathbf{e}}_1, \hat{\mathbf{e}}_2, \hat{\mathbf{e}}_3\}$ denoting the principal stresses and principal stress-directions, the constitutive equation for cavitating/volumetric contribution $\mathbf{D}_c^p$ to the plastic stretching is taken to be given by

$$\mathbf{D}_c^p = \sum_{i=1}^{3} \nu_c^{(i)} (\hat{\mathbf{e}}_i \otimes \hat{\mathbf{e}}_i), \qquad \nu_c^{(i)} \geq 0, \quad i = 1, 2, 3, \tag{3.7}$$

with

$$\nu_c^{(i)} = \begin{cases} \nu_0 \left\{ \dfrac{\sigma_i}{\sigma_{cr}} \right\}^{1/m} & \text{if } \sigma_i > 0, \\ 0 & \text{if } \sigma_i \leq 0, \end{cases} \tag{3.8}$$

$$\sigma_{cr} = c_1 - c_2 \bar{\sigma}_h > 0, \tag{3.9}$$

where

$$\bar{\sigma}_h = (1/3)(\sigma_1 + \sigma_2 + \sigma_3), \tag{3.10}$$

is the mean normal stress (hydrostatic tension), and c_1 and c_2 are material parameters.

In this model the contribution $\nu_c^{(i)}(\hat{\mathbf{e}}_i \otimes \hat{\mathbf{e}}_i)$ to $\mathbf{D}_c^p$ is zero if the principal stress σ_i is zero or negative. When σ_i is positive, its value relative to the value of a parameter $\sigma_{cr} = \hat{\sigma}_{cr}(\bar{\sigma}_h)$ which depends on the hydrostatic tension, controls the magnitude of $\nu_c^{(i)}$. The value of σ_{cr} is taken to decrease linearly as the hydrostatic tension $\bar{\sigma}_h$ increases, eq. (3.9). For simplicity, the reference strain rate ν_0, and the rate sensitivity parameter m in (3.8) are taken to be the same as that in (3.6).

Note that (3.7) and (3.8) predict a *spherical* inelastic cavitation only when all the principal stresses are equal to each other, $\sigma_1 = \sigma_2 = \sigma_3$. In situations where the principal stresses are unequal, the "cavitation" is predominantly in the direction of the maximum principal stress σ_1 because of the power-law nature of the relation (3.8).[4]

Further details of the development of the theory are given in Anand and Su (2005). Here we simply summarize the resulting special constitutive equations. The underlying constitutive equations relate the following basic fields:

[4]This situation corresponds closely to maximum principal stress-dependent "crazing" in amorphous polymeric materials.

$\boldsymbol{\chi}$,		motion,
$\mathbf{F} = \nabla\boldsymbol{\chi}$,	$J = \det\mathbf{F} > 0$,	deformation gradient,
$\mathbf{F}^p$,	$J^p = \det\mathbf{F}^p > 0$,	plastic deformation gradient,
$\mathbf{F}^e = \mathbf{F}\mathbf{F}^{p-1}$,	$J^e = \det\mathbf{F}^e > 0$,	elastic deformation gradient,
$\mathbf{F}^e = \mathbf{R}^e\mathbf{U}^e$,		polar decomposition of $\mathbf{F}^e$,
$\mathbf{U}^e = \sum_{\alpha=1}^3 \lambda_\alpha^e \mathbf{r}_\alpha \otimes \mathbf{r}_\alpha$,		spectral decomposition of $\mathbf{U}^e$,
$\mathbf{E}^e = \sum_{\alpha=1}^3 (\ln\lambda_\alpha^e)\mathbf{r}_\alpha \otimes \mathbf{r}_\alpha$,		logarithmic elastic strain,
$\mathbf{T}$,	$\mathbf{T} = \mathbf{T}^\top$,	Cauchy stress,
$\mathbf{T}^e = \mathbf{R}^{e\top}(J^e\mathbf{T})\mathbf{R}^e$,		stress conjugate to elastic strain $\mathbf{E}^e$,
$c > 0$,		cohesion,
$\mu \geq 0$,		internal friction coefficient,
$\phi = \arctan\mu$,		internal friction angle,

The set of constitutive equations is summarized below:

1. **Equation for the stress:**

$$\mathbf{T}^e = 2G\mathbf{E}_0^e + K\,(\mathrm{tr}\,\mathbf{E}^e)\mathbf{1}, \tag{3.11}$$

with G and K the elastic shear modulus and bulk modulus, respectively.

This symmetric stress tensor $\mathbf{T}^e$ has the spectral representation

$$\mathbf{T}^e = \sum_{i=1}^{3} \sigma_i\,\hat{\mathbf{e}}_i \otimes \hat{\mathbf{e}}_i, \tag{3.12}$$

where $\{\sigma_i | i = 1,2,3\}$ are the principal values, and $\{\hat{\mathbf{e}}_i | i = 1,2,3\}$ are the orthonormal principal directions of $\mathbf{T}^e$. We assume that the principal stresses $\{\sigma_i | i = 1,2,3\}$ are strictly ordered such that

$$\sigma_1 \geq \sigma_2 \geq \sigma_3. \tag{3.13}$$

2. **Slip systems, resolved shear stress, and compressive normal traction:**

We assume that plastic flow occurs by shearing relative to some slip systems. Slip systems are labelled by integers α; each slip system is specified by a slip direction $\mathbf{s}^\alpha$, and a slip plane normal $\mathbf{m}^\alpha$ with

$$\mathbf{s}^{(\alpha)} \cdot \mathbf{m}^{(\alpha)} = 0, \qquad |\mathbf{s}^{(\alpha)}|,\ |\mathbf{m}^{(\alpha)}| = 1. \tag{3.14}$$

As discussed previously, for an amorphous isotropic material there are no preferred directions other than the principal directions of stress, and accordingly we consider plastic flow to be possible on six potential slip systems defined relative to the principal directions of stress $\mathbf{T}^e$:

$$\left.\begin{aligned}
\mathbf{s}^{(1)} &= \cos\vartheta\hat{\mathbf{e}}_1 + \sin\vartheta\hat{\mathbf{e}}_3, & \mathbf{m}^{(1)} &= \sin\vartheta\hat{\mathbf{e}}_1 - \cos\vartheta\hat{\mathbf{e}}_3,\\
\mathbf{s}^{(2)} &= \cos\vartheta\hat{\mathbf{e}}_1 - \sin\vartheta\hat{\mathbf{e}}_3, & \mathbf{m}^{(2)} &= \sin\vartheta\hat{\mathbf{e}}_1 + \cos\vartheta\hat{\mathbf{e}}_3,\\
\mathbf{s}^{(3)} &= \cos\vartheta\hat{\mathbf{e}}_1 + \sin\vartheta\hat{\mathbf{e}}_2, & \mathbf{m}^{(3)} &= \sin\vartheta\hat{\mathbf{e}}_1 - \cos\vartheta\hat{\mathbf{e}}_2,\\
\mathbf{s}^{(4)} &= \cos\vartheta\hat{\mathbf{e}}_1 - \sin\vartheta\hat{\mathbf{e}}_2, & \mathbf{m}^{(4)} &= \sin\vartheta\hat{\mathbf{e}}_1 + \cos\vartheta\hat{\mathbf{e}}_2,\\
\mathbf{s}^{(5)} &= \cos\vartheta\hat{\mathbf{e}}_2 + \sin\vartheta\hat{\mathbf{e}}_3, & \mathbf{m}^{(5)} &= \sin\vartheta\hat{\mathbf{e}}_2 - \cos\vartheta\hat{\mathbf{e}}_3,\\
\mathbf{s}^{(6)} &= \cos\vartheta\hat{\mathbf{e}}_2 - \sin\vartheta\hat{\mathbf{e}}_3, & \mathbf{m}^{(6)} &= \sin\vartheta\hat{\mathbf{e}}_2 + \cos\vartheta\hat{\mathbf{e}}_3,
\end{aligned}\right\} \tag{3.15}$$

where

$$\vartheta = \frac{\pi}{4} + \frac{\phi}{2}. \tag{3.16}$$

and

$$\phi \stackrel{\text{def}}{=} \arctan\mu \tag{3.17}$$

is an *angle of internal friction*, and $\mu \geq 0$ is a *friction coefficient.*

The resolved shear and compressive normal traction on each slip system are given by

$$\tau^{(\alpha)} \stackrel{\text{def}}{=} \mathbf{s}^{(\alpha)} \cdot \mathbf{T}^e\mathbf{m}^{(\alpha)}, \qquad \sigma^{(\alpha)} \stackrel{\text{def}}{=} -\mathbf{m}^{(\alpha)} \cdot \mathbf{T}^e\mathbf{m}^{(\alpha)}. \tag{3.18}$$

3. **Flow rule**:

The evolution equation for $\mathbf{F}^p$ is

$$\dot{\mathbf{F}}^p = \mathbf{D}^p \mathbf{F}^p, \qquad \mathbf{F}^p(\mathbf{X}, 0) = \mathbf{1}, \tag{3.19}$$

with

$$\mathbf{D}^p = \mathbf{D}^p_s + \mathbf{D}^p_c \,. \tag{3.20}$$

The shearing contribution $\mathbf{D}^p_s$ is given by

$$\left.\begin{aligned} \mathbf{D}^p &= \sum_{\alpha=1}^{6} \nu^{(\alpha)} \operatorname{sym}\left(\mathbf{s}^{(\alpha)} \otimes \mathbf{m}^{(\alpha)}\right) \\ \nu^{(\alpha)} &= \nu_0 \left\{ \frac{\tau^{(\alpha)}}{c + \mu\sigma^{(\alpha)}} \right\}^{1/m} \geq 0 \end{aligned}\right\}, \tag{3.21}$$

where $c > 0$ is an internal variable called the *cohesion*, and $\mu \geq 0$ is an internal friction coefficient. Also, ν_0 is a *reference plastic shear strain rate*, and $m > 0$ is a *strain-rate sensitivity parameter.*

The volumetric contribution $\mathbf{D}^p_c$ is given by

$$\left.\begin{aligned} \mathbf{D}^p_c &= \sum_{i=1}^{3} \nu^{(i)}_c (\hat{\mathbf{e}}_i \otimes \hat{\mathbf{e}}_i), \qquad \nu^{(i)}_c \geq 0 \\ \nu^{(i)}_c &= \begin{cases} \nu_0 \left\{ \dfrac{\sigma_i}{\sigma_{cr}} \right\}^{1/m} & \text{if } \sigma_i > 0 \\ 0 & \text{if } \sigma_i \leq 0 \end{cases} \\ \sigma_{cr} &= c_1 - c_2 \bar{\sigma}_h > 0 \end{aligned}\right\}, \tag{3.22}$$

where

$$\bar{\sigma}_h = \frac{1}{3}\Big(\sigma_1 + \sigma_2 + \sigma_3\Big) \tag{3.23}$$

is the mean normal stress. Here c_1 and c_2 are material constants, and the constants ν_0 and m are taken to have the same values as those in (3.21).

3.2.1 Modeling of damage and failure of grain boundaries

We use the following simple critical-strain-based criteria to model damage and failure of grain boundaries due to cavitation.

Let

$$\tilde{\epsilon}^p = |\mathbf{D}_c^p| \tag{3.24}$$

define a volumetric strain rate, and

$$\epsilon^p \stackrel{\text{def}}{=} \int_0^t \tilde{\epsilon}^p(\chi)\, d\xi, \tag{3.25}$$

define a volumetric plastic strain. Then, as a simple model for damage by inelastic cavitation, we introduce a damage variable D defined by

$$D \stackrel{\text{def}}{=} \begin{cases} 0 & \text{if } \epsilon^p \leq \epsilon^p_{cr}, \\ \dfrac{(\epsilon^p - \epsilon^p_{cr})}{(\epsilon^p_f - \epsilon^p_{cr})} & \text{if } \epsilon^p_{cr} < \epsilon^p < \epsilon^p_f, \\ 1 & \text{if } \epsilon^p \geq \epsilon^p_f, \end{cases} \tag{3.26}$$

whose value is zero for ϵ^p less than a critical value ϵ^p_{cr}, and thereafter $D = (\epsilon^p - \epsilon^p_{cr})/(\epsilon^p_f - \epsilon^p_{cr})$, so that the damage variable evolves linearly towards a value of unity as ϵ^p evolves to a failure value ϵ^p_f. Correspondingly, the σ_{cr} in $(3.22)_3$ is decreased linearly towards a value of zero

$$\sigma_{cr} = \{c_1 - c_2\bar{\sigma}_h\} \times (1 - D) > 0\,. \tag{3.27}$$

As σ_{cr} approaches zero with increasing D, the material is deemed to have "failed" by cavitation, and it is "removed" from the finite element calculation.

Further, to account for the degradation of elastic properties due to damage, the elastic shear and bulk moduli G and K are replaced by

$$G \Rightarrow G \times (1 - D), \qquad \text{and} \qquad K \Rightarrow K \times (1 - D) \tag{3.28}$$

when damage occurs.[5] The damage model outlined above is quite rudimentary, and much work needs to be done to develop more realistic models for the transition from shear plasticity, to actual dilatant plasticity, damage and final fracture.

3.3 Constitutive model for grain interior response

We shall employ the following classical framework of rate-dependent single-crystal plasticity (e.g., Asaro and Needleman (1985); Kalidindi et al. (1992); Bronkhorst et al. (1992)). Single-crystal plasticity is based on the hypothesis that plastic flow takes place through slip on prescribed crystallographic slip systems $\alpha = 1, 2, \ldots, N$, with each system α defined by a slip direction $\mathbf{s}_0^\alpha$ and a slip-plane normal $\mathbf{m}_0^\alpha$, where

$$\mathbf{s}_0^\alpha \cdot \mathbf{m}_0^\alpha = 0, \qquad |\mathbf{s}_0^\alpha|, |\mathbf{m}_0^\alpha| = 1, \qquad \mathbf{s}_0^\alpha, \mathbf{m}_0^\alpha = \text{constant}. \tag{3.29}$$

For a material with slip systems $\alpha = 1, 2, \ldots, N$ defined by orthonormal vector pairs $(\mathbf{m}_0^\alpha, \mathbf{s}_0^\alpha)$, the constitutive equations relate the following basic fields:

$\boldsymbol{\chi}$,		motion,
$\mathbf{F} = \nabla\boldsymbol{\chi}$,	$J = \det\mathbf{F} > 0$,	deformation gradient,
$\mathbf{F}^p$,	$J^p = \det\mathbf{F}^p = 1$,	plastic deformation gradient,
$\mathbf{F}^e = \mathbf{F}\mathbf{F}^{p-1}$,	$J^e = \det\mathbf{F}^e > 0$,	elastic deformation gradient,
$\mathbf{C}^e = \mathbf{F}^{e\top}\mathbf{F}^e$,		elastic right Cauchy-Green tensor,
$\mathbf{E}^e = \frac{1}{2}(\mathbf{C}^e - \mathbf{1})$,		elastic strain,
$\mathbf{T}$, $\quad \mathbf{T} = \mathbf{T}^\top$,		Cauchy stress,
$\mathbf{T}^e = (\det\mathbf{F}^e)\mathbf{F}^{e-1}\mathbf{T}\mathbf{F}^{e-\top}$,		stress conjugate to $\mathbf{E}^e$,
$s^\alpha > 0$,		slip resistances.

The constitutive theory, intended to characterize small elastic strains, is summarized below.

[5] In actual numerical implementation, in order to avoid numerical singularities, failure due to cavitation is deemed to have occurred when the damage parameter D_c reaches a suitably large number, say ~ 0.995.

1. The *elastic stress-strain relation* has the form

$$\mathbf{T}^e = \mathbb{C}[\mathbf{E}^e], \tag{3.30}$$

where $\mathbb{C}$ is the anisotropic elasticity tensor. For cubic materials $\mathbb{C}$ has only three independent constants, which are traditionally denoted by C_{11}, C_{12}, C_{44}.

2. The *flow rule*, defined by an evolution equation for $\mathbf{F}^p$ of the form

$$\dot{\mathbf{F}}^p = \mathbf{L}^p\mathbf{F}^p, \qquad \mathbf{L}^p = \sum_{\alpha=1}^{N} \nu^\alpha \, \mathbf{s}_0^\alpha \otimes \mathbf{m}_0^\alpha, \qquad \mathbf{F}^p(0) = \mathbf{1}, \tag{3.31}$$

with the microshear rates ν^α determined by specific constitutive functions

$$\nu^\alpha = \hat{\nu}^\alpha(\tau^\alpha, s^\alpha)\,, \tag{3.32}$$

where

$$\tau^\alpha = \mathbf{s}_0^\alpha \cdot (\mathbf{C}^e\mathbf{T}^e)\mathbf{m}_0^\alpha, \tag{3.33}$$

is the *resolved stress* on the αth slip system , and s^α is a slip system deformation resistance, which for nanocrystalline materials are taken to be grain-size-dependent *constants*: that is (i.e.), no strain-hardening (cf. eqs. (3.35) and (3.37)).

Let Γ denote the stacking fault energy of an fcc material,

$$G \stackrel{\text{def}}{=} \sqrt{\frac{(C_{11} - C_{12})C_{44}}{2}}$$

a nominal shear modulus, and b the magnitude of the Burgers vector of a *perfect dislocation*. Then, according to a model of Asaro et al. (2003; 2005),

- *there exists a critical grain size d_c given by*

$$d_c \approx \frac{2}{3}\Big(\frac{Gb^2}{\Gamma}\Big), \tag{3.34}$$

α	$\mathbf{m}_0^\alpha$	$\mathbf{s}_0^\alpha$ For $d > d_c$
1	(111)	$[01\bar{1}]$
2	(111)	$[\bar{1}01]$
3	(111)	$[1\bar{1}0]$
4	$(\bar{1}\bar{1}1)$	$[01\bar{1}]$
5	$(\bar{1}\bar{1}1)$	$[101]$
6	$(\bar{1}\bar{1}1)$	$[\bar{1}10]$
7	$(\bar{1}11)$	$[01\bar{1}]$
8	$(\bar{1}11)$	$[101]$
9	$(\bar{1}11)$	$[\bar{1}\bar{1}0]$
10	$(1\bar{1}1)$	$[0\bar{1}\bar{1}]$
11	$(1\bar{1}1)$	$[\bar{1}01]$
12	$(1\bar{1}1)$	$[110]$

α	$\mathbf{m}_0^\alpha$	$\mathbf{s}_0^\alpha$ For $d \leq d_c$
1	(111)	$[\bar{2}11]$
2	(111)	$[1\bar{2}1]$
3	(111)	$[11\bar{2}]$
4	$(\bar{1}\bar{1}1)$	$[2\bar{1}1]$
5	$(\bar{1}\bar{1}1)$	$[\bar{1}21]$
6	$(\bar{1}\bar{1}1)$	$[\bar{1}\bar{1}\bar{2}]$
7	$(\bar{1}11)$	$[211]$
8	$(\bar{1}11)$	$[\bar{1}\bar{2}1]$
9	$(\bar{1}11)$	$[\bar{1}1\bar{2}]$
10	$(1\bar{1}1)$	$[\bar{2}\bar{1}1]$
11	$(1\bar{1}1)$	$[121]$
12	$(1\bar{1}1)$	$[1\bar{1}\bar{2}]$

Table 3.1: Slip plane normals $\mathbf{m}_0^\alpha$ and slip directions $\mathbf{s}_0^\alpha$ for the 12 slip systems in an fcc crystal for full dislocations when the grain size $d > d_c$, as well as the 12 faulting systems for partial dislocations when $d \leq d_c$.

above which plastic deformation in nanocrystalline grain interiors occurs by the emission of **complete dislocations** *from grain boundaries, and below which the plastic deformation occurs by* **partial dislocations**.

The slip plane normals $\mathbf{m}_0^\alpha$ and slip directions $\mathbf{s}_0^\alpha$ for the 12 slip systems in an fcc crystal with full dislocations when the grain size $d > d_c$, are given in Table 3.1. For full dislocations, slip can occur in either the positive or negative $< 110 >$-type slip direction on a $\{111\}$-type plane. The 12 faulting systems for partial dislocations when $d \leq d_c$, are also listed in Table 3.1. Note that the faulting systems for partial dislocations are identical to the classical
$\{111\} < 11\bar{2} >$ *twin systems* for fcc materials, Staroselsky and Anand (1998). Like twinning, because the underlying atomic arrangement is polar in nature, we assume that faulting can occur in only one $< 11\bar{2} >$-type direction on a $\{111\}$ plane, and the faulting systems listed in Table 3.1 correspond to the easy direction of faulting.[6]

[6]Note that we do not explicitly consider twinning as an explicit deformation mechanism here.

For grain sizes $d > d_c$, grain interior plasticity occurs by emission of full dislocations from grain boundaries, the slip resistance s^α is given by

$$s^\alpha = \frac{Gb}{d}, \tag{3.35}$$

and the corresponding microshear rate is given by

$$\nu^\alpha = \begin{cases} \nu_0 \Big(\dfrac{|\tau^\alpha|}{s^\alpha} \Big)^{1/m} \operatorname{sign}(\tau^\alpha) & \text{if } |\tau^\alpha| > 0, \\ 0 & \text{otherwise} . \end{cases} \tag{3.36}$$

For grain sizes $d \leq d_c$, grain interior plasticity occurs by emission of partial dislocations from grain boundaries, the slip resistance s^α is given by[7]

$$s^\alpha = \frac{Gb}{3d}. \tag{3.37}$$

In this case there also exists a threshold resistance

$$s_{th} = \frac{\Gamma}{b}, \tag{3.38}$$

and the corresponding microshear rate is given by

$$\nu^\alpha = \begin{cases} \nu_0 \Big(\dfrac{\tau^\alpha - s_{th}}{s^\alpha} \Big)^{1/m} & \text{if } (\tau^\alpha - s_{th}) > 0, \\ 0 & \text{otherwise}. \end{cases} \tag{3.39}$$

3.4 Simulation of an amorphous grain boundary region

Before we proceed to the application of our plasticity theories to model the response of nanocrystalline materials, in this section we consider the deformation and failure

[7]The factor of 3 difference between the resistances given in (3.35) and (3.37) arises because the energy per unit length of full dislocations is $(1/2)Gb^2_{\text{full}}$, while that of partial dislocations is $(1/2)Gb^2_{\text{partial}}$, and $b_{\text{partial}} = b_{\text{full}}/\sqrt{3}$.

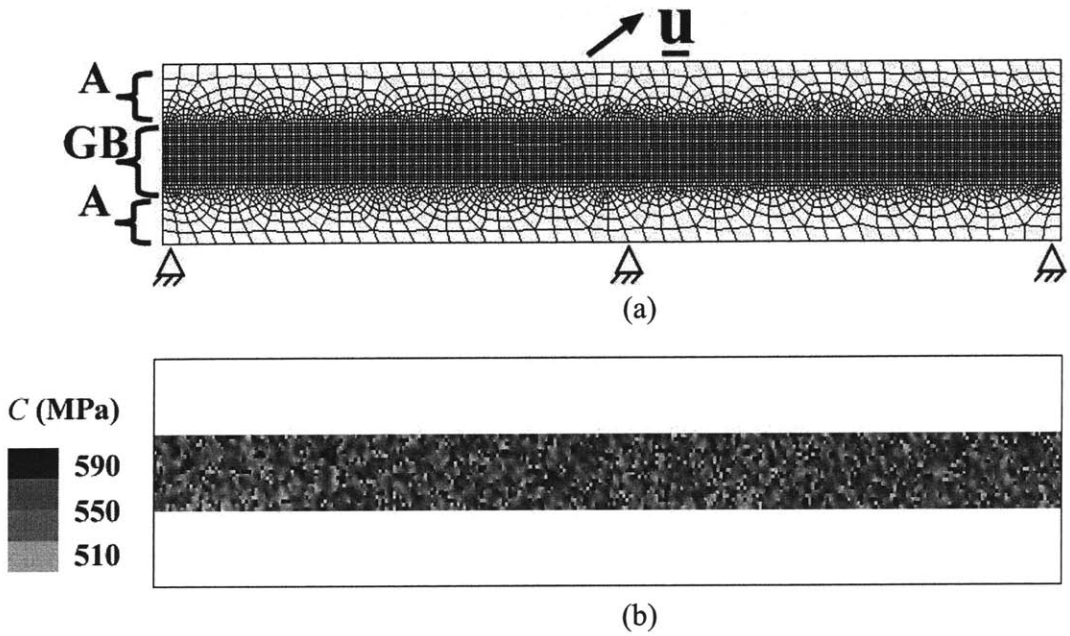

Figure 3-2: (a) An amorphous grain-boundary region "GB" sandwiched between elastic layers "A". The bottom edge of the sandwiched layer is held fixed, while $\underline{\mathbf{u}}$ denotes the displacement of the top edge (b) A contour plot of the initial cohesion c assigned to the grain-boundary elements before deformation; the initial value of c for each grain-boundary element was randomly assigned a value from a list which had values of c uniformly distributed between 510 and 590 MPa.

response of a prototypical "grain-boundary" as modelled by our theory for amorphous materials.

Fig. 3-2 a shows a finite element model of an amorphous grain-boundary region "GB" sandwiched between elastic layers "A". The bottom edge of the sandwiched layer is held fixed, while $\underline{\mathbf{u}}$ denotes the displacement of the top edge. Several material parameters are required in the constitutive model to describe the mechanical behavior of an amorphous grain boundary, cf. § 3.2. These include the elastic shear moduli G and K, the cohesion c, the frictional coefficient μ, the viscoplasticity parameters ν_0 and m; the critical strains for cavitation failure $\epsilon_{c,cr}$ and $\epsilon_{c,f}$, and the parameters c_1 and c_2 controlling the evolution of cavitation resistance σ_{cr}. In this section we have chosen representative values to qualitatively demonstrate the mechanical response of a grain-boundary.[8] *In order to model the heterogeneity of the grain boundaries,*

[8]The precise magnitudes of the grain boundary properties are not important here. They are

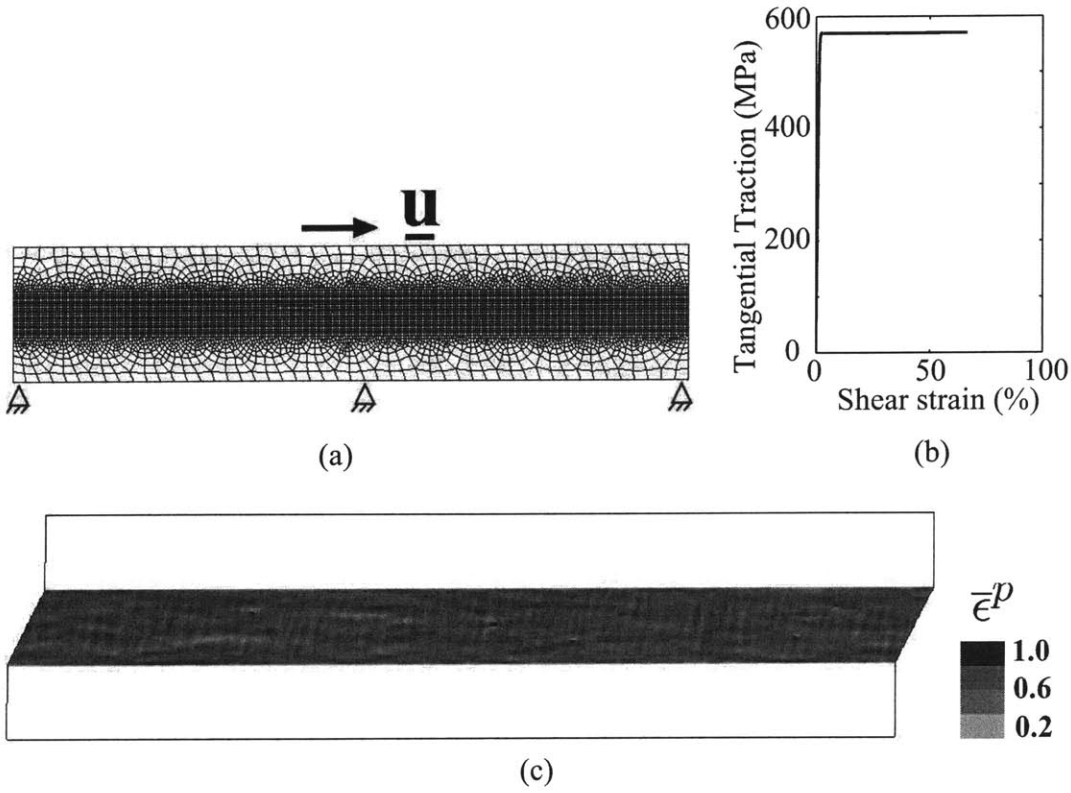

Figure 3-3: (a) Shear response of an amorphous grain-boundary region. The bottom edge of the sandwiched layer is held fixed, while the top edge is displaced by $\underline{\mathbf{u}}$ to produce a simple shear deformation. (b) Nominal shear stress versus shear strain response of the grain-boundary region in simple shear, using representative values of material parameters for the amorphous layer. (d) A contour plot of the equivalent plastic strain, showing inhomogeneous deformation in grain-boundary region after a shear strain of 50%.

the initial value of the cohesion c for each grain-boundary element was randomly assigned a value from a list which had values of c uniformly distributed between 510 and 590 MPa. Fig. 3-2 b shows a contour plot of the initial value of c in the grain-boundary region.

discussed in greater detail in § 3.6.2 where we apply our model to nc-Ni.

We first simulated the deformation of such an interface region to macroscopic simple shear, Fig. 3-3 a. In this simulation we *suppressed* the cavitation mechanism. The nominal shear stress versus shear strain response of the grain-boundary region using representative values of material parameters for the amorphous layer is shown in Fig. 3-3 b. A contour plot of the equivalent plastic strain, exhibiting inhomogeneous deformation involving "shear bands" in the grain-boundary region after a nominal macroscopic shear strain of 50% is shown in Fig. 3-3 c.

Next, cavitation failure in grain-boundary elements is also allowed. The top edge of the sandwich layer, cf. Fig.3-2, was given displacements $\underline{\mathbf{u}}_{90}$, $\underline{\mathbf{u}}_{45}$, and $\underline{\mathbf{u}}_{0}$, respectively. Figs. 3-4 a and b, respectively, show the resulting normal traction versus normal strain, and tangential traction versus tangential shear strain curves from the three simulations. Fig. 3-4 c shows the failure pattern corresponding to the point "X" marked on the normal traction versus normal strain curve in Fig. 3-4a for the case $\underline{\mathbf{u}}_{90}$. Cavities initiate in the grain-boundary region, grow and coalesce very quickly, and result in a progressive drop of the traction in the normal direction. Fig. 3-4 d shows the failure pattern corresponding to the point "X" marked on the normal traction versus normal strain curve in Fig. 3-4a for the case $\underline{\mathbf{u}}_{45}$. Finally, Fig. 3-4 e shows the failure pattern corresponding to the point "a" marked on the tangential traction versus shear strain curve in Fig. 3-4b for the case $\underline{\mathbf{u}}_{0}$. The tangential traction versus shear strain curve shown in Fig. 3-4 b indicates that even though there is some damage which initiates in the highly constrained regions, Fig.3-4 c, the shear strength of the grain boundary decreases only slightly in simple shear.

In nanocrystalline materials, it is the interplay between the response of "amorphous" grain boundaries and crystalline grain interiors that dictates the overall deformation and failure behavior. In the next section, we discuss how to numerically generate representative microstructures which include different relative volume fractions of grain boundaries and grain interiors. These microstructures, coupled with appropriate constitutive models, will enable us to numerically investigate the competition between the deformation of grain interiors and grain-boundary regions in nanocrystalline materials with different grain sizes.

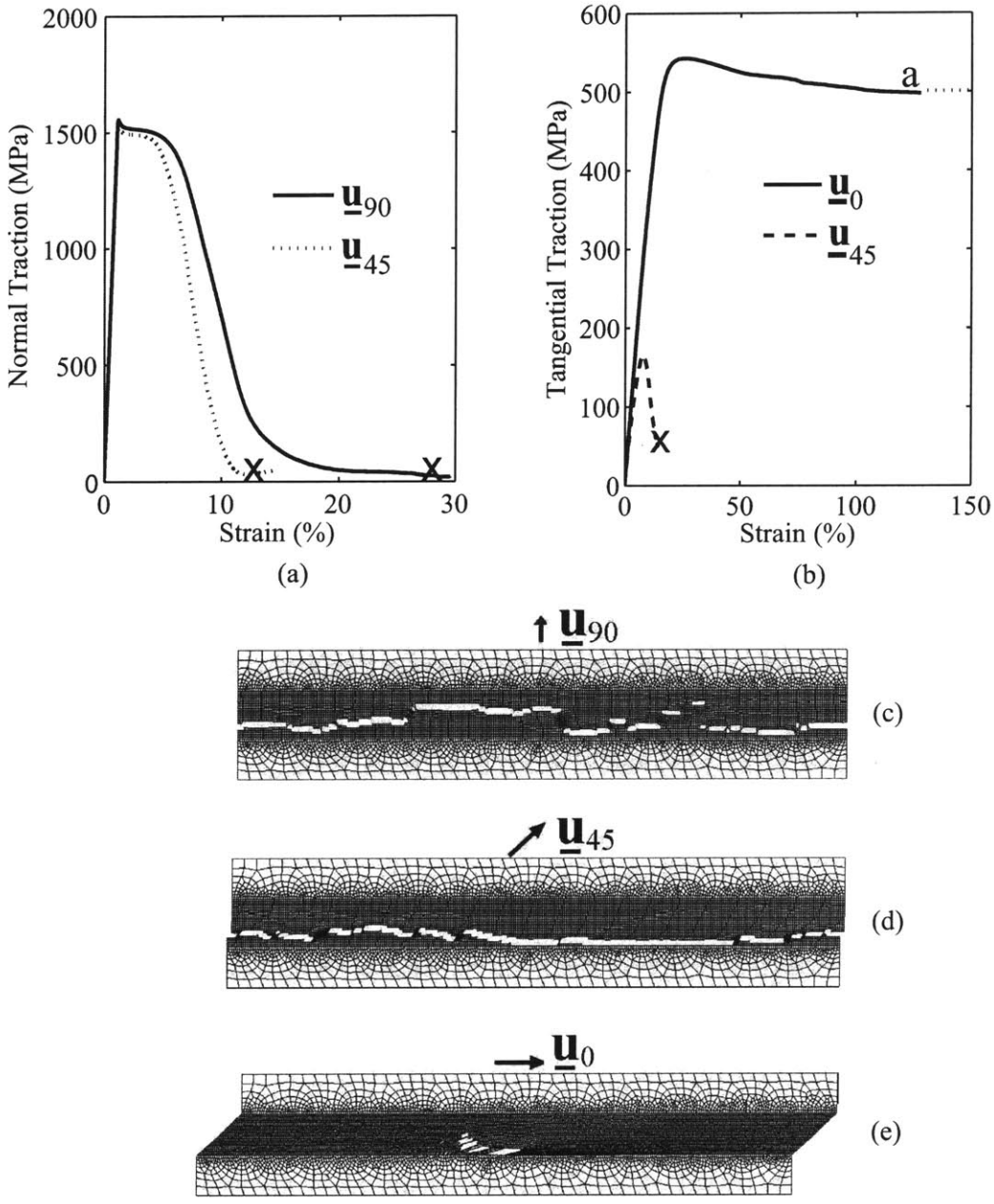

Figure 3-4: (a) Normal traction versus nominal normal strain of the amorphous layer for $\underline{\mathbf{u}}_{90}$ and $\underline{\mathbf{u}}_{45}$. (b) Tangential traction versus nominal shear strain of the amorphous layer for $\underline{\mathbf{u}}_0$ and $\underline{\mathbf{u}}_{45}$. (c) Failure pattern of the amorphous grain-boundary region subject to normal displacement $\underline{\mathbf{u}}_{90}$. (d) Failure pattern for $\underline{\mathbf{u}}_{45}$. (e) Failure pattern for $\underline{\mathbf{u}}_0$.

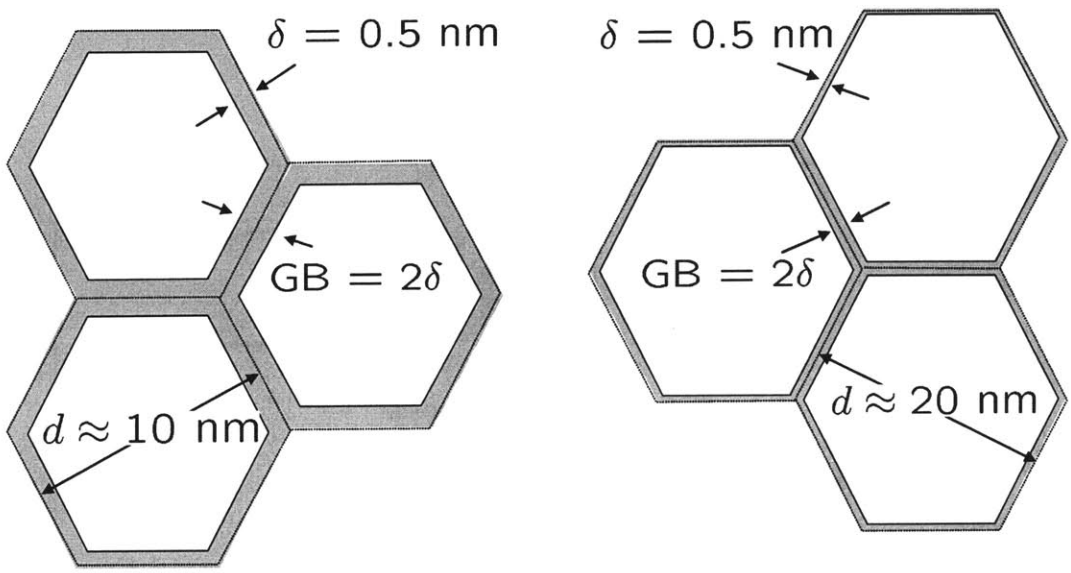

(a) (b)

Figure 3-5: Schematic of (a) grain size of $d = 10\,\text{nm}$ with grain-boundary regions of thickness $2\delta = 1\,\text{nm}$; and (b) grain size of $d = 20\,\text{nm}$ with grain-boundary region of thickness $2\delta = 1\,\text{nm}$.

3.5 Finite element representation of microstructures with different grain sizes

As shown schematically in Fig. 3-5 a and b, for a fixed grain-boundary thickness of $2\delta = 1\,\text{nm}$, the volume fraction of grain-boundary regions decreases as the grain size d increases from 10 nm to 20 nm. Hence, by assuming that the physical thickness of a grain boundary is fixed at $\approx 1\,\text{nm}$, we can numerically represent microstructures with different average grain size, by simply adjusting the volume fraction of "grain-boundary" elements to "grain-interior" elements in a finite-element mesh.

Two-dimensional Voronoi-tesselated grains have been generated and meshed to represent the plane strain deformation of nanocrystalline metals. Those Voronoi grains, generated by a method suggested by Gross and Li (2002), satisfies a log normal distribution . Figs. 3-6 a – 6 d show four microstructures of average grain size of $\approx$ 10 nm, 20 nm, 34 nm, and 50 nm, respectively. Diameter d of individual grain size is estimated using $Area = \frac{\pi d^2}{4}$. The lighter-colored regions in these figures are the grain-boundary regions, and the darker regions are the grain interiors. In Fig. 3-

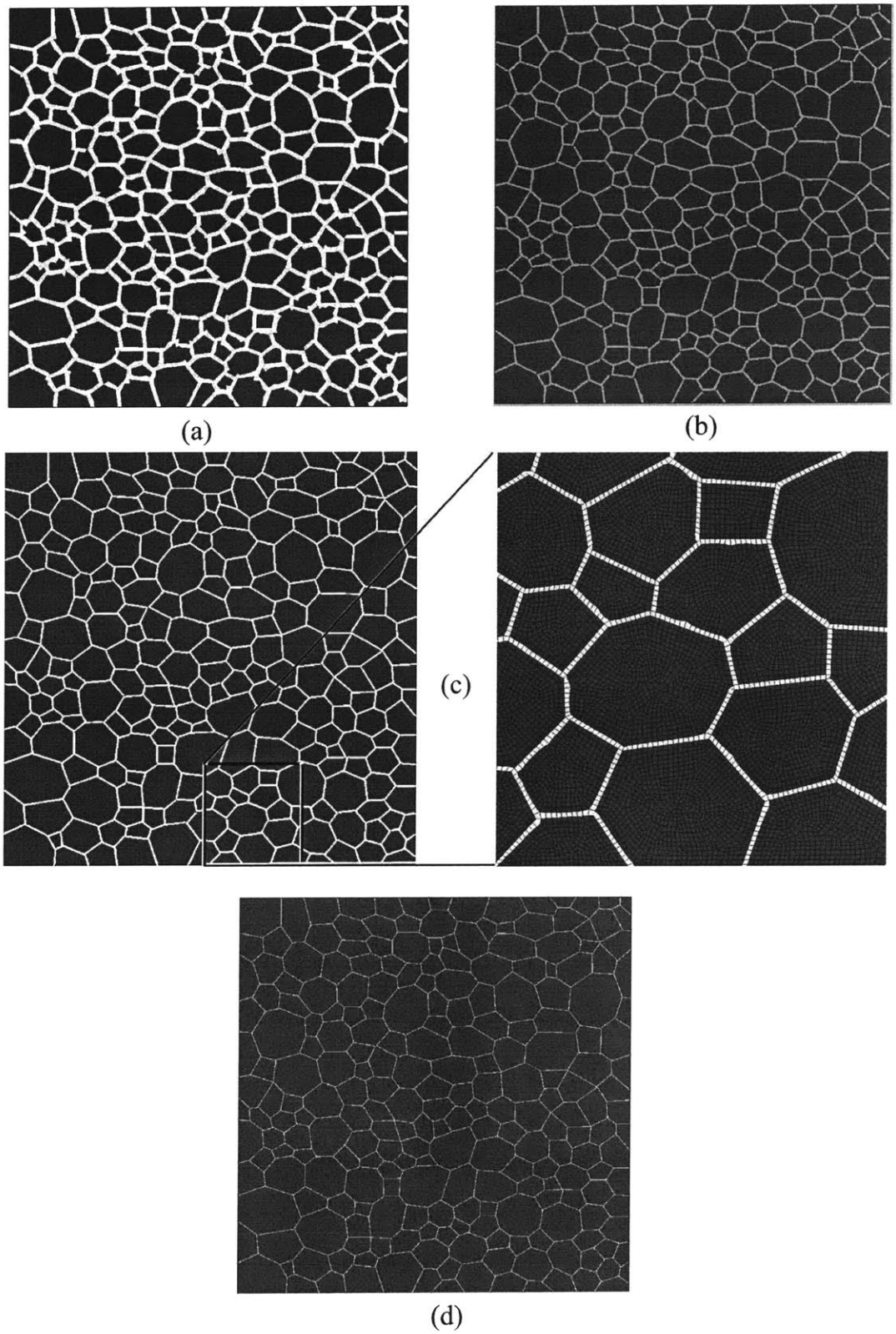

Figure 3-6: Microstructures with an average grain size of (a) 10 nm; (b) 20 nm; (c) 34 nm; the boxed region is magnified to show finite-element meshes in grain interiors and grain boundaries; (d) 50 nm.

6 c the boxed region is magnified to show the finite elements in the grain-boundary regions and the grain interiors. Note that unlike Fig. 3-2, here for computational efficiency *all grain-boundary regions are meshed with only one element through their thicknesses.* Thus, in order to obtain a high quality mesh for grain-boundary regions which are one element thick, the larger the grain size, the smaller the element size in the finite element mesh that is required; this results in a large number of elements in the microstructure with larger grain sizes. For example, in the microstructure shown in Fig. 3-6 d, more than 300,000 elements were used to represent the microstructure for a grain size of $d \approx 50\,\text{nm}$.

The constitutive response of the grain-boundary elements is represented by the model detailed in § 3.2 for amorphous metals, while the constitutive response of the grain-interior elements is represented by the single-crystal plasticity model detailed in § 3.3.

3.6 Application of the model to nanocrystalline nickel

The tensile stress-strain response of nanocrystalline nickel (nc-Ni) has been experimentally investigated by numerous (different) groups (e.g. Gray et al., 1997; Wang et al., 1997; Yin and Whang, 2001; Xiao et al., 2001; Torre et al., 2002; Schwaiger et al., 2003; Zhu et al., 2005). For example, Fig. 3-7 from Schwaiger et al. (2003) shows room temperature tensile stress-strain curves for nc-Ni with a grain size of $\approx 35\,\text{nm}$ at three different strain-rates. The material exhibits a high strength of approximately 1500 MPa, but a low ductility of less than 5%. As noted earlier, it also exhibits a positive strain-rate sensitive response, with the rate sensitivity significantly higher than that observed in microcrystalline nickel at the same temperature, cf. Fig. 3-1.

In order to use our constitutive models for grain-interior crystal plasticity and grain-boundary amorphous plasticity to reproduce the macroscopic stress-strain curves for nc-Ni in Fig. 3-7, we need to estimate reasonable values for the material parameters

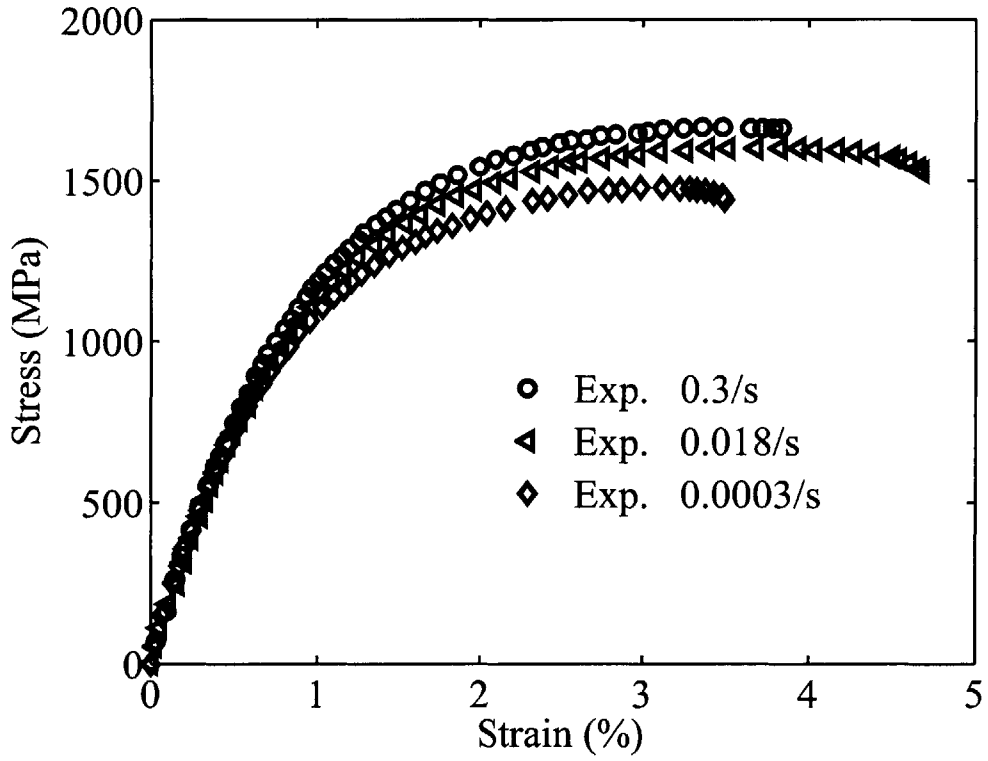

Figure 3-7: Tensile stress-strain curves for nanocrystalline nickel with an average grain size of $\approx 35\,\text{nm}$ at different quasi-static strain rates, Schwaiger et al. (2003).

appearing in these models. We discuss our estimation procedure in the subsections below. Briefly, reasonable values for the grain-interior material properties are readily arrived at from physical considerations, but the properties of the grain-boundaries need to be estimated by *curve-fitting* the macroscopic stress-strain curves. Our strategy is to estimate the material parameters by fitting the model to the stress-strain curves of Schwaiger et al. (2003) shown in Fig. 3-7, and then to check whether these values are reasonable or otherwise, by checking whether the model with the material parameters so estimated, is able to reproduce a different set of data for a different grain size and different strain rates reported by Zhu et al. (2005).

3.6.1 Material properties for grain interiors

The anisotropic elasticity tensor $\mathbb{C}$ for cubic materials is specified in terms of three standard stiffness parameters, C_{11}, C_{12} and C_{44}. The values of the elastic parameters for nickel are taken as (Simmons and Wang, 1971):

$$C_{11} = 247\,\text{GPa}, \quad C_{12} = 147\,\text{GPa}, \quad C_{44} = 125\,\text{GPa}. \tag{3.40}$$

Next, with

$$G = \sqrt{(C_{11} - C_{12})C_{44}/2} \approx 79\,\text{GPa}, \tag{3.41}$$

a nominal shear modulus, $b = 0.249\,\text{nm}$ the magnitude of the Burgers' vector, and $\Gamma \approx Gb/100$ the surface energy, the critical grain size below which partial dislocations emitted from grain boundaries are the dominant carriers of plastic deformation of the grain interiors is given by

$$d_c \approx \frac{2}{3}\left(\frac{Gb^2}{\Gamma}\right) \approx 16.6\,\text{nm}. \tag{3.42}$$

The slip systems for $d > d_c$, and the faulting systems for $d \leq d_c$, are listed in Table 3.1, and the slip and faulting system resistances are taken as

$$s^{\alpha} = \begin{cases} \dfrac{Gb}{d} & \text{for } d > d_c, \\ \\ \dfrac{Gb}{3d} & \text{for } d \leq d_c\,, \end{cases} \tag{3.43}$$

respectively. If for the very smallest grain sizes the resistance calculated using (3.43) exceeds the the ideal shear strength

$$s^{\alpha}_{\max} \approx \frac{G}{30} \approx 2.6\,\text{GPa},$$

then the resistance is capped at this maximum possible value. Fig. 3-8 a shows a contour plot of the grain-interior strength for a microstructure with an average grain-size of 34 nm. Nanocrystalline nickel produced by electro-deposition typically possesses a strong crystallographic texture. Fig. 3-8 b shows the (111) pole figure for such a material; the pole figure projection direction is normal to the plane of the sheet nc-Ni specimen. In our numerical simulations the lattices of the individual grains were assigned a set of orientations that approximate this initial texture, Fig. 3-8 c. Fig. 3-6 shows self-similar microstructures with different average grain sizes. For each of these different average grain-sized microstructures, the initial lattice orientation of each grain is taken to be the same for the four different microstructures; hence the resulting overall crystallographic texture for all the different microstructures of Fig. 3-6 is as shown in Fig. 3-8 c.

The reference strain rate ν_0 and strain-rate sensitivity parameter m in (3.36) and (3.39) are taken as

$$\nu_0 = 10^{-5}/s, \qquad m = 0.005\,;$$

the low value of the strain rate-sensitive parameter is meant to represent an approximately rate-independent response for the plasticity of the grain interiors, cf. Fig. 3-1.

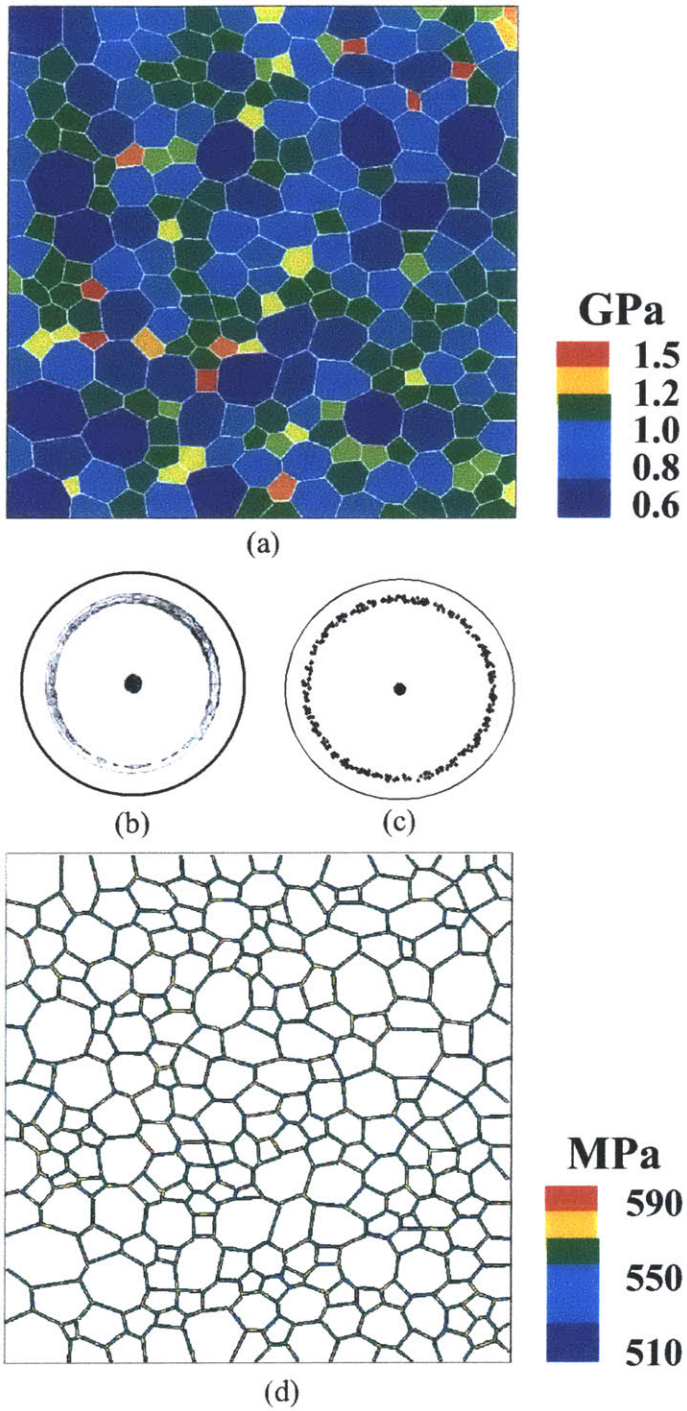

Figure 3-8: (a) Grain-interior strength for the microstructure with an average grain size of $\approx 34\,\text{nm}$. (b) Experimental (111) pole figure of as-received electrodeposited nc-nickel sheet from Xiao et al. (2001); pole figure projection direction is normal to the plane of the sheet specimen. (c) (111) Pole figures corresponding to the grain orientations used in the polycrystal simulations. (d) Heterogeneity of grain-boundary cohesion. Cohesion in grain-boundary elements is randomly distributed in the range 510 to 590 MPa.

The threshold resistance s_{th} for partial dislocation emission in (3.39) is taken as

$$s_{th} = \frac{\Gamma}{b} \approx 790\,\text{GPa}\,.$$

3.6.2 Material properties for grain boundaries

Having arrived at physically plausible values for the grain-interior material properties, we next estimate the properties of the grain boundaries by *curve-fitting* the macroscopic stress-strain curves of Schwaiger et al. (2003) shown in Fig. 3-7. Since the average grain size in the material tested by Schwaiger et al. (2003) is $\approx$ 30 to 40 nm. We have used the microstructure with average grain size of 34nm, Fig. 3-6 c, to estimate the grain-boundary properties.

The elastic properties of grain-boundary elements are assumed to be the same as those for polycrystalline nickel with

$$G = 79\,\text{GPa}, \text{ and } \quad K = 182\,\text{GPa}.$$

To allow for varying grain-boundary strengths, the value of c for each grain-boundary element was randomly assigned a value from a list which had values of c uniformly distributed between 510 and 590 MPa, so that the average value of the cohesion of the grain boundaries is

$$c = 550\ \text{MPa}.$$

Fig.3-8 d shows a contour plot of the values of the initial cohesion in the grain boundaries. We use a small value of frictional coefficient $\mu = 0.04$, which is close to the internal frictional coefficient of metallic glass Anand and Su (2005).[9] The reference strain rate ν_0 and strain-rate sensitivity parameter m in (3.21) and (3.23) are taken as[10]

$$\nu_0 = 10^{-5}/s, \qquad m = 0.1\,,$$

[9]The precise value of μ is not consequential here.

[10]The value of strain-rate sensitivity of $m = 0.1$ appears high, but this is the value that gives us the fit to the macroscopic stress-strain curves shown in Fig. 3-9 a.

while the parameters governing the cavitation resistance in $(3.22)_3$ are taken as

$$\sigma_{cr} = c_1 - c_2\,\bar{\sigma}_h, \text{ with } c_1 = 10\,\text{GPa},\ c_2 = 8.5\,,$$

and the parameters ϵ^p_{cr} and ϵ^p_f appearing in the definition of cavitation damage (3.26), are taken as

$$\epsilon^p_{cr} = 0.1, \qquad \text{and} \qquad \epsilon^p_f = 0.36,$$

respectively.

Using our previously-listed assumptions concerning the grain-interior properties and the inelastic parameters for the grain boundaries listed above, we obtained the reasonable curve-fit shown in Fig. 3-9 a, to the experimentally-measured stress-strain curves Schwaiger et al. (2003). Fig. 3-9 b shows a contour plot of the equivalent plastic strain after 5% strain at a strain rate of $\dot{\epsilon} = 3 \times 10^{-4}/\text{s}$. At this low strain rate most of the inelastic deformation is restricted to the grain-boundary elements, and due to the constrained deformation in these boundaries, cavitation occurs. The voids observed in Fig. 3-9 b result from grain-boundary elements which have failed due to cavitation. In contrast, Fig. 3-9 c shows a contour plot of the equivalent plastic strain after 5% strain at a strain rate of $\dot{\epsilon} = 3 \times 10^{-1}/\text{s}$. At this higher strain rate the high rate-sensitivity of the grain-boundary elements results in stronger grain boundaries, and this induces dramatically increased grain-interior plasticity, as evidenced by the plastic strain contours in this figure. Also, comparing Fig. 3-9 c to Fig. 3-9 b, we note that the amount of cavitation damage at the grain boundaries is substantially reduced at the higher strain rate.

Next, in order to check whether the material parameters estimated for the grain interiors and grain boundaries are in a reasonable range, we verified the predictive capability of the model by comparing the predicted stress-strain curves at different strain-rates for nc-Ni with an average grain size of 20 nm using the mesh shown in Fig. 3-6 b against corresponding experimental data from Zhu et al. (2005). The comparison, Fig. 3-10, shows that while stress levels are reasonably well-predicted, the ductility is not well-predicted by our relatively crude grain-boundary cavitation

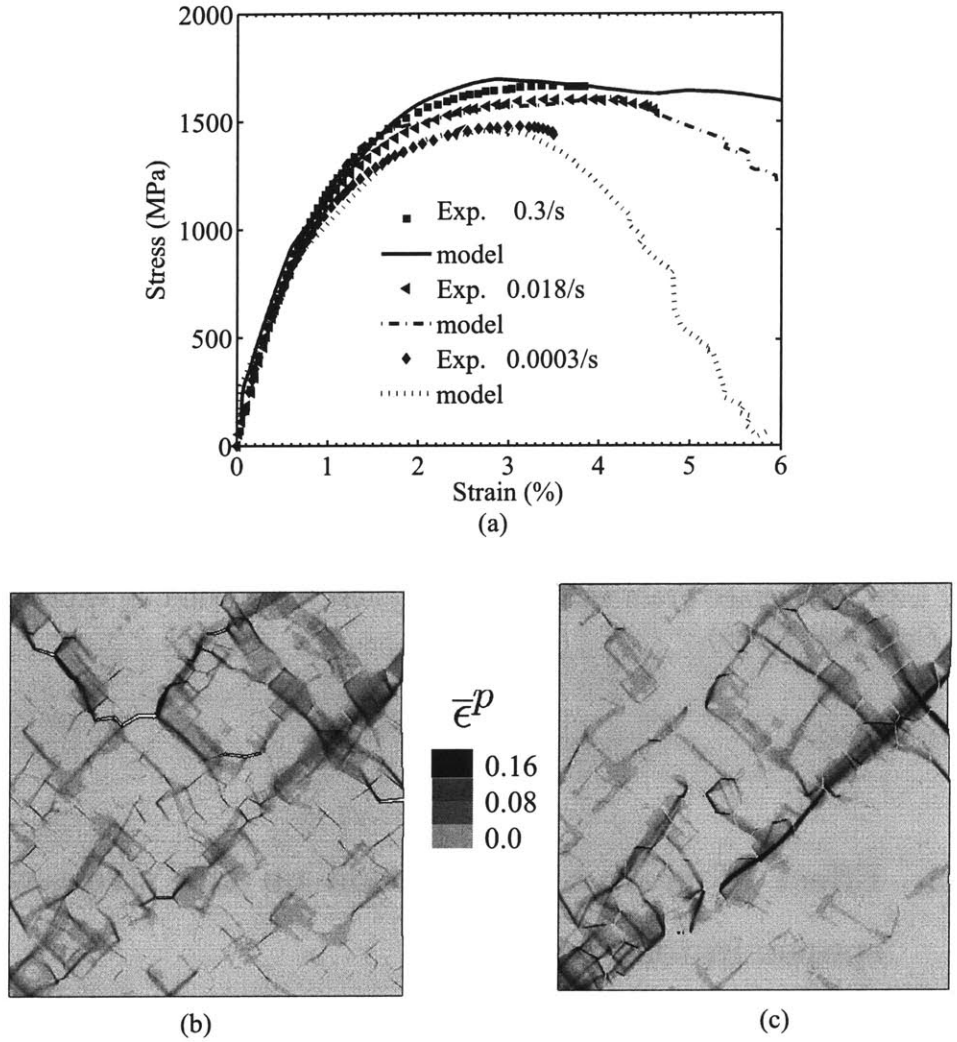

Figure 3-9: (a) Comparison of numerically-calculated and experimentally-measured (Schwaiger et al., 2003) stress-strain curves. (b) Equivalent plastic strain contour after 4% strain at a strain rate of $\dot{\epsilon} = 3 \times 10^{-4}/\text{s}$; voids in the figure result from grain-boundary elements which have failed due to cavitation. At this higher strain rate, the high rate-sensitivity of the grain-boundary elements results in stronger grain boundaries, and this induces dramatically-increased grain-interior plasticity.

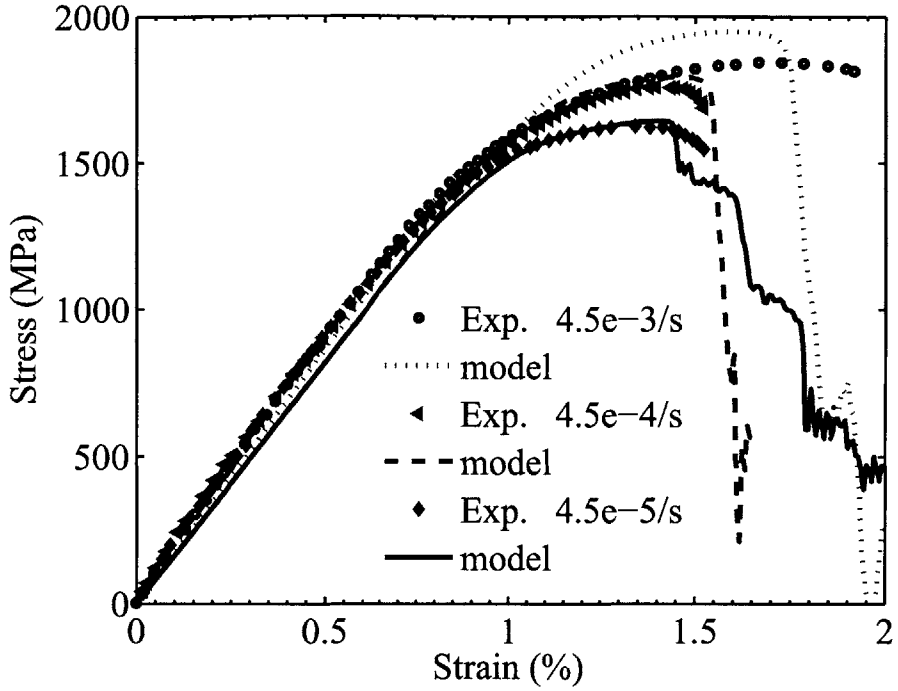

Figure 3-10: Comparison of predicted stress-strain curves at different strain-rates for nc-Ni with an average grain size of 20nm against corresponding experimental data from Zhu et al. (2005).

damage model.

3.6.3 Effect of grain size variation on the stress-strain response in tension

With the material parameters for the grain interior and grain boundaries fixed at values determined in the previous subsections, Fig. 3-11 a shows tensile stress-strain curves for different grain-sized microstructures of Fig. 3-6, at a strain rate of 3×10^{-4}/s. As is clear, the peak strength does not increase monotonically as the grain size is reduced. Although we have results for only four different grain sizes, a clear peak is observed for the microstructure with a grain size of 20 nm; the peak strengths for the 10 nm and 34 nm microstructures are clearly lower than that for the 20 nm microstructure. Figs. 3-11 b-d show contour plots of the equivalent plastic strain at the peak strength levels for the different grain sizes. As is clear from these figures, at the

smaller grain sizes of 10, 20 and 34 nm most of the inelastic deformation occurs at the grain boundaries, while the larger 50 nm grain-sized microstructure shows substantial grain-interior plasticity.

3.6.4 Effect of grain size variation on the stress-strain response in compression

In this section we numerically investigate the response of nc-Ni in compression.[11] Fig. 3-12 a shows tensile stress-strain curves for different grain-sized microstructures of Fig.3-6, at a strain rate of $3 \times 10^{-4}/\text{s}$. Figs. 3-12 b,c show contour plots of the equivalent plastic strain at a macroscopic strain of 4% for microstructures of 20 nm and 50 nm average grain-sizes respectively. For clarity, in each of Figs. 3-12 b and c, a small region of the deformed microstructure is magnified to show the severe deformation of grain-boundary regions marked by arrows. The smaller grain-sized microstructure of Fig. 3-12 b shows substantial grain-boundary shearing and cavitation, with some grain-interior plasticity in the grains associated with boundaries with intense shearing activity. As the grain size increases to 50 nm, Fig. 3-12 c shows a transition to increased grain interior plasticity and inhomogeneous deformation patterns resembling "shear-bands" which traverse several grains.

A plot of ultimate strength in tension and compression versus grain size is shown in Fig. 3-13. There is a clear strength-differential effect, with compressive strengths being higher than tensile strengths for the 10 nm, 20 nm, and 34 nm grain-sized microstructures. Our calculations show that this strength-differential effect is *not due* to the small friction coefficient of $\mu = 0.04$ for the grain-boundary model, but arises because of the delayed damage by cavitation of grain boundaries in compression, relative to the situation for tension.

[11] We were unable to find experimental data for controlled compression tests on nc-Ni in the literature.

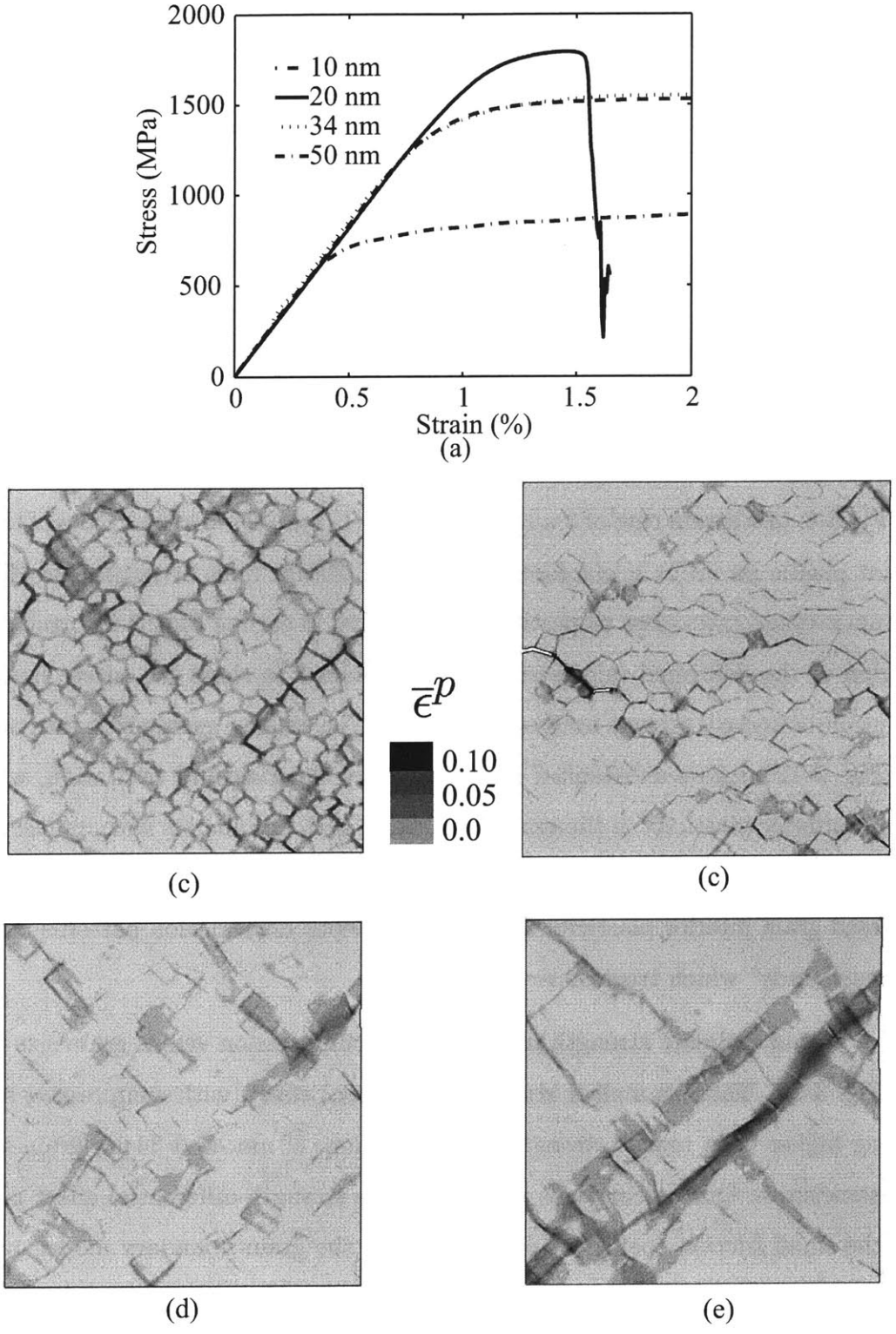

Figure 3-11: (a) Tensile stress-strain curves for different grain sizes at a strain rate of 3×10^{-4}/s. Corresponding contours of plastic strain at a macroscopic strain of 1.5%: (b) 10 nm. (c) 20 nm. (d) 34 nm, and (e) 50 nm.

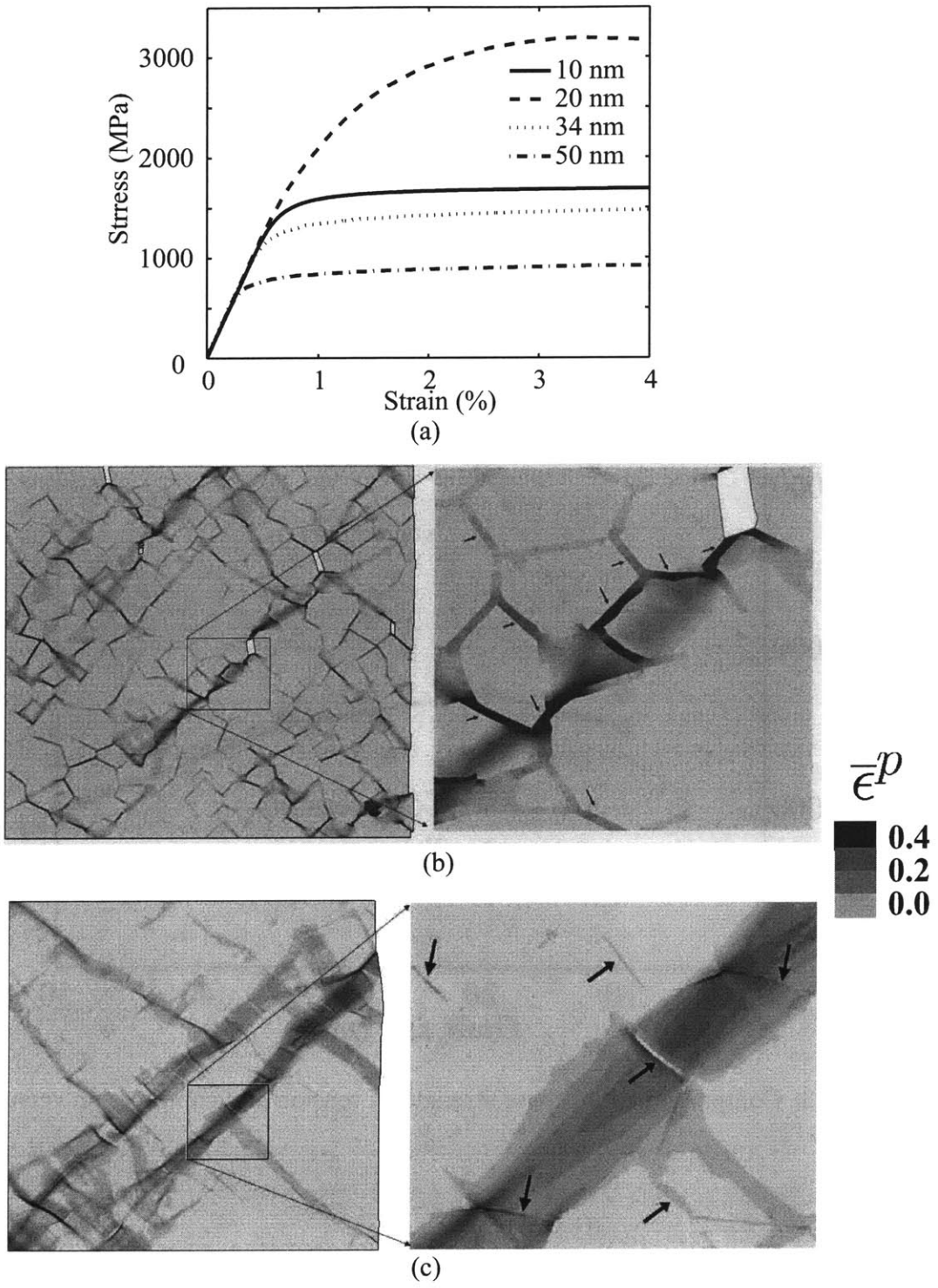

Figure 3-12: (a) Compression stress-strain curves for different grain sizes at a strain rate of 3×10^{-4}/s. Corresponding contours of plastic strain at a macroscopic strain of 4%: (b) 20 nm, and (c) 50 nm. In (b) and (c) a small region of the microstructure is magnified to show the severe deformation of grain-boundary regions marked by arrows.

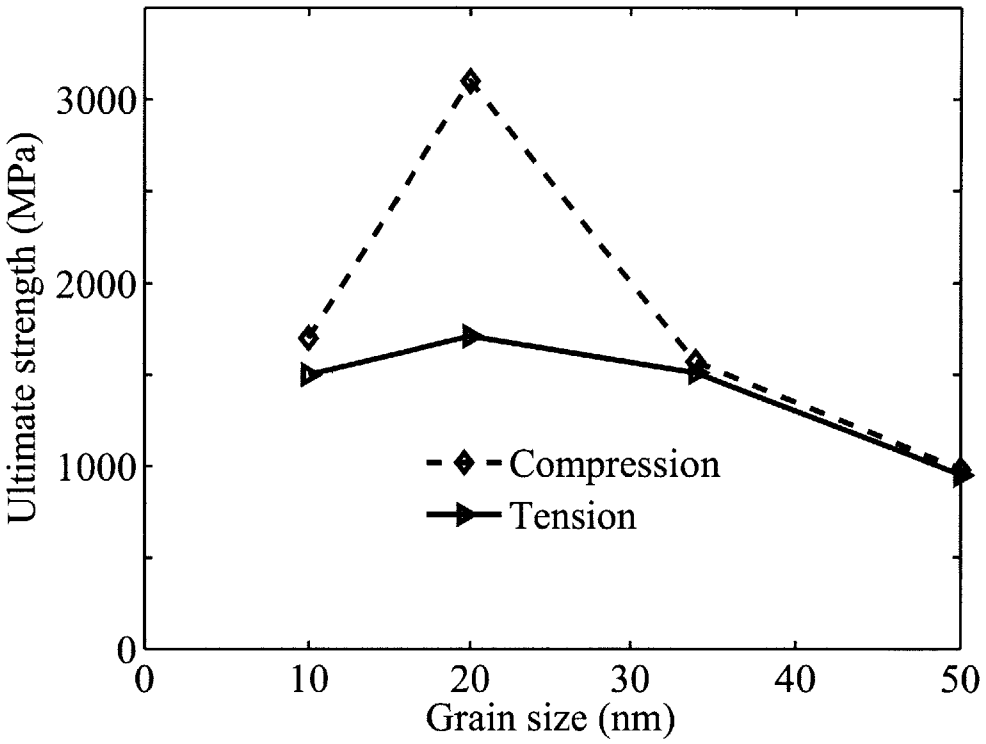

Figure 3-13: Comparison of ultimate strength in tension and compression versus grain size.

3.7 Concluding remarks

We have developed a finite-element-based mesoscale "core-and-mantle"-type two-dimensional plane-strain model to numerically study the deformation and failure behavior of nanocrystalline fcc metals. A rate-dependent amorphous plasticity model which accounts for cavitation and related failure phenomena is used to model the grain boundary, while a crystal-plasticity model which accounts for the transition from partial dislocation to complete dislocation mediated plasticity is used for the limited plasticity of the grain interiors. Numerical simulations using material parameters estimated to represent the macroscopic rate-dependent stress-strain response of nc-Ni show that

- There is a deformation mechanism transition from grain-interior dominant shearing to grain-boundary dominant shearing and cavitation as the average grain-size decreases from 50 nm to 10 nm.

- A change from low strain rate to high strain rate deformation also induces a transition in mechanism from deformation dominated by grain-boundary shearing and cavitation to grain-interior dominated plastic deformation.

- The low ductility in nc-Ni is the result of intergranular failure due to grain-boundary shearing and resulting cavitation at triple-junctions and other high stress points in the microstructure.

- The strength of nc-Ni is expected to be higher in compression than in tension, primarily due to the easier operation of cavitation failure of the grain boundaries in tension relative to that in compression.

Chapter 4

A constitutive model for powder-processed nanostructured materials

4.1 Introduction

Nanostructured metals with grain sizes typically less than 100 nm have been shown to exhibit high strength and hardness, but they also exhibit limited ductility due to difficulties in synthesis, specially for materials produced from powders by various consolidation techniques. Significant developments in the processing of such materials have occurred in recent years, and materials are beginning to be produced which exhibit not only high strength, but also a reasonable amount of ductility. Such materials, when produced in sufficient quantities, may therefore actually become viable for use in structural applications.

Of particular note is the recent work reported by Youssef et al. (2004) and Cheng et al. (2005) for the processing of copper, in which the authors report achieving nominally-dense samples with a narrow grain-size distribution in the nanocrystalline range by a special *in-situ* processing technique that involves a two-step high-energy

[1]The work in this chapter is submitted to Acta Materialia (2006) for publication.

ball milling process, first at liquid nitrogen temperature, and subsequently at room temperature.[1] Fig. 3-1a from Cheng et al. (2005) shows a typical TEM bright-field image of their nc-Cu, and Fig. 3-1b shows engineering stress-strain curves from tension tests on one of their materials at strain rates of 10^{-2}, 10^{-3}, and 10^{-4} s^{-1}. Their nc-Cu shows strength levels greater than $\approx$ 650 MPa, and a tensile elongation to failure of at least 6%.

Further, the nc-Cu shows a strain-rate sensitivity $m(\equiv \partial \ln \sigma_f / \partial \ln \dot{\epsilon}) \approx 0.026$, which represents a four-fold increase over the strain rate sensitivity of conventional coarse-grained Cu ($m \approx 0.006$).

Similarly impressive properties have also been recently been reported for powder-consolidated nanocrystalline Mg-based materials by Lu et al. (2004a).[2] Samples of their nc-Mg-5%Al-1%Nd alloy were kindly provided to us by Prof. Li Lu of the National University of Singapore, and we conducted TEM microscopy, and performed some standard tension and compression experiments on their material. Fig. 3-2a shows a typical TEM bright-field image of their nc-Mg. Fig. 3-2b shows true stress-strain curves in tension and compression at a strain rate of $10^{-4}\,s^{-1}$. The strength level is approximately 400 MPa. Note that there is a small tension-compression asymmetry, with the compressive curve being slightly higher than the tensile curve; also, while the tensile ductility is at a respectable level of approximately 9%, the ductility in compression is substantially higher, approaching levels greater than 35% at low strain rates. Further, the material shows *strain-softening* in both tension and compression. Fig. 3-2 c shows true stress-strain curves from compression tests on the same material at strain rates of 10^{-2}, 10^{-3}, and 10^{-4} s^{-1}. Note the pronounced strain-rate sensitivity exhibited by the material; the nc-Mg has a strain-rate sensitivity of $m \approx 0.07$, which represents a seven-fold increase over that of a conventional coarse-grained magnesium alloy AZ31B ($m \approx 0.01$). The ductility in compression is seen to *decrease* as the strain

[1] For additional processing details see Cheng et al. (2005).

[2] These authors have developed nanostructured Mg alloys of nominal composition Mg-5%Al-x%Nd, with x=0.5%, 1%, and 5% by weight. A typical processing schedule used by these authors is to first mechanically-alloy the Mg, Al and Nd powders. The mechanically-alloyed powders are then cold-compacted into cylinders of 35mm diameter, and sintered at 400 C or 500 C in a vacuum furnace for 2 hours. The sintered cylinders are then extruded at 400 C with an extrusion ratio of 25:1. For additional processing details see Lu et al. (2004a).

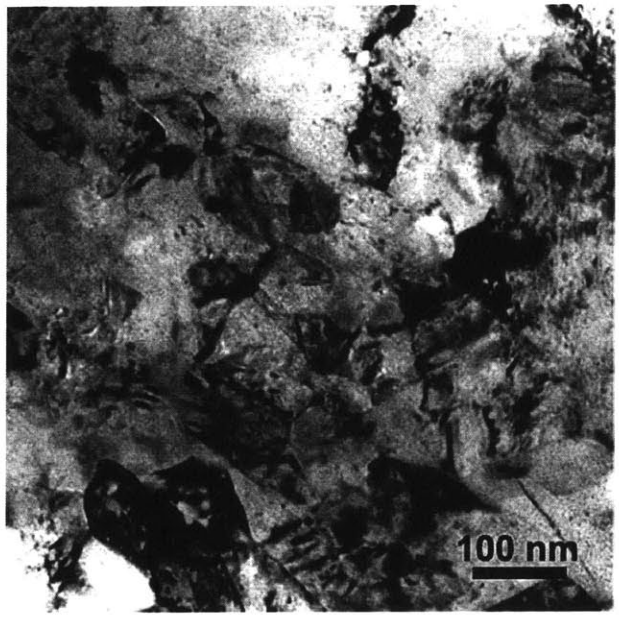

(a)

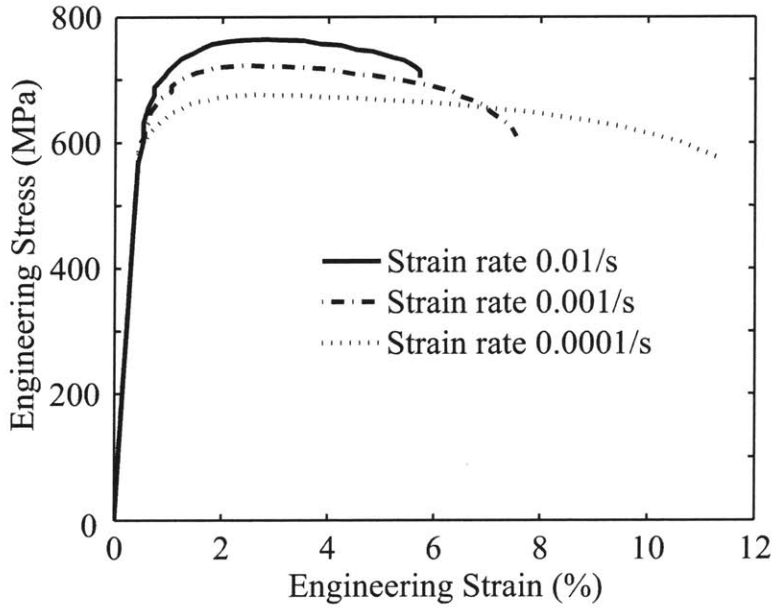

(b)

Figure 4-1: From Cheng et al. [2]: (a) TEM bright-field image of nc-Cu obtained after a two-stage high-energy ball milling process. (b) Tensile engineering stress-strain curves at strain rates of $10^{-2}\,\mathrm{s}^{-1}$, $10^{-3}\,s^{-1}$, and $10^{-4}\,\mathrm{s}^{-1}$.

Material	ρ Mg/m^3	E GPa	σ_y MPa	E/ρ	σ_y/ρ	grain size (nm)
nc-Mg (Lu et al., 2004a)	1.8	$\sim$ 43	$\sim$400	$\sim$ 25	$\sim$222	$\sim$ 90
nc-Cu (Cheng et al., 2005)	8.9	$\sim$ 107	$\sim$700	$\sim$14	$\sim$ 80	$\sim$45
nc-Ni (Torre et al., 2002)	8.7	$\sim$ 192	$\sim$1150	$\sim$ 28	$\sim$ 130	$\sim$28

Table 4.1: Specific stiffness and strength of some nanocrystalline metals.

rate increases, but it is still greater than 10% at a strain rate of $10^{-2}\,s^{-1}$. Finally note that the high values of specific-stiffness (E/ρ) and specific-strength (σ_y/ρ) of nc-Mg, relative to that of powder-consolidated nanocrystalline Cu and electro-deposited Ni, cf. Table 1, makes the Mg-based nanocrystalline material potentially very attractive for light-weight structural applications.

Concerning the strain-softening of the nc-Mg alloy observed in Fig. 3-2b, pole figures from our crystallographic texture evolution experiments on this material, Fig. 3-3a and b, show that there is very little texture evolution after compressive strain levels of $\sim$ 15%. However, as shown in a representative TEM micrograph of the deformed specimen in Fig. 3-3c, there is evidence of distributed internal damage due to grain-boundary decohesion in the material. Based on these experimental results we conclude that the strain-softening is *not* due to texture evolution, but due to distributed internal grain-boundary damage, which is to be expected in powder-consolidated materials.

With the emerging capabilities to produce nanocrystalline materials which exhibit not only high strength but also a reasonable amount of ductility, it is of interest to formulate continuum-level constitutive models, which when implemented in finite-element solution procedures may be used in the design of structural components made from such materials. It is the purpose of this chapter to report on such a model. From a macroscopic point-of-view, powder-consolidated metals (nanocrystalline or otherwise) are similar to cohesive granular materials. Guided by this similarity, the constitutive model that we have formulated is a large-deformation, isotropic, rate-dependent elasto-plasticity model in which, the plastic flow is taken to be pressure-

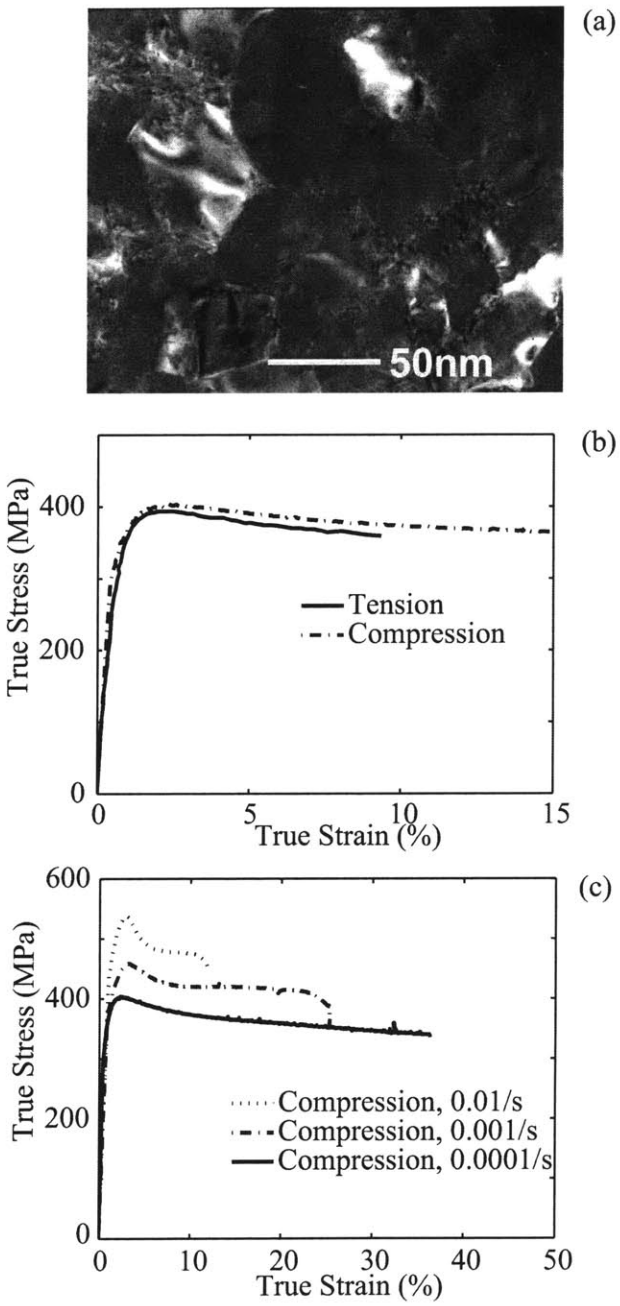

Figure 4-2: (a) TEM bright-field image of nc-Mg; material supplied by Lu et al. [3]. (b) Stress-strain curves for nc-Mg in tension and compression at a strain rate of $10^{-4}\,\mathrm{s}^{-1}$. (c) Stress-strain curves in compression at strain rates of $10^{-2}\,\mathrm{s}^{-1}$, $10^{-3}\,s^{-1}$, and $10^{-4}\,\mathrm{s}^{-1}$.

dependent, plastically dilatant, and non-normal.

The plan of this chapter is as follows. We develop our constitutive model in § 2. We have implemented the constitutive model in the commercial finite-element program ABAQUS/Explicit (Abaqus, 2005) by writing a user-material subroutine. In § 3 we use published experimental data from macroscopic stress-strain tests to estimate the material parameters appearing in the model for nc-Cu (Cheng et al., 2005). Using the material parameters so-determined, we carry out a three-dimensional finite-element simulation of a sheet tension specimen of this material, and numerically study the evolution of deformation patterns and localized necking in this material. In this section we also compare the results from our numerical simulations of localized-necking against those observed experimentally by Cheng et al. (2005) (their Fig. 8), and show that our numerical simulations satisfactorily reproduce their experimental results. In § 4 we use our own experimental stress-strain data on nc-Mg to estimate the material parameters appearing in the model for this material. Then, in order to check the predictive capabilities of our constitutive model and computational procedures, we carry out axisymmetric finite-element simulations of conical micro-indentation experiments at three different loading rates, and compare the numerically predicted load (P) versus indentation depth (h) curves against corresponding experimentally-measured P-h curves. The numerically-predicted curves are shown to closely match those observed in the experiments. We close in § 5 with a few final remarks.

4.2 Constitutive model

Our continuum-mechanical theory is based on the following major kinematical and constitutive ideas:[3]

[3] *Notation*: We use standard notation of modern continuum mechanics. The symbols ∇ and Div denote the gradient and divergence with respect to the material point $\mathbf{X}$ in the *reference configuration*; grad and div denote these operators with respect to the point $\mathbf{x} = \boldsymbol{\chi}(\mathbf{X}, t)$ in the deformed configuration; a superposed dot denotes the material time-derivative. Throughout, we write $\mathbf{F}^{e-1} = (\mathbf{F}^e)^{-1}$, $\mathbf{F}^{p-\top} = (\mathbf{F}^p)^{-\top}$, etc. We write $\operatorname{sym}\mathbf{A}$, $\operatorname{skw}\mathbf{A}$, $\mathbf{A}_0$, and $\operatorname{sym}_0\mathbf{A}$ respectively, for the symmetric, skew, deviatoric, and symmetric-deviatoric parts of a tensor $\mathbf{A}$. Also, the inner product of tensors $\mathbf{A}$ and $\mathbf{B}$ is denoted by $\mathbf{A}:\mathbf{B}$, and the magnitude of $\mathbf{A}$ by $|\mathbf{A}| = \sqrt{\mathbf{A}:\mathbf{A}}$.

(i) The decomposition

$$\mathbf{F} = \mathbf{F}^e\mathbf{F}^p \tag{4.1}$$

of the deformation gradient $\mathbf{F} = \nabla\boldsymbol{\chi}$ into *elastic* and *plastic* parts $\mathbf{F}^e$ and $\mathbf{F}^p$, respectively (Kröner, 1960; Lee, 1969).

(ii) An evolution equation for $\mathbf{F}^p$, the flow rule,[4]

$$\dot{\mathbf{F}}^p = \mathbf{D}^p\mathbf{F}^p, \qquad \mathbf{D}^p = \mathbf{D}^{p\top}, \tag{4.2}$$

with the plastic stretching $\mathbf{D}^p$ given by

$$\left.\begin{aligned} \mathbf{D}^p &= \mathbf{D}^p_0 + \frac{1}{3}(\mathrm{tr}\mathbf{D}^p)\mathbf{1}, \quad \text{with} \\ \mathbf{D}^p_0 &= \nu^p\,\mathbf{N}^p, \quad \text{and} \\ \mathrm{tr}\mathbf{D}^p &= \beta\nu^p, \end{aligned}\right\} \tag{4.3}$$

where

$$d^p = \sqrt{2}|\mathbf{D}^p_0| \tag{4.4}$$

is an *equivalent plastic shear strain rate*,

$$\mathbf{N}^p = \frac{\boldsymbol{\Sigma}_0}{2\bar{\tau}} \tag{4.5}$$

is a "direction" of deviatoric plastic flow given in terms of the deviator $\boldsymbol{\Sigma}_0$ of a stress $\boldsymbol{\Sigma}$, with

$$\bar{\tau} = \frac{1}{\sqrt{2}}|\boldsymbol{\Sigma}_0| \tag{4.6}$$

an *equivalent shear stress*. The equivalent plastic shear strain rate d^p is specified by a *power-law* constitutive function

$$d^p = d_0\left\{\frac{\bar{\tau}}{c+\mu\bar{p}}\right\}^{1/m} \geq 0, \tag{4.7}$$

[4]Our flow rule is a generalization of the rate-independent flow rules of Rudnicki and Rice (1975) and Anand (1980).

where

$$\bar{p} = -\frac{1}{3}\mathrm{tr}\,\boldsymbol{\Sigma}, \tag{4.8}$$

is mean-normal pressure; $c > 0$ and $\mu \geq 0$ are internal variables called the *cohesion* and *internal friction*, respectively; also d_0 is a *reference plastic shear strain rate*, and $m > 0$ is a *strain-rate-sensitivity parameter*. The term $\mu\bar{p}$ accounts for pressure-sensitivity of plastic flow, and the quantity β in eq. $(4.3)_3$ is a *shear-induced plastic dilatancy function*.[5]

(iii) A key feature controlling the plastic deformation of compacted powder materials is the change in the density of these materials due to plastic dilatancy during plastic flow. For well-consolidated powder materials, it is a decrease in the density which is the major reason for the post-yield strain-softening observed in these materials. Let ρ_0 denote the initial mass density of the material, and ρ_p the mass density in the intermediate space after plastic deformation. In our theory, we account for the *change in the density* of a cohesive powder-consolidated material from its virgin state by the *plastic volumetric strain*

$$\eta = \ln(\rho_0/\rho_p) = \ln\, J^p,$$

where $J^p = \det \mathbf{F}^p$. Since $\dot{\eta} = \mathrm{tr}\,\mathbf{D}^p$, using eq. $(4.3)_3$ we have that

$$\dot{\eta} = \beta\, d^p. \tag{4.9}$$

We assume that the dilatancy function β depends on the current value of η,

$$\beta = \hat{\beta}(\eta). \tag{4.10}$$

Further, at a given strain rate d^p, we assume that the cohesion c decreases

[5]Rate-independent versions of our flow rule are broadly used to model the plastic response of granular materials in which pressure-sensitivity and plastic dilatancy are quite pronounced. We emphasize that we do not assume that $\mu = \beta$, which would correspond to an associated/normality flow rule.

as the material softens due to the decrease in the density during the course of deformation. This is modelled phenomenologically by constructing an evolution equation (cf. (4.27))

$$\dot{c} = \hat{\dot{c}}(\eta, d^p), \tag{4.11}$$

with the value of the cohesion c decreasing as η increases at a given plastic strain rate d^p.

The details of the development of a thermodynamically-consistent pressure-sensitive and plastically-dilatant elastic-viscoplastic theory are similar to that for a theory for amorphous metallic materials developed recently by Anand and Su (2005), and are not reproduced here. Instead, we simply summarize our resulting special constitutive equations, which relate the following basic fields:

ψ,	free energy density per unit volume of intermediate space,
$\boldsymbol{\chi}$,	motion,
$\mathbf{F} = \nabla\boldsymbol{\chi}$, $\quad J = \det\mathbf{F} > 0$,	deformation gradient,
$\mathbf{F}^p$, $\quad J^p = \det\mathbf{F}^p > 0$,	plastic deformation gradient,
$\mathbf{F}^e = \mathbf{F}\mathbf{F}^{p-1}$, $\quad J^e = \det\mathbf{F}^e > 0$,	elastic deformation gradient,
$\mathbf{F}^e = \mathbf{R}^e\mathbf{U}^e$,	polar decomposition of $\mathbf{F}^e$,
$\mathbf{U}^e = \sum_{\alpha=1}^{3} \lambda_\alpha^e \mathbf{r}_\alpha \otimes \mathbf{r}_\alpha$,	spectral decomposition of $\mathbf{U}^e$,
$\mathbf{E}^e = \sum_{\alpha=1}^{3} (\ln \lambda_\alpha^e)\mathbf{r}_\alpha \otimes \mathbf{r}_\alpha$,	logarithmic elastic strain,
$\mathbf{E}_0^e = \mathbf{E}^e - \frac{1}{3}(\epsilon^e)\mathbf{1}$,	deviatoric elastic strain,
$\mathbf{T}$, $\quad \mathbf{T} = \mathbf{T}^\top$,	Cauchy stress,
$\mathbf{T}^e = \mathbf{R}^{e\top}(J^e\mathbf{T})\mathbf{R}^e$,	stress conjugate to elastic strain $\mathbf{E}^e$,
$\eta = \ln J^p$,	plastic volumetric strain
$c > 0$,	cohesion,
$\mu \geq 0$,	internal friction coefficient,
β,	dilatancy parameter.

The set of constitutive equations is summarized below:

1. **Free energy**:

$$\tilde{\psi}(\mathbf{E}^e, \eta) = G|\mathbf{E}_0^e|^2 + \frac{1}{2}K(\mathrm{tr}\,\mathbf{E}^e)^2, \tag{4.12}$$

with

$$G = \hat{G}(\eta) > 0, \quad K = \hat{K}(\eta) > 0, \tag{4.13}$$

the elastic shear modulus and bulk modulus, which depend on the plastic volumetric strain η.

2. **Equation for the stress**:

$$\mathbf{T}^e = \frac{\partial \tilde{\psi}(\mathbf{E}^e, \eta)}{\partial \mathbf{E}^e} = 2G\mathbf{E}_0^e + K\,(\mathrm{tr}\,\mathbf{E}^e)\mathbf{1}. \tag{4.14}$$

Dissipative stress:

The dissipation inequality in the theory is

$$\boldsymbol{\Sigma}\colon \mathbf{D}^p > 0 \quad \text{for} \quad \mathbf{D}^p \neq 0, \tag{4.15}$$

where the thermodynamically-consistent driving stress $\boldsymbol{\Sigma}$ for plastic flow is given by (Anand and Su (2005), their Equations (43-51))

$$\boldsymbol{\Sigma} \stackrel{\text{def}}{=} \mathbf{T}^e - \underbrace{\Big(\tilde{\psi}(\mathbf{E}^e, \eta) + \frac{\partial \tilde{\psi}(\mathbf{E}^e, \eta)}{\partial \eta}\Big)\mathbf{1}}_{\text{this term originates due to plastic dilatancy}} . \tag{4.16}$$

The quantities

$$\bar{\tau} \stackrel{\text{def}}{=} \frac{1}{\sqrt{2}}\,|\boldsymbol{\Sigma}_0|, \qquad \bar{p} \stackrel{\text{def}}{=} -\frac{1}{3}\mathrm{tr}\,\boldsymbol{\Sigma}, \tag{4.17}$$

define an *equivalent shear stress*, and a *mean normal pressure*, respectively. In the case of no dilatancy, the term $\dfrac{\partial \tilde{\psi}(\mathbf{E}^e, \eta)}{\partial \eta}$ will disappear automatically. The influence of $\tilde{\psi}(\mathbf{E}^e, \eta)$ will also vanish due to the fact that $\mathrm{tr}\mathbf{D}^p = 0$ and hence $\tilde{\psi}(\mathbf{E}^e, \eta)\mathbf{1}\colon \mathbf{D}^p = 0$.

3. **Flow rule**:

The evolution equation for $\mathbf{F}^p$ is

$$\dot{\mathbf{F}}^p = \mathbf{D}^p \mathbf{F}^p, \qquad \mathbf{F}^p(\mathbf{X}, 0) = \mathbf{1}, \tag{4.18}$$

with $\mathbf{D}^p$ given by

$$\left.\begin{aligned} \mathbf{D}^p &= d^p \left(\frac{\boldsymbol{\Sigma}_0}{2\bar{\tau}} + \frac{1}{3}\beta \mathbf{1} \right), \quad \text{with} \\ d^p &= d_0 \left\{ \frac{\bar{\tau}}{c + \mu \bar{p}} \right\}^{1/m} \geq 0, \end{aligned} \right\} \tag{4.19}$$

where $c > 0$ and $\mu \geq 0$ are internal variables called the *cohesion* and *internal friction*, respectively; also d_0 is a *reference plastic shear strain rate*, and $m > 0$ is a *strain-rate-sensitivity parameter*. The term $\mu\bar{p}$ accounts for pressure-sensitivity of plastic flow, and the quantity β is a *shear-induced plastic dilatancy function*.

For $d^p > 0$, the flow equation $(4.19)_2$ may be inverted to read

$$\bar{\tau} = \{c + \mu \bar{p}\} \left(\frac{d^p}{d_0} \right)^m ; \tag{4.20}$$

thus, the limit $m \to 0$ renders the flow stress to be *rate-independent*.

The dissipation inequality (4.15) requires that

$$\boldsymbol{\Sigma} : \mathbf{D}^p = [\bar{\tau} - \beta \bar{p}]\, d^p \; > 0 \tag{4.21}$$

whenever plastic flow occurs. Thus, whenever $d^p > 0$, we must have

$$[\bar{\tau} - \beta \bar{p}] > 0; \tag{4.22}$$

this is a *restriction* that the dilatancy function β must satisfy.

We account for the *change* in the density a cohesive powder-consolidated ma-

terial from its virgin state by the *plastic volumetric strain* $\eta = \ln J^p$, and take the dilatancy function to be given by

$$\beta = g_0 \left(1 - \frac{\eta}{\eta_{cv}}\right), \tag{4.23}$$

where g_0 and η_{cv} are positive-valued material parameters. Thus, $\beta = 0$ when $\eta = \eta_{cv}$, and η_{cv} denotes the value of the plastic volume change in a fully-developed constant plastic volume state.

4. **Evolution equations for η, c and μ:**

For the cohesive powder-consolidated nanocrystalline materials under consideration we take the internal friction μ to be a positive constant,[6]

$$\mu \equiv \text{constant} > 0. \tag{4.24}$$

By definition $\eta = \ln J^p$, and therefore $\dot{\eta} = \operatorname{tr} \mathbf{D}^p$. Thus using (4.19) we have,

$$\dot{\eta} = \beta d^p, \tag{4.25}$$

and with β given by (4.23), the evolution equation for η becomes

$$\dot{\eta} = g_0 \left(1 - \frac{\eta}{\eta_{cv}}\right) d^p, \qquad \eta(0) = 0\,. \tag{4.26}$$

The evolution of the cohesion c is in general a function of η and d^p, with c decreasing as the material softens due to the increase in the value of η during the course of inelastic deformation at a fixed strain rate d^p. This is modelled

[6]There is not enough experimental information available to be more definitive about the evolution of μ at this time.

by introducing the following phenomenological function for the evolution of c:

$$\left.\begin{aligned} \dot{c} &= \left[h_0 \left|\left(1-\frac{c}{c^*}\right)\right|^a \operatorname{sign}\left(1-\frac{c}{c^*}\right)\right] d^p, \quad \text{with} \\ c^* &= \bar{c}\left(\frac{d^p}{d_0}\right)^n + b(\eta_{cv}-\eta)\,, \quad \text{and initial value} \\ c(0) &= c_0\,. \end{aligned}\right\} \tag{4.27}$$

The *material constants* used in the coupled evolution equations (4.27) and (4.26) to describe the *rate-dependent* strain-hardening or softening response of the material are

$$\{h_0, a, c_0, \bar{c}, n, b, g_0, \eta_{cv}\}\,.$$

The quantity c^* in (4.27) represents a "saturation" value of c which depends on η and d^p: $\dot{c}$ is positive for $c < c^*$ which corresponds to strain-hardening, and negative for $c > c^*$ which corresponds to strain-softening.

We have implemented our constitutive model in the finite-element computer program ABAQUS/Explicit (Abaqus, 2005) by writing a user material subroutine. We apply this numerical capability to model the response of nc-Cu and nc-Mg in § 3 and § 4 below.

4.3 Application to nc-Cu

In this section we apply our constitutive model to describe the response of the powder-consolidated nc-Cu reported in (Cheng et al., 2005). Unlike the nc-Mg, which exhibits strain-softening (cf. Fig. 3-2), the true stress-strain curves for the nc-Cu of Cheng et al. (2005) (cf. their Fig. 4b) do not exhibit any softening until very near final failure. To model such a stress-strain response, our constitutive model may be *considerably simplified* by neglecting the effects of the plastic volumetric strain and its evolution. Specifically, the plastic dilatancy part of the flow rule may be set to zero with $\beta = 0$, so that $\dot{\eta} = 0$. c^* and $\bar{c}$ are identical in this case. The friction coefficient

μ may also be neglected,[7] and the evolution equation for the cohesion may be taken in the simple form

$$\dot{c} = \left[h_0 \left|\left(1 - \frac{c}{c^*}\right)\right|^a\right] d^p, \quad \text{with} \quad c(0) = c_0\,. \tag{4.28}$$

Thus, in the simplified model the material parameters are the elastic shear and bulk moduli (G, K); the parameters $\{d_0, m\}$ in the flow rule; and the parameters $\{h_0, a, c_0, c^*\}$ in the evolution equation (4.28) for c.

Cheng et al. (2005) conducted their experiments on dog-bone-shaped sheet tensile specimens which were electro-discharge machined from their consolidated Cu. A finite-element mesh of such a sheet tensile specimen is shown in Fig. 3-4a. Using this three-dimensional specimen geometry and the implementation of our constitutive model in ABAQUS/Explicit (Abaqus, 2005), we conducted numerical tension tests, and adjusted the material parameters in our model to obtain a curve-fit to the engineering stress-strain curves of Cheng et al. (2005). The curve-fit is shown in Fig. 3-4b; the fit at all three strain rates for major portions of the engineering stress-strain curves is reasonable. Since our model is intended to represent only the inelastic deformation of these materials, and does not contain provisions to model failure, it clearly cannot capture the final failure process observed in the experiments. The material parameters used to obtain the curve-fit shown in Fig. 3-4b are listed in Table 4.3.

G = 45 GPa,	K = 140 GPa,	d_0 =0.001,	m=0.026
h_0 =45 GPa,	a = 1.2,	c_0 = 330 MPa,	c^*=395 MPa.

Table 4.2: Estimated material constants for nc-Cu.

Contour plots for the equivalent plastic shear strain

$$\bar{\gamma}^p = \int d^p\, dt,$$

[7]Cheng et al. (2005) do not report results form compression experiments for us to determine a value for this constitutive parameter.

keyed to points b, c and d on the engineering stress-strain curve at a strain rate of 10^{-4}/s, Fig. 3-5a, are shown in Figs. 3-5b through d. The numerical simulation shows the classical diffuse-necking, which eventually gives way to intense localized-necking which occurs at an angle of $\approx 55^{\circ}$ to the tensile axis. A photograph of the corresponding experimentally-measured localized-neck reported by Cheng et al. (2005) (their Fig. 8b) is shown in Fig. 3-5e. The qualitative similarity between the numerical simulation and experimental observation is very encouraging.

4.4 Application to nc-Mg

In this section we apply our model to describe the deformation behavior of nc-Mg. Unlike the nc-Cu discussed in the previous section, the nc-Mg exhibits rate-dependent strain-softening, and we need the complete model of § 2 to describe the response of this material. Recall that the material parameters in our model are (i) the elastic shear and bulk moduli (G, K); (ii) the parameters $\{d_0, m, \mu\}$ in the flow rule; and (iii) the parameters $\{h_0, a, c_0, \bar{c}, n, b, g_0, \eta_{cv}\}$ in the evolution equations for c and η.

In this case, since we have data for the true stress-strain curves from our own tension and compression experiments, we used a single ABAQUS/C3D8R element to conduct numerical simulations in tension and compression. We judiciously adjusted the values of the material parameters to fit the model to the data of Fig.3-2b and c. The results of our curve-fitting procedure are shown in Fig. 3-6a and b. The material parameters used to obtain the fit are listed in Table 3.[8]

G = 17 GPa,	K = 50 GPa,		
d_0 =0.0001,	m=0.03,	μ = 0.03,	
h_0 =6.4 GPa,	a = 1.2,	c_0 = 200.0 MPa,	$\bar{c}$ = 187.0 MPa,
n = 0.04,	b = 36 GPa,	η_{cv} = 1.0× 10^{-3},	g_0 = 0.015.

Table 4.3: Estimated material constants for nc-Mg.

[8]For simplicity we have neglected any dependence of the elastic moduli on the plastic volumetric strain η.

Next, in order to check the predictive capabilities of our constitutive model, we carried out axisymmetric finite-element simulations of micro-indentation experiments with a conical indenter which has a half-cone angle of 70.3°. The undeformed finite-element mesh is shown in Fig. 3-7a. The simulations were conducted at three different loading rates of 0.5, 5, and 50 mN/s. The load (P) versus indentation depth (h) curves at these different loading rates are shown in Fig. 3-7b. As expected, because of the intrinsic strain-rate sensitivity of the nc-Mg, the indentation P-h curves also show significant loading rate-sensitivity. Corresponding micro-indentation experiments were performed on the nc-Mg, and the experimentally measured P-h, are shown in and compared against the numerically-simulated curves in Fig. 3-7c.[9] The numerically simulated P-h curves agree reasonably-well with the corresponding experimental curves.

4.5 Discussion and conclusion

In order to model the macroscopic response of powder-consolidated nanocrystalline metals, we have developed a finite-deformation elastic-plastic constitutive model, in which the plastic flow is taken to be rate- and pressure-dependent, plastically dilatant, and non-normal. The results of our study show that this model, when suitably calibrated and numerically implemented, may be used with reasonable accuracy to simulate the deformation behavior of the important emerging class of nanocrystalline materials, which exhibit not only high strength but also a reasonable amount of ductility. However, much work still remains to be done to study and model the ductile fracture processes that are operative in these materials.

[9] Approximately ten indentation experiments were carried out at each loading rate to ensure the repeatability of the P-h curves.

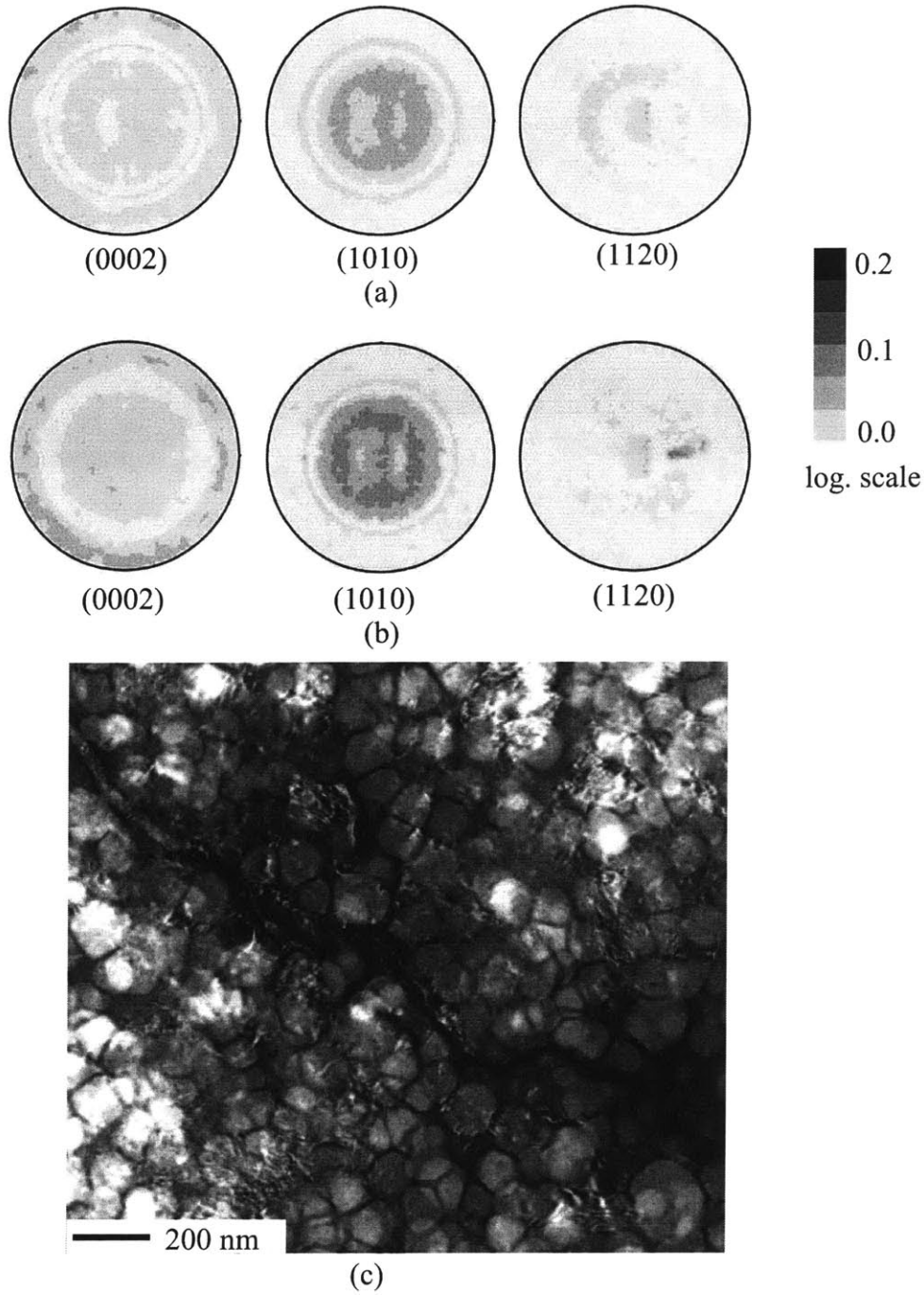

Figure 4-3: (a) Initial crystallographic texture for the nc-Mg as represented by pole figures for the {0002}, {1010}, and {1120} (b) Pole figures after 15% compressive strain. Note that there is very little difference in the pole figures after deformation relative those before, indicating that there is little twinning or lattice re-rotation due to slip after 15% strain. (c) TEM micrograph of specimen after 15% compression showing decohesion at grain-boundaries.

(a)

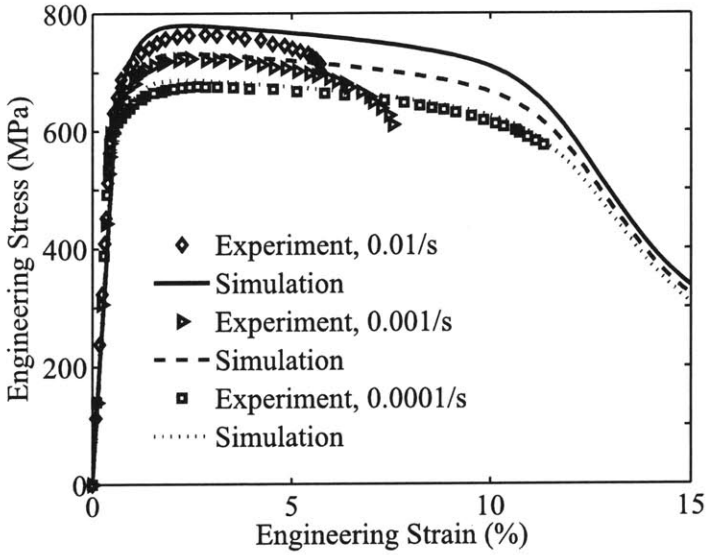

(b)

Figure 4-4: Deformation of a thin-sheet sample under tension. (a) A 3D view of the initial meshed structure with dimensions similar to these of the sample tested by Cheng et al. (2005) (b) Fitted stress-strain curves at three different strain rate using the meshed structure in (a).

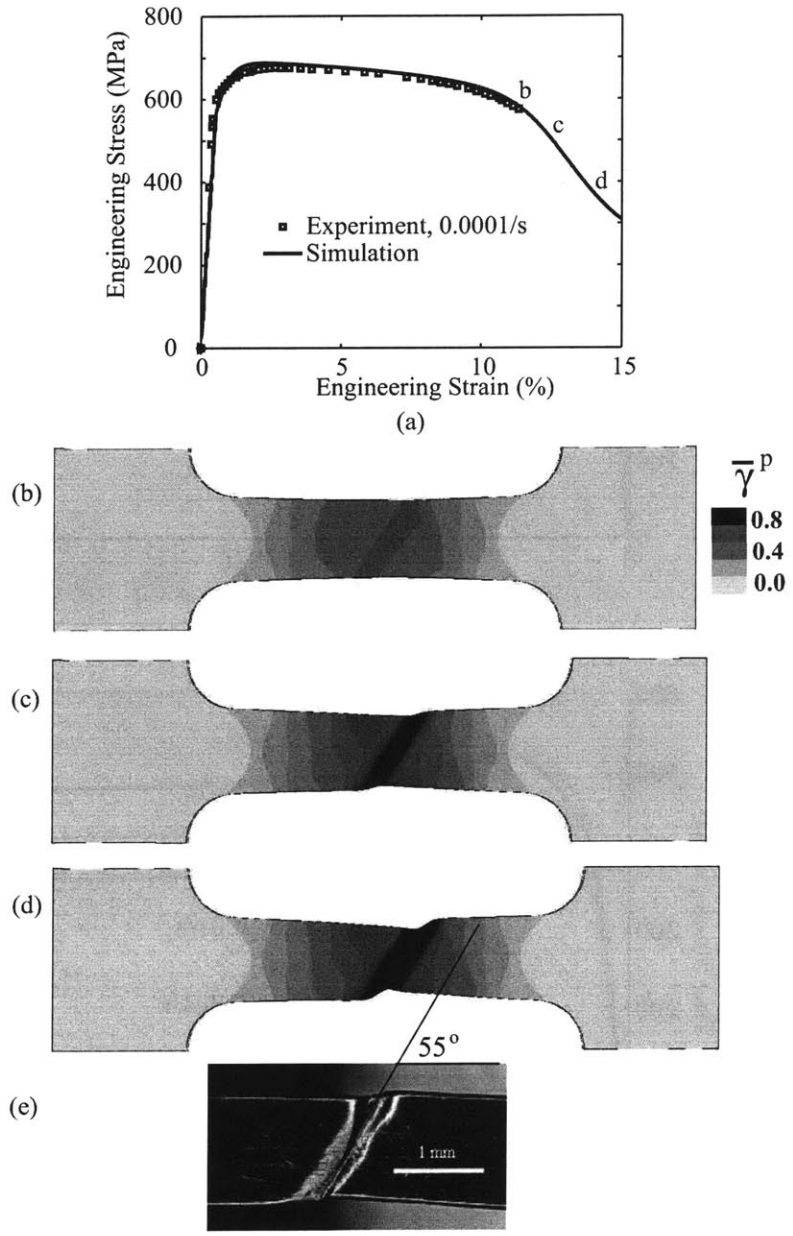

Figure 4-5: Deformation pattern of the thin-sheet sample under tension. (a) The stress-strain curves from the simulation and the experiment for nc-Cu at a strain rate of 10^{-4}/s. (b-d) Equivalent plastic strain contour of the thin-sheet sample at different stress status keyed on the stress-strain curve in (a), which show the necking process. (e) Deformation pattern of the necked sample in Cheng et al. [2].

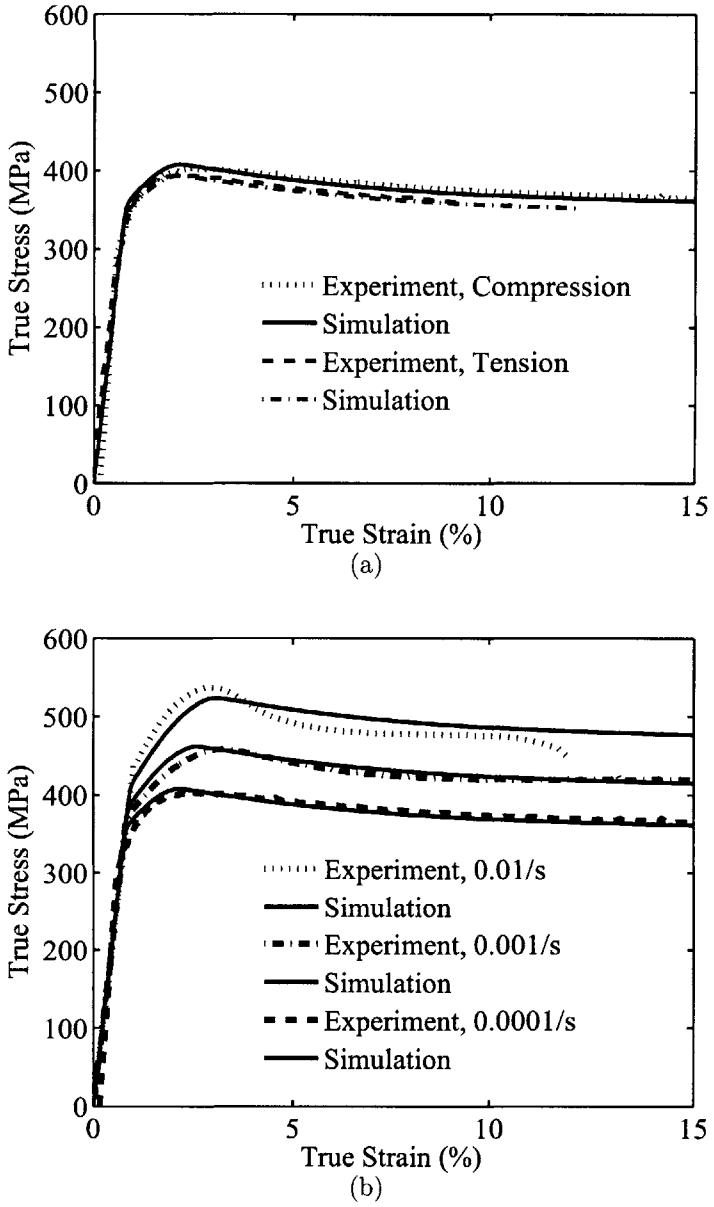

Figure 4-6: (a) Stress-strain curves of nc-Mg predicted by the model versus these from experiments at the referential strain rate with a magnitude 0.0001/s. (b) Comparison for the predicted stress-strain curves with experimental results for nc-Mg under compression with different strain rates.

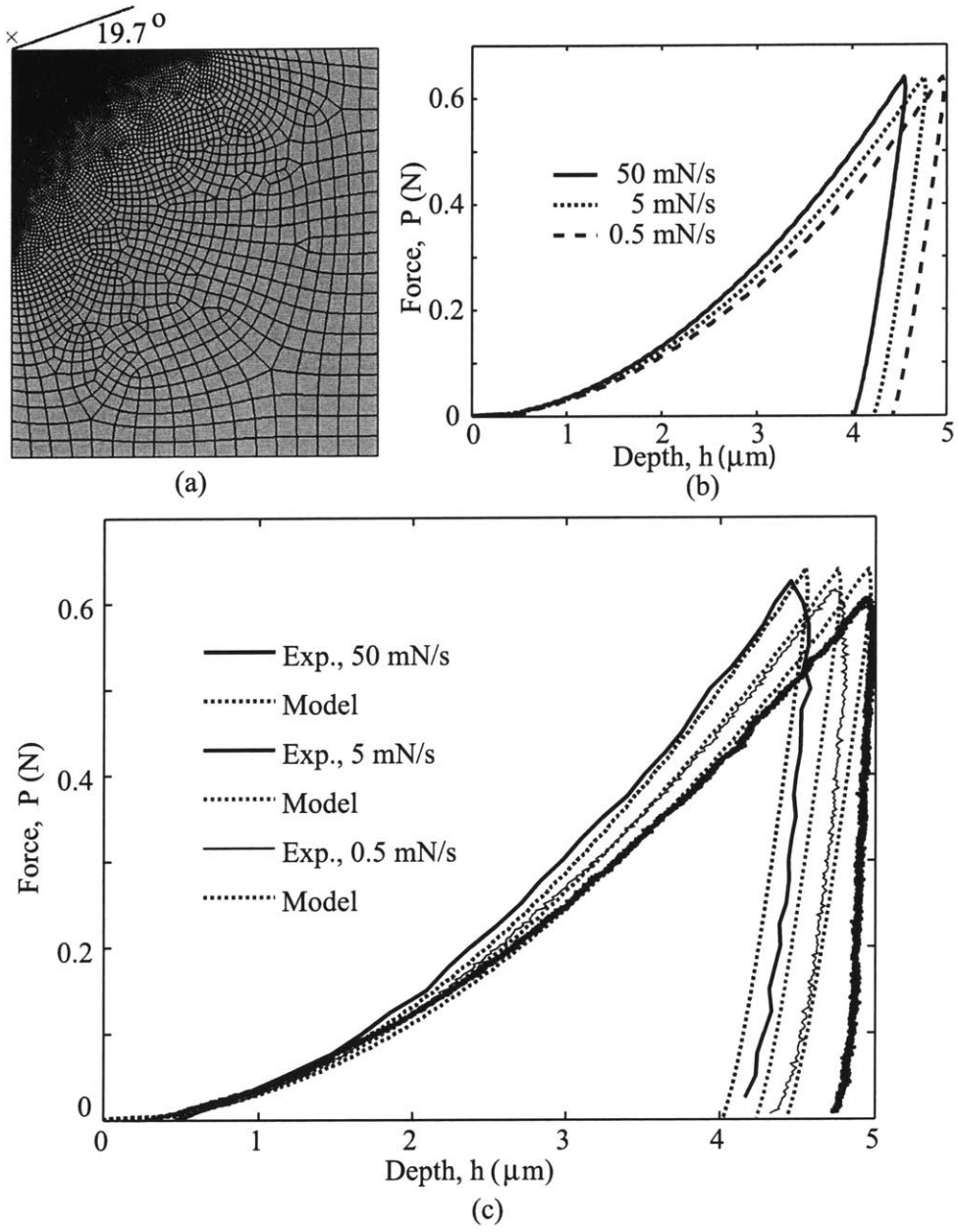

Figure 4-7: Conical indentation on nc-Mg at different loading rate versus model predictions. (a) Axis-symmetric conical indentation mesh used in Abaqus (explicit) microindentation simulations. (b) Load versus depth at different loading rates from model. (c) Comparison between modeling and experimental results.

Chapter 5

Summary and future work

Significant advancement in the synthesis and deformation mechanisms of high strength nanocrystalline materials have been achieved due to the worldwide research effort. A broad picture of the operative micromechanisms of inelastic deformation in this class of materials at low homogeneous temperature range is beginning to emerge. Much of the understanding of the micromechanisms operative during the inelastic deformation of nanocrystalline materials has been obtained from the large-scale molecular dynamics (MD) studies published in the past few years. Although such MD methods of studying atomic level mechanical response of materials are useful for gaining valuable insight, these methods are at present not suitable for carrying out simulations of deformation and failure under conditions similar to which physical experiments on nanocrystalline materials are carried out; that is, macroscopic-sized specimens with complicated boundary conditions, involving realistic strain rates. In order to obtain stress-strain responses of nc materials at laboratory length and time-scales, there is space for developing continuum constitutive models for the deformation of nc materials.

The purpose of this thesis is to develop constitutive modeling strategy to investigate the deformation mechanisms of nc materials, with emphasis on f.c.c. nc nickel and h.c.p. nc magnesium. To this end, several modeling strategies at a continuum frame were developed to capture the experimentally observed mechanical and deformation behavior in nc materials. Two different methods have been developed to

capture the deformation for grain boundaries in nc materials. We first considered a grain boundary is governed by the interaction of two coupled surfaces belonging to the two neighboring grains. Mechanical response due to the interactions between two coupled surfaces is controlled by traction-separation laws. Next, in order to capture the enhanced strain-rate dependence in fcc and hcp nc materials as grain size reduces, a viscoplastic amorphous constitutive model is applied to capture deformation in grain boundaries with finite thickness of ~1nm. Finally, a constitutive model for powder-processed nanocrystalline material, where the plastic flow could pressure-dependent, plastically-dilatant, and non-normal, has been developed. A brief summary on accomplished thesis work is given here.

5.1 Interface model

A new interface is developed to capture the mechanical behavior in grain boundaries. Most previous interface models are of the *non-linear reversible elastic* type. The new interface model that we have developed accounts for both reversible elastic, *as well as irreversible inelastic separation-sliding* deformations at the interface prior to failure. The interface traction-separation model has been implemented in the finite element program ABAQUS/Explicit (Abaqus, 2005) by writing a USER INTERFACE subroutine. As a first application of our model, we have considered the widely studied problem of modelling the behavior of adhesively-bonded components. We showed that our new model, when suitably calibrated against a suite of experiments to determine the constitutive parameters in the interface model for aluminum components bonded by a polymeric adhesive, is able to reasonably-well predict the macroscopic load-displacement curves of several different verification experiments: four-point bend tests, peel tests, and single- and double-lap joint tests. Our study of the mechanical response of nc-nickel is summarized in Su et al. (2004).

5.2 Quasi-static: rate-independent traction-separation law for GBs

Given the uncertainties of ascribing a finite width to grain boundaries, as existed in those "core-and-mantle" type of models, we (Wei and Anand, 2004) developed an alternate modeling approach to account for the combined effects of grain-boundary-related deformation as well as dislocation-mediated plasticity within the grains. We have coupled our new interface traction-separation model with an isothermal, rate-independent crystal-plasticity model for the grain interior to model the behavior of nc-materials. We have used the new computational capability to study the deformation and fracture response of an aggregate of crystals. Such a computational capability may serve as a *meso-scale simulation tool* to study the deformation and fracture response of polycrystals whose individual crystals may be in the $\leq 100\,\text{nm}$ size range. The results from the simulations capture the experimentally-observed stress-strain curves, and the dominant fracture mechanisms in nc-Nickel. Our study of the mechanical response of nc-nickel has been published (Wei and Anand, 2004).

5.3 Rate-effect: Amorphous GB layers

In the modeling strategy with traction-separation law to represent grain boundary response, the tensile and shear properties of the cohesive grain boundaries were estimated by fitting results of numerical simulations to experimentally-measured stress-strain curves for electrodeposited nc-Ni. Unfortunately, such a fitting procedure makes it difficult to unambiguously characterize the grain boundary properties. Meanwhile, on the continuum frame, there are two important issues we could address for the modeling of nc metals which are missing in the previously modeling. Firstly, considering the enhanced strain-rate effects observed in most f.c.c. nc metals, it is of importance to take the rate-dependent GB deformation behavior into consideration. Secondly, recent continuum theory on grain boundary emitted dislocations show a transition between the emission of perfect dislocation and partial dislocation. For

grain sizes from about several hundred nanometers to about 10~20nm, grain interior plastic deformation is mainly accommodated via perfect dislocations emitted in grain boundaries. At even smaller grain sizes, grain boundary emitted partial dislocations may be the primary source for grain interior plastic strain.

In this part, we took the two missing factors stated above into account in a mesoscopic continuum model for nc materials. Motivated by the fact that the lower size limit for nc materials would be bulk amorphous materials, we treated the non-equilibrium, more or less disordered grain boundaries in nc material as amorphous layers with finite thickness of 1 nm. Such a treatment for grain boundaries doesn't necessarily represent the precise nature of all, especially some grain boundaries in nc materials synthesized by electrodeposition which may be quite sharp and clean. The double shear model developed by Anand and Su (2005)) for amorphous metals which accounts for rate-dependent deformation, shearing and cavitation failure mechanisms in grain boundaries, is adopted to represent the mechanical response in grain boundaries in nc materials. For grain interiors, conventional crystal plasticity model is used as an indicator for plastic deformation in grain interiors when grain sizes are greater than the transitional grain size. For grain sizes smaller than the transitional grain size, partial dislocations on confined slip systems account for the dominant plastic deformation in grain interiors. A different flow rule, which accounts for the influence of stacking fault, has been adopted. This part of work has been compiled and submitted for publication.

5.4 Macroscopic model for powder-consolidated nc materials

The models we have developed in the last two chapters can serve as mesoscopic models to better our understanding in the deformation behavior in grain boundaries and grain interiors of nc materials, at a laboratory attainable time scale. The synthesis of nc materials has advanced to a stage that bulk materials with nanoscale

microstructures can be produced. For their engineering application, it is of interest to constitutive models for nanocrystalline materials which could be applied to analyze mechanical behavior of these materials at macroscopic level. We have conducted a series of mechanical and microstructure characterizations for nc magnesium synthesized by powder-consolidation. Motivated by the observed mechanical properties and deformation mechanisms in powder-consolidated nc magnesium, as well as powder-consolidated nc metals from literature, we have develop a thermodynamically-consistent and frame-indifferent model for the large deformation response of pressure-sensitive and plastically-dilatant elastic-viscoplastic materials which may be idealized to be isotropic. Using our numerical finite-element-based capability, we show that our constitutive model may be used with reasonable accuracy to simulate the response of the nc-Cu and nc-Mg in some representative boundary-value problems.

5.5 Future work

Continuum modelings on nc materials and interfacial failures are still in their infancy. Further work remains to be done in these models to quantitatively accounts for the failure behavior of grain boundaries and interfaces. It is desired to develop more physically based interface traction-separation relations, which might vary widely depending on grain boundary misorientations, porosity, grain boundary thickness, impurities in a grain boundaries, for the case of nanocrystalline materials. Also interfacial decohesion and crack propagation associate closely with material properties; environments; and the imposed loading conditions. When considering the time-dependent deformation in cracking zone and the influence of impurities, they add extra levels of complexity, in engineering structures subject to such factors.

5.5.1 Thermal-mechanical coupled grain boundary behavior in nc materials and thin films

It is well known that grain boundary diffusion is much faster than lattice diffusion, and surface diffusion is much faster than grain boundary diffusion. In structures like thin films and nc materials applied in elevated temperature, their thermal and mechanical liability depends on the property of grain boundaries in such environment. The grain boundary properties are governed by thermally-activated, stress-assisted diffusion. It is meaningful to develop thermally-mechanically coupled constitutive modeling strategy to investigate the liability of such nanostructures in their application.

5.5.2 Influence of impurities to cracking

As concerned in technical applications, the effect of impurity atoms on slow decohesion where the impurity concentration in the decohering zone evolves with time, a coupled process of diffusion and decohesion, has long been a list of standing problems. Stress-corrosion cracking, hydrogen embrittlement in high strength steel, sulfur-induced embrittlement of nickel, for example, have been found and investigated for centuries; and are commonly referred as environment-assisted cracking. It is of scientific importance to know how the stress, concentration of sulfur or hydrogen will weaken grain boundaries; what is the critical stress status, concentration of sulfur or hydrogen to induce decohesion and the transition from intragranular ductile deformation to intergranular brittle behavior for materials. Physical based theory and modeling may could reasonably prediction the liability and the life span of structures subject to the influence by factors we stated. Utilizing the rapid growing computational capability, I am planning to conduct atomistic simulations to gain atomistic level mechanisms on the influence of impurities to the decohesion of grain boundaries. The atomistic scale mechanisms will then input to continuum models. Hence we may be able to have physical sound base for the deformation mechanisms embedded in continuum models and could obtain simulation with laboratory accessible time and length scale.

5.5.3 Material design with layered structures

Layered natural and bio-materials have recently attracted the interest of the mechanical engineering and material science fields. Nacre, a composite containing > 95 $vol\%$ interlocking aragonite platelets staggered in consecutive laminae and surrounded by < 5 $vol\%$ protein-polysaccharide matrix, has a fracture toughness 3000 times higher than that of pure aragonite. The mechanical properties of polymeric materials (proteins) and mineral bridges between aragonite platelets are the key for the overall strength and toughness of nacre. Mechanical experiments have shown that the failure in this kind of materials mainly occur in their interfaces. I am planning to develop micro-mechanical models capture the local and global deformations in these materials and understand their design motif for high strength and high ductility.

5.6 Conclusion and remarks

In this thesis, We have developed different continuum constitutive models to investigate the competing deformation mechanisms in grain boundaries and grain interior in nc materials, the influence of microstructure and testing condition upon the mechanical response. Investigation is focusing on grain sizes where grain interior plastic deformation and grain boundary deformation contribute competitively to accommodate applied boundary conditions. The models could serve as bridges from atomistic scale to macroscopic continuum level. In the foreseen future, such a modeling strategy should be the main methods in the modeling of nanocrystalline materials with the laboratory attainable time and length scales. The developed numerical could be applied to many structures with interface/grain boundary embedded, where the interfaces/grain boundaries might be the main issue for the mechanical or thermal liability of the integrated systems.

Appendix A

Interface model and its application on adhesively bonded structure

A.1 Introduction

Cohesive interfaces between bodies in natural and man-made systems are ubiquitous, and the initiation and development of fracture by sliding and separation at such interfaces is widely observed. Common examples are (i) at the geological scale, the boundaries between the plates on the surface of the earth are cohesively bonded at asperity contacts, and the initiation and development of relative sliding between plate boundaries often results in earthquakes; (ii) at the scale of engineering structures, many systems are built by adhesively bonding different components, and the mechanical failure of such systems often occurs because of the failure of the bonded interfaces; and (iii) at the microscopic level, in metallic, ceramic and rock-like polycrystalline materials, fracture initiation and propagation due to grain boundary interface failure is also a relatively common occurrence.

Cohesive interface modelling of fracture started more than 40 years ago with the work of Barenblatt (1959) and Dugdale (1960). In recent years, cohesive surface models have been widely used to numerically simulate fracture initiation and growth

[1]The work in this appendix is published in *Int. J. Plasticity* by Su, Wei and Anand, 2004, **20**, 2063.

by the finite-element method (cf., e.g., Needleman 1990; Xu and Needleman 1994; Camacho and Ortiz 1996), for a recent review see Hutchinson and Evans (2000). Typically, a set of cohesive surfaces are introduced in the finite element discretization by the use of special interface elements which obey a non-linear interface traction-separation constitutive relation which provides a phenomenological description for the complex microscopic processes that lead to the formation of new traction-free crack faces. The loss of cohesion, and thus of crack nucleation and extension, occurs by the progressive decay of interface tractions. The interface traction-separation relation usually includes a cohesive strength and cohesive work-to-fracture. Once the local strength and work-to-fracture criteria across an interface are met, decohesion occurs naturally across the interface, and traction-free cracks form and propagate along element boundaries. An important characteristic of this methodology for modelling fracture initiation and propagation is that macroscopic fracture criteria, based on elastic or elastic-plastic analyses, such as $K_I = K_{IC}$ or $J_I = J_{IC}$, are not needed, because material strength and toughness, and crack nucleation and propagation, are all characterized by the local traction-separation relation and the cohesive surface methodology.

Although substantial progress has been made in recent years, there are still several key issues that need to be addressed in the cohesive surface modelling of fracture. Specifically, (i) Most previous interface models are of the *non-linear reversible elastic* type. For example, in (Xu and Needleman, 1994), with $\boldsymbol{\delta}$ denoting the displacement jump across the cohesive surface, and $\mathbf{t}$ the work-conjugate traction vector on the surface, the constitutive equation for the cohesive surfaces is expressed in terms of a potential function φ, such that the traction $\mathbf{t} = \partial\varphi/\partial\boldsymbol{\delta}$. The specific form for φ chosen by

citepxu1994 is history- and rate-independent, and this leads to a traction-displacement relation which is fully reversible. It appears that the interface constitutive model of (Xu and Needleman, 1994) is intended to represent the cohesive behavior of *initially defect free* interfaces, and thus in some sense to describe the *ideal strength* of solids. There exists a need to develop interface constitutive models which allow for *inelas-*

ticity at the interface prior to failure, much in the spirit of elastic-plastic constitutive equations which govern the deformation of the bulk material.[1] (ii) While it is relatively straightforward to construct a traction-separation relation for normal separation across an interface to model mode I conditions, elastic-plastic traction-separation relations for combined opening and sliding, together with the experimental methods needed to determine the parameters that might enter such coupled interface constitutive relations, are not well-developed. [2]

In this chapter, we will present a continuum-level interface constitutive model which accounts for both reversible elastic, as well irreversible inelastic separation-sliding deformations at the interface prior to failure. We have implemented our constitutive model in the finite-element computer program ABAQUS/Explicit (Abaqus, 2005) by writing a USER INTERFACE subroutine. As a first application of our model we consider the widely studied problem of modelling the behavior of adhesively-bonded components.[3] We show that our new model, when suitably calibrated against a set of experiments to determine the constitutive parameters for aluminum components bonded by a polymeric adhesive, is able to reasonably well predict the macroscopic load-displacement curves of three different verification experiments using (a) T-peel specimens, (a) four-point bending of bi-layer edge-notch specimens, and (b) lap-shear specimens.

The plan of this chapter is as follows. In § 2 we develop our interface constitutive model. In § 3 we describe our experiments to calibrate the material parameters in the model for aluminum components bonded by a polymeric adhesive, and verify the predictive capabilities of our constitutive model and computational procedures for the deformation and fracture response of adhesively-bonded components. We close

[1] Camacho and Ortiz (1996) do allow for a form of inelasticity. They consider interface constitutive equations in which the initial cohesive response is rigid, and there is a finite traction at which softening occurs; they also allow loading/unloading irreversibility, with linear unloading to the origin.

[2] This is true even for two-dimensional problems, and this issue is expected to be substantially more complicated in three dimensions.

[3] Cohesive interface models have been widely used to investigate interfacial failure of bi-material systems, e.g., Tvergaard and Hutchinson 1992, 1996 and Thouless and co-workers (Yang et al. 1999, 2000; Yang and Thouless 2001; Kafkalidis and Thouless 2002). The major difference between these previous studies and the present work is the use of our new interface constitutive model.

in § 4 with some final remarks.

A.2 Interface constitutive model

We consider two bodies $\mathcal{B}^+$ and $\mathcal{B}^-$separated by an interface $\mathcal{I}$ (Fig. 2-4). Let $\{\hat{\mathbf{e}}_1, \hat{\mathbf{e}}_2, \hat{\mathbf{e}}_3\}$ be an orthonormal triad, with $\hat{\mathbf{e}}_1$ aligned with the normal $\mathbf{n}$ to the interface, and $\{\hat{\mathbf{e}}_2, \hat{\mathbf{e}}_3\}$ in the tangent plane at the point of the interface under consideration.

Let $\boldsymbol{\delta}$ denote the displacement jump across the cohesive surface, and $\mathbf{t}$ the power-conjugate traction, such that $\mathbf{t} \cdot \dot{\boldsymbol{\delta}}$ gives the power per unit area of the interface in the reference configuration.

We assume that the displacement jump may be additively decomposed as

$$\boldsymbol{\delta} = \boldsymbol{\delta}^e + \boldsymbol{\delta}^p, \tag{A.1}$$

where $\boldsymbol{\delta}^e$ and $\boldsymbol{\delta}^p$, respectively, denote the elastic and plastic parts of $\boldsymbol{\delta}$. Then,

$$\mathbf{t} \cdot \dot{\boldsymbol{\delta}} = \mathbf{t} \cdot \dot{\boldsymbol{\delta}}^e + \mathbf{t} \cdot \dot{\boldsymbol{\delta}}^p. \tag{A.2}$$

Let φ denote a free-energy per unit surface area in the reference configuration. We consider a purely mechanical theory based on the following local energy imbalance that represents the first two laws of thermodynamics under isothermal conditions,

$$\dot{\varphi} \leq \mathbf{t} \cdot \dot{\boldsymbol{\delta}}. \tag{A.3}$$

Then, using (A.2), the field

$$\Gamma = \mathbf{t} \cdot \dot{\boldsymbol{\delta}}^e + \mathbf{t} \cdot \dot{\boldsymbol{\delta}}^p - \dot{\varphi} \geq 0 \tag{A.4}$$

represents the **dissipation** per unit reference area.

We assume that the free-energy φ is given by

$$\varphi = \hat{\varphi}(\boldsymbol{\delta}^e). \tag{A.5}$$

Then, using standard arguments, (A.4) gives

$$\mathbf{t} = \frac{\partial \hat{\varphi}(\boldsymbol{\delta}^e)}{\partial \boldsymbol{\delta}^e} \tag{A.6}$$

and

$$\Gamma = \mathbf{t} \cdot \dot{\boldsymbol{\delta}}^p \geq 0. \tag{A.7}$$

We are concerned with interfaces in which the elastic displacement jumps are small, but but the plastic displacement jumps may be arbitrarily large. For small elastic displacement jumps we assume a simple quadratic free-energy φ

$$\varphi = \frac{1}{2}\boldsymbol{\delta}^e \cdot \mathbf{K}\boldsymbol{\delta}^e, \tag{A.8}$$

with $\mathbf{K}$, the interface elastic stiffness tensor, positive definite. In this case (A.6) gives

$$\mathbf{t} = \mathbf{K}\boldsymbol{\delta}^e = \mathbf{K}(\boldsymbol{\delta} - \boldsymbol{\delta}^p). \tag{A.9}$$

We consider an interface model which is *isotropic* in its tangential response, and take $\mathbf{K}$ to be given by

$$\mathbf{K} = K_N \mathbf{n} \otimes \mathbf{n} + K_T(\mathbf{1} - \mathbf{n} \otimes \mathbf{n}), \tag{A.10}$$

with $K_N > 0$ and $K_T > 0$ normal and tangential elastic stiffness moduli.

The interface traction $\mathbf{t}$ may be decomposed into normal and tangential parts, $\mathbf{t}_N$ and $\mathbf{t}_T$, respectively, as

$$\mathbf{t} = \mathbf{t}_N + \mathbf{t}_T, \quad \mathbf{t}_N \equiv (\mathbf{n} \otimes \mathbf{n})\,\mathbf{t} = (\mathbf{t} \cdot \mathbf{n})\,\mathbf{n} \equiv t_N \mathbf{n} \quad \mathbf{t}_T \equiv (\mathbf{1} - \mathbf{n} \otimes \mathbf{n})\,\mathbf{t} = \mathbf{t} - t_N \mathbf{n}. \tag{A.11}$$

The quantity t_N represents the *normal stress* at the interface. We denote the magni-

tude of the tangential traction vector $\mathbf{t}_T$ by

$$\bar{\tau} \equiv \sqrt{\mathbf{t}_T \cdot \mathbf{t}_T} \,, \tag{A.12}$$

and call it the *effective tangential traction*, or simply the *shear stress*.

We take the elastic domain in our elastic-plastic model to be defined by the interior of the intersection of two convex yield surfaces.[4] The yield functions corresponding to each surface are taken as

$$\Phi^{(i)}(\mathbf{t}, s^{(i)}) \leq 0, \qquad i = 1, 2, \tag{A.13}$$

and henceforth we indentify the index $i = 1$ with a "normal" mechanism, and the index $i = 2$ with a "shear" mechanism. The scalar internal variable $s^{(1)}$ represents the deformation resistance for the normal mechanism, and $s^{(2)}$ represents the deformation resistance for the shear mechanism. In particular, we consider the following simple specific functional form for the yield functions:

$$\Phi^{(1)} = t_N - s^{(1)} \leq 0, \qquad \Phi^{(2)} = \bar{\tau} + \mu t_N - s^{(2)} \leq 0, \tag{A.14}$$

where μ represents a *friction coefficient*. The surface $\Phi^{(i)} = 0$ denotes the ith yield surface in traction space, and

$$\mathbf{n}^{(1)} = \frac{\partial \Phi^{(1)}}{\partial \mathbf{t}} = \mathbf{n}, \qquad \mathbf{n}^{(2)} = \frac{\partial \Phi^{(2)}}{\partial \mathbf{t}} = \frac{1}{\sqrt{1+\mu^2}} \Big(\frac{\mathbf{t}_T}{\bar{\tau}} + \mu \mathbf{n} \Big) \tag{A.15}$$

denote the outward unit normals to the yield surface at the current point in traction space; see Fig. 2-5.

The equation for $\dot{\boldsymbol{\delta}}^p$, the *flow rule*, is taken to be representable as a sum of the

[4] It may be possible to develop a theory with only a single yield surface with a rounded corner to model the yield response of the interface, but we have not followed this avenue.

contribution from each mechanism

$$\dot{\boldsymbol{\delta}}^p = \sum_{i=1}^{2} \nu^{(i)} \mathbf{m}^{(i)}, \qquad \nu^{(i)} \geq 0, \qquad \nu^{(i)} \Phi^{(i)} = 0, \quad \text{with} \tag{A.16}$$

$$\mathbf{m}^{(1)} = \mathbf{n}, \qquad \mathbf{m}^{(2)} = \frac{\mathbf{t}_T}{\bar{\tau}}. \tag{A.17}$$

Note that since $\mathbf{m}^{(2)} \neq \mathbf{n}^{(2)}$, we have a *non-normal* flow rule for the shear response.[5]

The evolution equations for the internal variables $s^{(i)}$ are taken as a pair of ordinary differential equations

$$\dot{s}^{(i)} = \sum_{j=1}^{2} h^{(ij)} \nu^{(j)}, \tag{A.18}$$

where the coefficients $h^{(ij)}$ denote hardening/softening moduli.

Finally, during inelastic deformation, an active mechanism must satisfy the *consistency condition*

$$\nu^{(i)} \dot{\Phi}^{(i)} = 0 \qquad \text{when} \qquad \Phi^{(i)} = 0. \tag{A.19}$$

The consistency condition serves to determine the inelastic deformation rates $\nu^{(i)}$ when inelastic deformation occurs. Straightforward calculations using (A.9) – (A.18) give

$$\dot{\Phi}^{(i)} = \mathbf{n}^{(i)} \cdot \mathbf{K} \dot{\boldsymbol{\delta}} - \sum_{j} \left[\mathbf{n}^{(i)} \cdot \mathbf{K} \mathbf{m}^{(j)} + h^{(ij)} \right] \nu^{(j)}.$$

For $\nu^{(i)} > 0$, when $\Phi^i = 0$ the consistency condition requires that $\dot{\Phi}^{(i)} = 0$. This gives the following system of linear equations for $\nu^{(i)} > 0$:

$$\sum_{j=1}^{2} A^{(ij)} \nu^{(j)} = b^{(i)}, \qquad A^{(ij)} = \mathbf{n}^{(i)} \cdot \mathbf{K} \mathbf{m}^{(j)} + h^{(ij)}, \qquad b^{(i)} = \mathbf{n}^{(i)} \cdot \mathbf{K} \dot{\boldsymbol{\delta}}. \tag{A.20}$$

We assume that *the matrix A is invertible*, so that the $\nu^{(j)}$ are uniquely determined.

[5]Such a non-normal flow rule for the shear response is common in interface models for friction, where there is strong effect of the compressive normal traction on the resistance to plastic flow, but the plastic flow in shear is essentially non-dilational.

A.2.1 Specific form for the evolution equations

Let

$$\gamma^{(1)} \stackrel{\text{def}}{=} \int_0^t \nu^{(1)}(\xi)\, d\xi, \tag{A.21}$$

$$\gamma^{(2)} \stackrel{\text{def}}{=} \int_0^t \nu^{(2)}(\xi)\, d\xi, \tag{A.22}$$

define equivalent relative plastic displacements for the two individual mechanisms, and

$$\bar{\gamma} \stackrel{\text{def}}{=} \sqrt{(\gamma^{(1)})^2 + \alpha\,(\gamma^{(2)})^2} \tag{A.23}$$

define a combined *equivalent relative plastic displacement*, where α represents a *coupling parameter* between the normal and shear mechanisms.

A simple set of evolution equations for $s^{(1)}$ and $s^{(2)}$ which represent strain-hardening response until a critical value of $\bar{\gamma} = \bar{\gamma}_c$ is reached, and a *softening response* thereafter is

$$s^{(1)} = \hat{s}^{(1)}(\bar{\gamma}), \qquad \text{with} \qquad \hat{s}^{(1)}(\bar{\gamma}) = \begin{cases} \hat{s}^{(1)}_{hard}(\bar{\gamma}) & \text{if } \bar{\gamma} \le \bar{\gamma}_c, \\ \hat{s}^{(1)}_{soft}(\bar{\gamma}) & \text{if } \bar{\gamma} > \bar{\gamma}_c \text{ and } s^{(1)} > 0. \end{cases} \tag{A.24}$$

Similarly,

$$s^{(2)} = \hat{s}^{(2)}(\bar{\gamma}), \qquad \text{with} \qquad \hat{s}^{(2)}(\bar{\gamma}) = \begin{cases} \hat{s}^{(2)}_{hard}(\bar{\gamma}) & \text{if } \bar{\gamma} \le \bar{\gamma}_c, \\ \hat{s}^{(2)}_{soft}(\bar{\gamma}) & \text{if } \bar{\gamma} > \bar{\gamma}_c \text{ and } s^{(2)} > 0. \end{cases} \tag{A.25}$$

In this case

$$\dot{s}^{(1)} = \frac{\partial\, \hat{s}^{(1)}}{\partial\, \bar{\gamma}} \dot{\bar{\gamma}} = \frac{1}{\bar{\gamma}} \frac{\partial\, \hat{s}^{(1)}}{\partial\, \bar{\gamma}} \Big(\gamma^{(1)} \nu^{(1)} + \alpha \gamma^{(2)} \nu^{(2)} \Big), \tag{A.26}$$

$$\dot{s}^{(2)} = \frac{\partial\, \hat{s}^{(2)}}{\partial\, \bar{\gamma}} \dot{\bar{\gamma}} = \frac{1}{\bar{\gamma}} \frac{\partial\, \hat{s}^{(2)}}{\partial\, \bar{\gamma}} \Big(\gamma^{(1)} \nu^{(1)} + \alpha \gamma^{(2)} \nu^{(2)} \Big), \tag{A.27}$$

so that

$$h^{(11)} = \frac{\gamma^{(1)}}{\bar{\gamma}} \frac{\partial \hat{s}^{(1)}}{\partial \bar{\gamma}}, \quad h^{(12)} = \frac{\alpha\gamma^{(2)}}{\bar{\gamma}} \frac{\partial \hat{s}^{(1)}}{\partial \bar{\gamma}}, \quad h^{(21)} = \frac{\gamma^{(1)}}{\bar{\gamma}} \frac{\partial \hat{s}^{(2)}}{\partial \bar{\gamma}}, \quad h^{(22)} = \frac{\alpha\gamma^{(2)}}{\bar{\gamma}} \frac{\partial \hat{s}^{(2)}}{\partial \bar{\gamma}}. \tag{A.28}$$

A simple explicit constitutive time-integration procedure for the interface model is summarized in the Appendix. The model, using this time-integration, has been implemented in the finite element program ABAQUS/Explicit (Abaqus, 2005) by writing a user-interface subroutine.

A.3 Application to adhesively-bonded components

In this section we consider the application of our model to predict the deformation and failure response of adhesively-bonded components. In particular, we shall consider components made from the aluminum alloy 6061-T6, bonded by the ductile polymeric adhesive Hysol EA 9361. Surfaces of the components to be bonded were first roughened with medium-grit emery paper, degreased with acetone, and thoroughly cleaned in alcohol, as recommended by the adhesive manufacturer. The interface between the adhesively-bonded components was controlled to a nominal thickness of $100\,\mu$m by inserting a wire of this diameter between the adherends while preparing the bond. We emphasize that the polymeric adhesive is not treated as an interfacial continuum layer with its own constitutive stress-strain model, but as the interface whose response (i.e., traction vs displacement jump) is governed by the model proposed in the previous section.[6]

The aluminum alloy was modeled as a rate-independent isotropic elastic-plastic material using the classical J_2-flow theory of the plasticity.[7] A Young's modulus

[6] In general bulk polymeric materials exhibit a significant rate sensitivity of inelastic response. For the thin film polymeric adhesives one would also expect the inelastic traction-separation response to be rate-dependent, but there is insufficient experimental evidence at this stage to quantify such a response. Accordingly, as a first attempt, we have approximated the response the Hysol adhesive to be *rate-independent* for the narrow ranges of separation rates examined in our application.

[7] We have used ABAQUS's built-in implementation of such a model. Specifically, using standard notation, with $\mathbf{T}^{\nabla} = \dot{\mathbf{T}} - \mathbf{W}\mathbf{T} + \mathbf{T}\mathbf{W}$ denoting the Jaumann derivative of the Cauchy stress $\mathbf{T}$, $\mathbf{W}$ the spin, and $\mathbf{D}$ the stretching, the constitutive equation for the stress is taken as $\mathbf{T}^{\nabla} = \boldsymbol{\mathcal{C}}[\mathbf{D} - \mathbf{D}^p]$, with $\boldsymbol{\mathcal{C}} = \frac{E}{(1+\nu)}\boldsymbol{\mathcal{I}} + \frac{E\nu}{(1+\nu)(1-2\nu)}\mathbf{1} \otimes \mathbf{1}$ the isotropic elasticity tensor, where E is the Young's modulus

of 62.50 GPa, a Poisson's ratio of 0.33, an initial yield strength of 300 MPa, were used, and the strain-hardening characteristics of the aluminum were extracted from an experimentally-measured stress-strain curve shown in Fig. A-1.

To calibrate the interface model we have conducted three sets of experiments to measure the normal and tangential response of an Al/Hysol/Al interface: (a) Direct tension experiments on butt-jointed specimens to calibrate the tension response. (b) Double-shear experiments on double-lap specimens to calibrate the shear response, and (c) Peel experiments to estimate the strain-softening response of the interface (more on this below).

Fig. A-2(a) and (c) show schematics of the direct tension and the double-lap shear specimens used to measure the normal and shear response, respectively. A non-contacting optical extensometer system was used to measure the relative opening and sliding displacements in the two experiments.[8] Fig. A-2(b) shows the traction-separation curve for the interface in the normal direction. The result shows the interface failed at a total relative normal separation of $\approx 22\,\mu m$ when the stress reaches a peak value of $\approx$ 24 MPa. Fig. A-2(d) shows the the traction-separation curve for the interface in shear; the maximum shear stress is $\approx 20 MPa$, and the total relative shear displacement at failure is $\approx 44\ \mu m$, twice that of the tensile response. Note that shear response shows significant "strain-hardening" prior to failure.

Referring back to equations (A.24) and (A.25), the experimental results for the *hardening portion* of the traction-separation curves were fit to the following special

---

and ν the Poisson's ratio. The yield condition is $\phi = \bar{\sigma} - s \leq 0$, where with $\mathbf{T}'$ denoting the stress deviator, $\bar{\sigma} = \sqrt{(3/2)\mathbf{T}' \cdot \mathbf{T}'}$ is the equivalent tensile stress, and s is the flow strength. The flow rule is $\mathbf{D}^p = \nu^p(3\mathbf{T}'/2\bar{\sigma})$, with $\nu^p \geq 0$ satisfying $\nu^p\phi = 0$. The evolution equation for the flow strength is $\dot{s} = h\nu^p$ with h a strain-hardening function, and initial value $s(0) = s_0$, the yield strength of the material. As is standard, the scalar plastic flow rate ν^p in a rate-independent theory is determined form the consistency condition $\nu^p\dot{\phi} = 0$ when $\phi = 0$.

[8]Before an experiment, two reference points are marked on either side of the interface on the surfaces of the aluminum plates. A CCD camera takes pictures of the region of the specimen surface which includes the reference points during the experiment at an appropriate frequency, and the images are transferred to a personal computer through an image-acquisition board. The digital image files are then processed numerically to measure the relative positions of the two marks on either side of the interface. The optical extensometer system that we have used has a sub-micron resolution.

	s_0 (MPa)	h_0 (MPa/mm)	s^* (MPa)	a	$\bar{\gamma}_c$ (μm)	h_{soft} MPa/mm	$\bar{\gamma}_{fail}$ (μm)
Tension	20.0	10000	25.0	1.6	22	2400	32
Shear	1.00	1700	24.0	1.0	22	2000	32

Table A.1: Parameters for the inelastic response of an adhesively bonded interface.

form of the evolution for the two resistances $s^{(i)}$:

$$\dot{s}^{(i)}_{hard} = h_0 \left\{ 1 - \frac{s^{(i)}}{s^{*(i)}} \right\}^{a^{(i)}} \dot{\bar{\gamma}}, \qquad \text{with initial values} \quad s^{(i)}(0) = s^{(i)}_0, \quad \text{for} \quad \bar{\gamma} \leq \bar{\gamma}_c, \tag{A.29}$$

with $s^{*(i)} \geq s^{(i)}$. Recall that we have defined the *equivalent relative plastic displacement* by

$$\bar{\gamma} = \sqrt{(\gamma^{(1)})^2 + \alpha\,(\gamma^{(2)})^2}.$$

We choose a value for the coupling parameter α by *assuming* that $\bar{\gamma}$ has the same critical value $\bar{\gamma}_c$ when the interface starts to soften in any combination of tension or shear. Thus, choosing the tension value as reference, that is $\bar{\gamma}_c = \gamma_c^{(1)} = 22\mu$m, and noting that $\gamma_c^{(2)} = 44\mu$m, we obtain

$$\alpha = 0.25,$$

for the Al/Hysol/Al interface. The numerical fit to the "hardening" portion of the experimental traction-separation curves for pure tension and shear is also shown in Fig. A-2(b) and Fig. A-2(d), respectively. The interface elastic stiffnesses used in the fit are

$$K_N = 18.9\,\text{GPa/mm}, \qquad K_T = 7.1\,\text{GPa/mm}$$

and the inelastic parameters for the interface used in the fit are listed in Table A.3:

In the simulations to follow, we take the resistance of an interface in tangential direction to be independent of the normal stress on that interface, i.e., $\mu = 0$.[9]

[9]Special compression-shear experiments will have to be devised to determine appropriate values

The interface softening response beyond the peak stresses is not measurable in the direct tension and shear experiments described above, because the large amount of elastic energy stored in the aluminum plates causes an unloading instability which masks the true constitutive response of the interface during softening. In our numerical simulations we allow for a softening branch to the interface traction-separation response, by *assuming* a simple linear softening from $\bar{\gamma}_c$ to a failure value $\bar{\gamma}_{fail}$:

$$\dot{s}^{(i)}_{soft} = -h^{(i)}_{soft}\dot{\bar{\gamma}} \quad \text{for} \quad \bar{\gamma}_c < \bar{\gamma} \leq \bar{\gamma}_{fail}. \tag{A.30}$$

The values of $h^{(i)}_{soft}$ and $\bar{\gamma}_{fail}$ were *estimated* from a set of peeling experiments in which, because the adherends are thin sheets, the load-displacement curves show a gradually softening response before failure. The geometry for the L-peel specimens used in our study is shown in Fig. A-3(a). The specimen was made from a 1.59 mm (1/16 inch) thick Al 6061-T6 sheet adhered to an Al 6061-T6 block. The experiments were carried out under displacement control at a cross-head-displacement rate of 4×10^{-3} mm/sec.

The geometry of the L-peel specimens was modelled using 1250 ABAQUS CPE4R elements for the thin sheet part interacting with a rigid surface. The constitutive response for the sheets was specified using the implementation of isotropic J_2-flow theory in ABAQUS/Explicit and the material parameters for Al6061-T6. The hardening parameters for the interface model listed in Table 1 were used in the simulations, and the softening parameters $h^{(i)}_{soft}$ were *adjusted* in the simulations to obtain a reasonable match with the measured load-displacement curve for the L-peel experiment. The best-fit values for $h^{(i)}_{soft}$ and $\bar{\gamma}_{fail}$ so obtained are also listed in Table 1, and the corresponding softening portions of the traction-separation curves are shown in Fig. A-2(b) and Fig. A-2(d), respectively. Fig. A-3(b) and Fig. A-3(c) compare the numerically-calculated (outline only) and experimentally-observed deformation of the L-peel specimen. A comparison between the experimentally-measured load-displacement curves and those from the simulations using the parameters listed in

of μ; we have not yet developed such experimental techniques for adhesively bonded interfaces.

Table 1 is shown in Fig. A-3(d). As is clear from this figure, the numerical calculations accurately reproduce all the major features of the experimentally-measured load-displacement curve, and also capture all the major features of the macroscopic deformed shape including the large plastic strains of the aluminum sheets.

With the material parameters for the Al/Hysol/Al interface and the aluminum plates calibrated, in the sections below we check the capability of our model to predict the deformation and fracture response of adhesively-bonded components in three other important configurations. In these simulations we shall use the material parameters obtained from the calibration experiments described above.

A.3.1 T-peel test

T-peeling tests were carried out to further investigate the predictive capability of the interface constitutive model. The geometry for the symmetrical T-peel test is shown in Fig. A-4(a). T-peel specimens were made with two different thicknesses of the adherend Al 60661-T6 sheets, 1.59 mm (1/16 inch) and 0.80 mm(1/32 inch), respectively. The two different sheet thicknesses were chosen to investigate the effects of different amounts of plastic deformation in the adherends on the macroscopic load-displacement curves. The experiments were carried out under displacement control at a cross-head-displacement rate of 4×10^{-3} mm/sec.

The geometry of the adherends was modeled using 2500 ABAQUS CPE4R elements. Fig. A-4(b) and Fig. A-4(c) compare the numerically-predicted (outline only) and experimentally-observed deformation of the specimens made from the 1.59 mm-thick sheets. The numerical calculations capture all the major major features of the macroscopic deformation, including the large plastic strains of the adherends. A comparison between the experimentally measured load-displacement curves and those predicted from the simulations is shown in Fig. A-4(d). As is clear from this figure, the numerical predictions accurately reproduce all the major features of the experimentally-measured load-displacement curves, and also quantitatively capture the effects of adherend thickness on the peel forces.

A.3.2 Edge-notch four-point bending specimens

As shown in Fig. A-5a, three plates of Al 6061-T6, one of which was nominally 350 mm long and the other two 175 mm long, and each of 50 mm width and 5 mm thickness, were adhesively bonded,[10] to produce a specimen with an "edge-notch" of width 100 μm and depth 5 mm.[11] Such specimens were tested in a four-point bend configuration at a constant displacement rate of 4×10^{-3} mm/sec. Because of the symmetry of the problem, one-half of the geometry was meshed using 1250 ABAQUS CPE4R elements.

Fig. A-5(b) shows a photograph of the experiment after debonding has occurred in the specimen, while Fig. A-5(c) shows a magnified image (2X) of the deformed finite element mesh in a region near the debond. The load vs displacement curves from two nominally identical experiments are shown in Fig. A-5(d). Initially, the system behaves linearly, then nonlinearity associated with the *plastic deformation of the aluminum plates sets in*, and finally debonding of the interface occurs at a load of $\approx$ 3.2KN; the load plateau is associated with a stable propagation of the debonding along the interface. Fig. A-5(d) also shows that the corresponding numerically-predicted load-displacement curve is in good accord with the experiments.

A.3.3 Lap-shear test

The geometry for our special lap-shear test is shown in Fig. A-6(a). The geometry consists of two sheets of Al 6061-T6 adhesively-bonded to a 5 mm thick 25.4 mm square piece of the same aluminum alloy, to produce two interfaces. The specimens were made with two different thicknesses of the Al 6061-T6 sheets, 1.59 mm (1/16 inch) and 0.80 mm(1/32 inch), to investigate the effects of different amounts of plastic deformation in the sheets on the macroscopic load displacement curves. As the figure shows, there is an offset between the loading axes of the two sheets; this offset will generate a moment which will rotate the middle block, and this rotation will cause

[10]The interface was prepared in a manner identical to that used in the calibration experiments described in the previous section.

[11]Specimens of this type, but of much smaller dimensions, are widely used to test the adhesion and debonding of thin-film structures, c.f., e.g., (Duskardt et al., 1998; Lane et al., 2000).

the interface to separate in a combined tension and shear mode. The experiments were carried out under displacement control at a cross-head-displacement rate of 10^{-3} mm/sec.

The geometry of the adherends was modelled using 2250 ABAQUS CPE4R elements. Fig. A-6(b) and Fig. A-6(c) compare the numerically-predicted (outline only) and experimentally-observed deformation of the specimens made from the 1.59 mm thick sheets. The numerical calculations capture all the major features of the macroscopic deformation, including the large plastic strains of the adherends and the accompanying rotations.[12] A comparison between the experimentally-measured load-displacement curves and those predicted from the simulations is shown in Fig. A-6(d). The numerical predictions accurately reproduce all the major features of the experimentally measured load-displacement curves, and also quantitatively capture the effects of the thickness of the aluminum sheets on the macroscopic force displacement curves.

A.4 Concluding Remarks

We have developed a continuum-level phenomenological interface constitutive model which accounts for both reversible elastic, as well irreversible inelastic separation-sliding deformations at the interface prior to failure. We have implemented our constitutive model in the finite-element computer program ABAQUS/Explicit (Abaqus, 2005) by writing a user interface subroutine.

We have applied the model and the numerical capability to predict the failure response of adhesively-bonded components made from the aluminum alloy 6061-T6 bonded by the ductile polymeric adhesive Hysol EA 9361. We have shown that our new model, when suitably calibrated against a set of experiments to determine the constitutive parameters, is able to reasonably well predict the macroscopic deformed

[12]Ideally, the two interfaces on either side of the middle block will have identical properties and will be identically loaded because of geometrical symmetry, so that they should fail in a similar fashion during the test, which is what actually happens in the numerical simulation. However, in the actual experiment, because of various possible minor variations, one interface always starts to fail earlier than the other.

geometries and the load-displacement curves in (a) T-peel experiments, (b) four-point bend experiments on bonded bi-layer edge-notch specimens; and (c) lap-shear experiments.

The constitutive model and the computational procedures presented here provide a new capability for the simulation and design of structures with bonded components which may be undergoing large inelastic deformations in both the adherends and the adhesives.

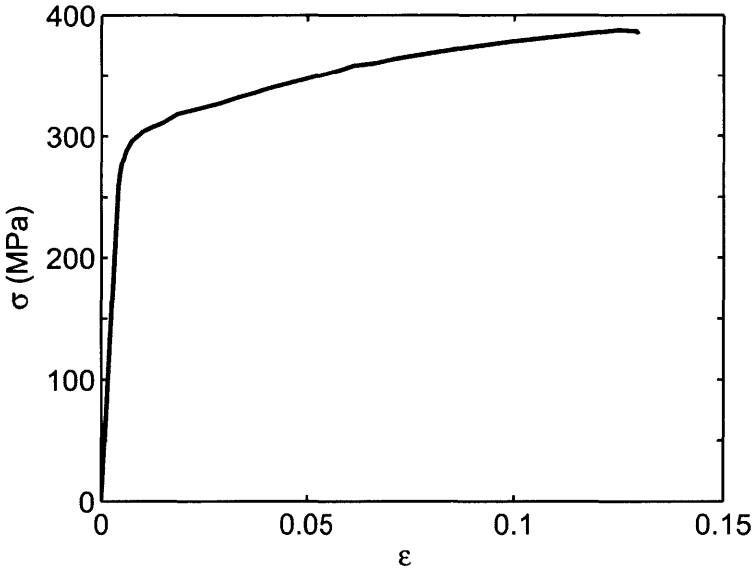

Figure A-1: True stress-strain curve for aluminum alloy 6061-T6.

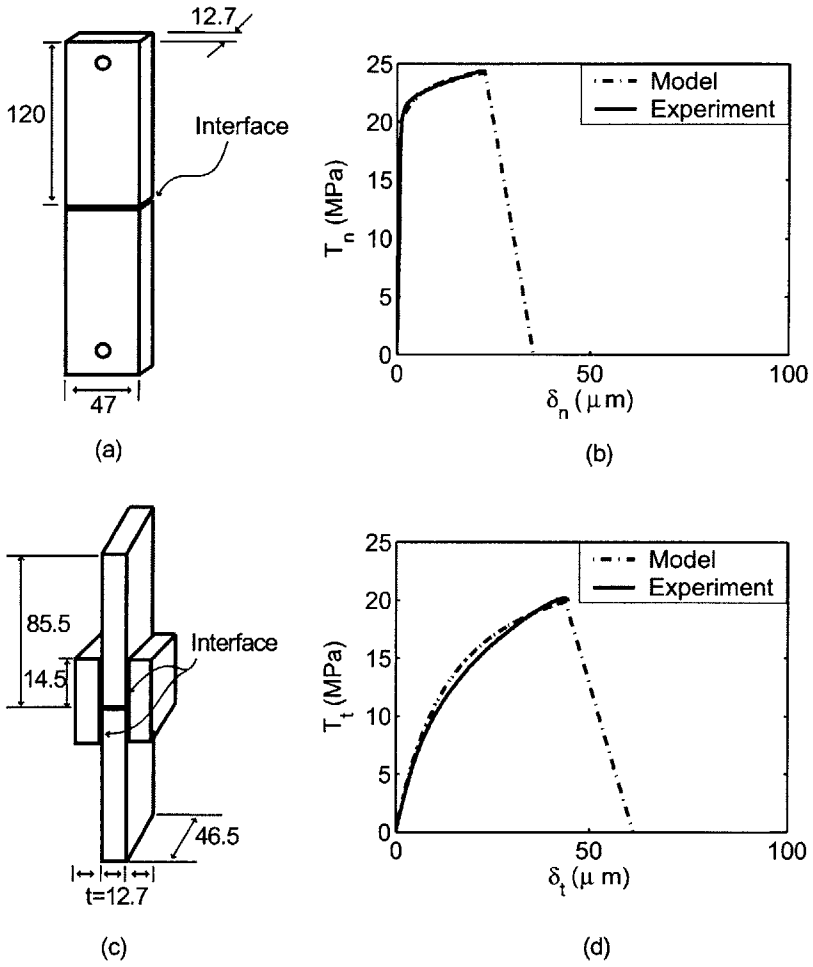

Figure A-2: Calibration of Al/Hysol/Al interface response. (a): Geometry of the specimen used for measuring the traction-separation response in the direction normal to the interface; all dimensions are in mm. (b): Traction-separation curve in the normal direction from experiment, as well as the curve-fit used in subsequent simulations. (c): Geometry of the specimen used for measuring the interface traction-separation response in shear; all dimensions are in mm. (d): Traction-separation curve in the shear direction from the experiment, as well as the curve-fit used in subsequent simulations.

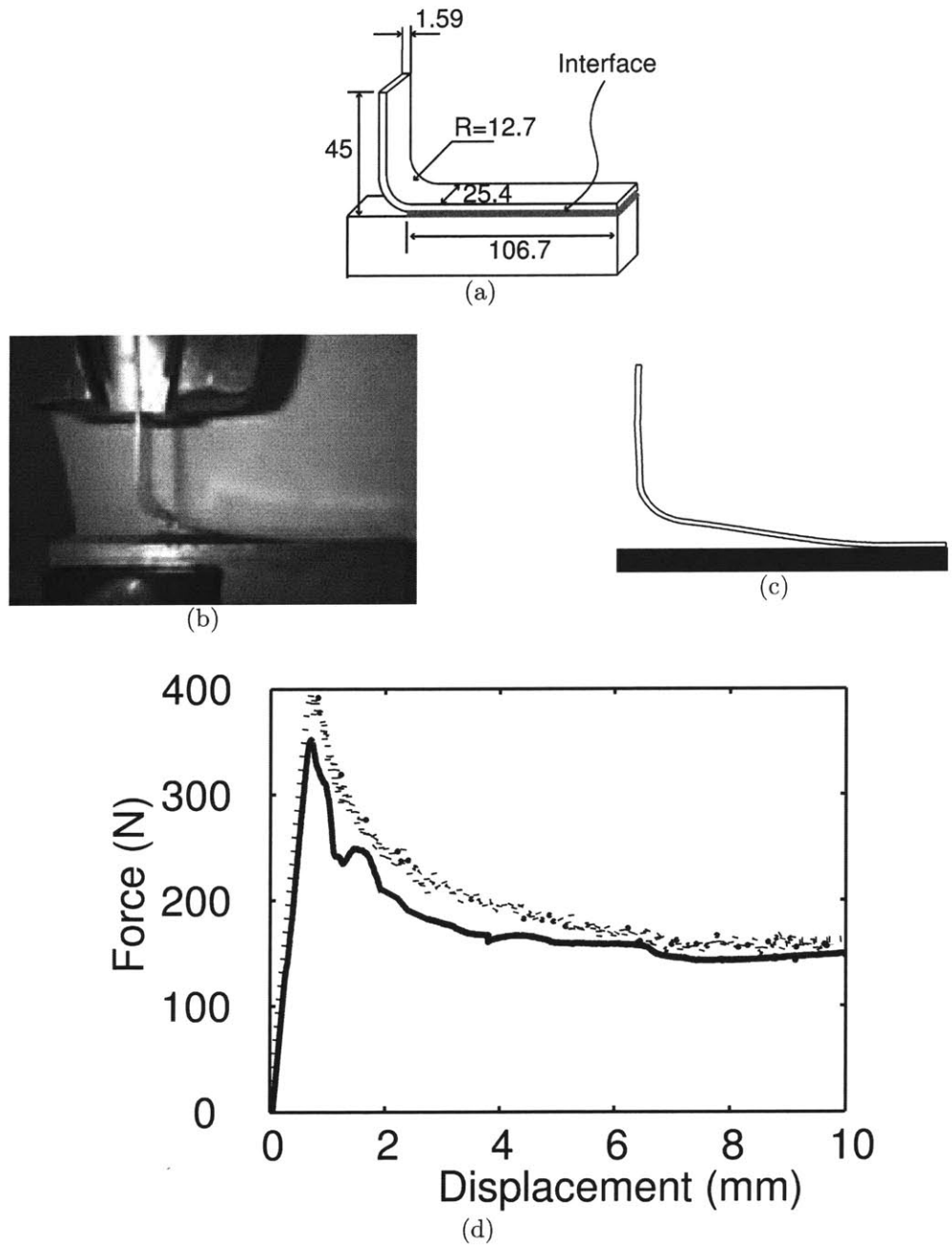

Figure A-3: L-peel experiments: (a): Geometry of the specimen; all dimensions are in mm. (b): Photograph of a deformed specimen in an experiment. (c): Deformed mesh in a corresponding numerical simulation (outline only). (d): Force versus displacement curves from the experiments conducted at a constant displacement rate of 4×10^{-3} mm/sec, compared with the corresponding result from the numerical simulation.

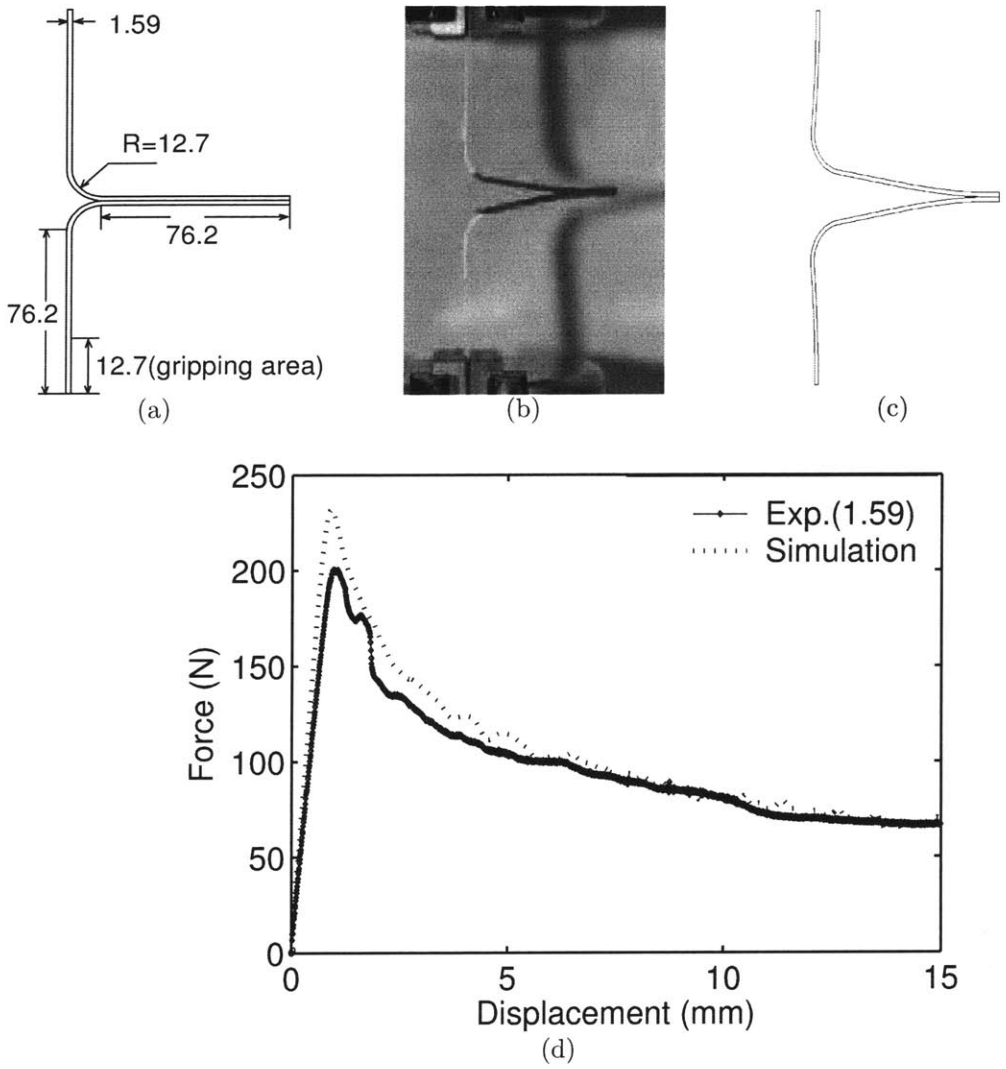

Figure A-4: T-peel experiments: (a): Geometry of the specimen; all dimensions are in mm. (b): Photograph of a deformed specimen in an experiment. (c): Deformed mesh in a corresponding numerical simulation (outline only). (d): Force versus displacement curves from the experiments conducted at a constant displacement rate of 4×10^{-3} mm/sec, compared with the corresponding result from the numerical simulation for sheet thicknesses of 1.59 mm and 0.79 mm.

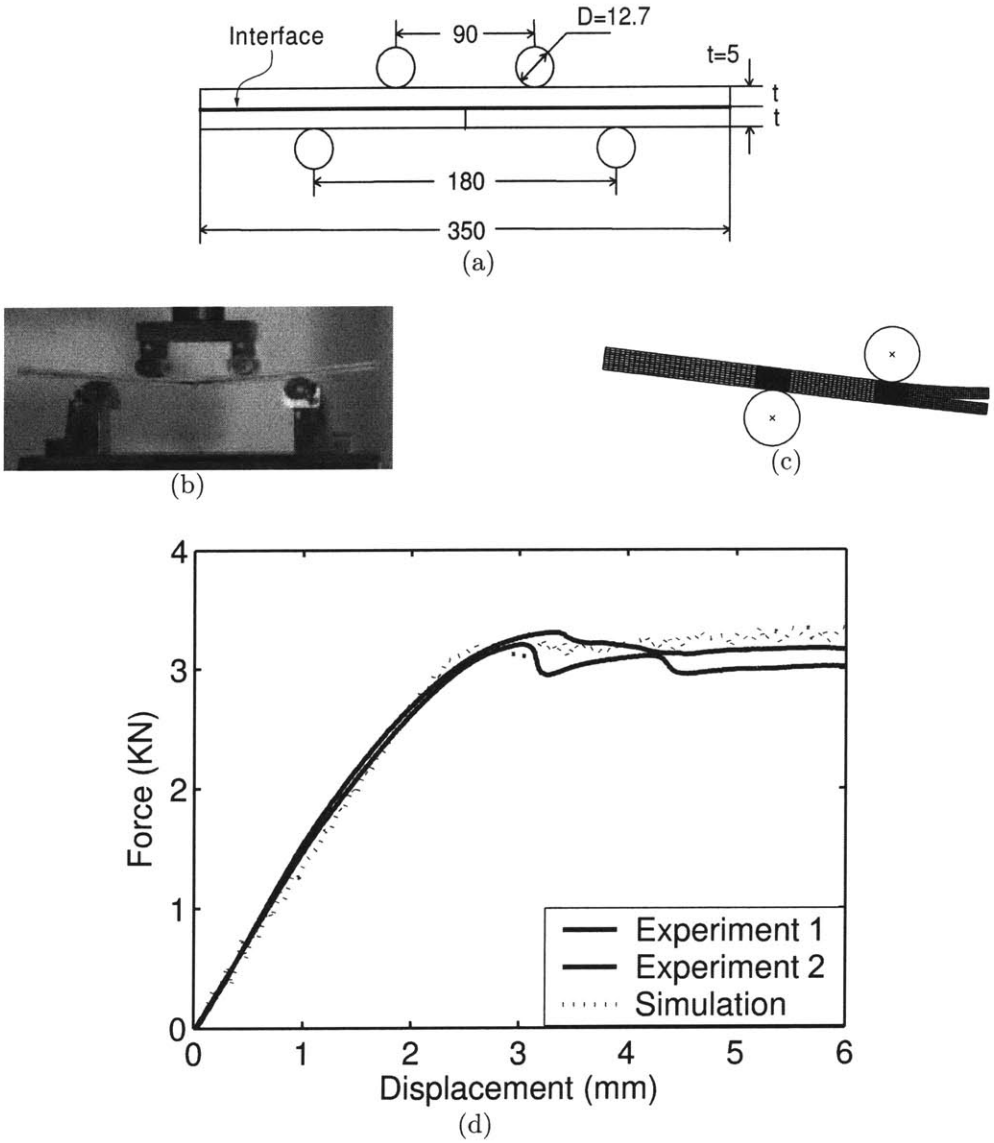

Figure A-5: Four-point bend experiments on bonded bi-layer edge-notch specimens: (a): Geometry of the specimen and the four-point bend configuration; all dimensions are in mm. (b): Photograph of a deformed specimen in an experiment. (c): Deformed mesh in a corresponding numerical simulation (magnified 2). (d): Force versus displacement curves from the experiments conducted at a constant displacement rate of 4×10^{-3} mm/sec, compared with the corresponding result from the numerical simulation.

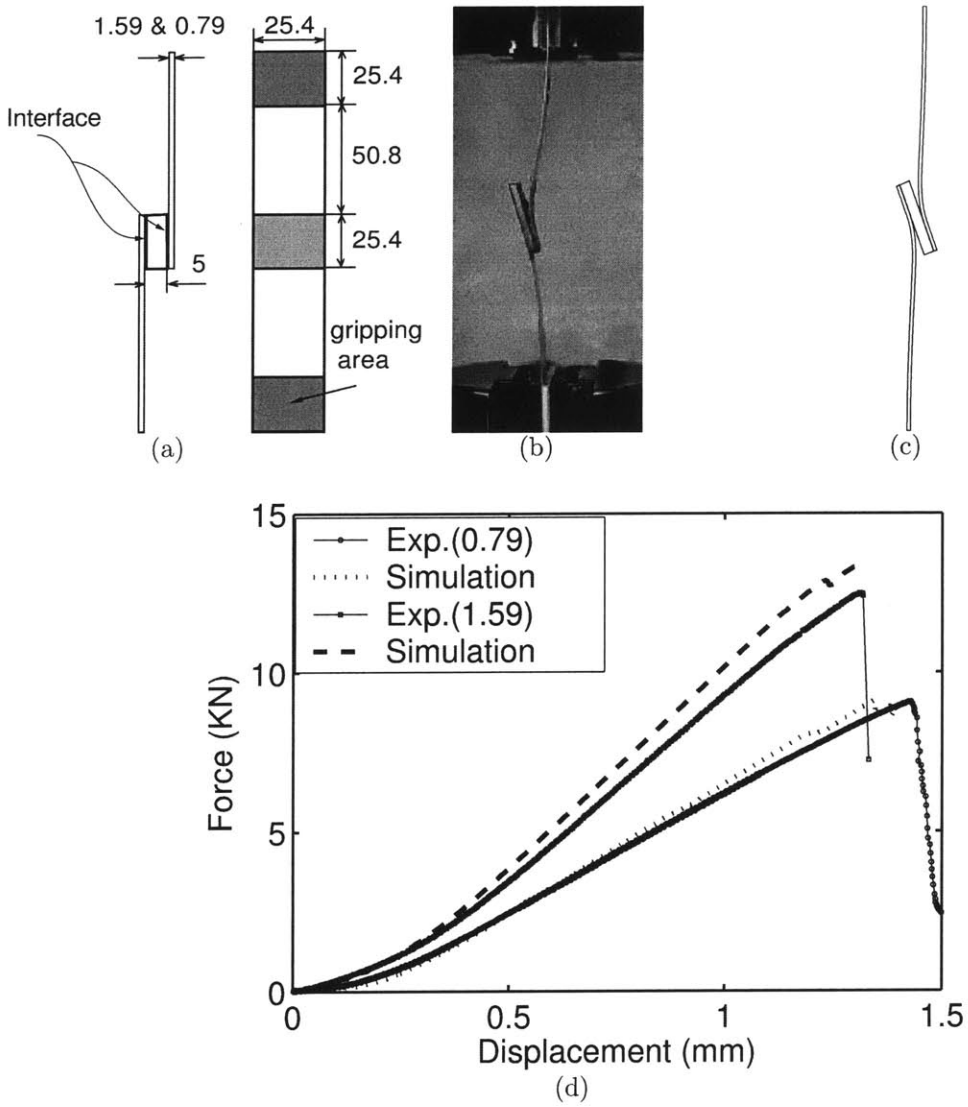

Figure A-6: Lap-shear experiments: (a): Geometry of the specimen; all dimensions are in mm. (b): Photograph of a deformed specimen in an experiment. (c): Deformed mesh in a corresponding numerical simulation (outline only). (d): Force versus displacement curves from the experiments conducted at a constant displacement rate of 10^{-3} mm/sec, compared with the corresponding result from the numerical simulation for sheet thicknesses of 0.80 mm and 1.59 mm.

Appendix B

Interface model: summary of time-integration procedure

Let $\{\hat{\mathbf{e}}_1(0), \hat{\mathbf{e}}_2(0), \hat{\mathbf{e}}_3(0)\}$ be an orthonormal triad, with $\hat{\mathbf{e}}_1(0) = \mathbf{n}$ aligned with the normal to the interface in the reference configuration, and $\{\hat{\mathbf{e}}_2(0), \hat{\mathbf{e}}_3(0)\}$ be in the tangent plane at the point of the interface under consideration. Let $\{\hat{\mathbf{e}}_1(t), \hat{\mathbf{e}}_2(t), \hat{\mathbf{e}}_3(t)\}$ be the same basis in the current configuration, with $\mathbf{e}_i(t) = \mathbf{R}(t)\mathbf{e}_i(0)$, where $\mathbf{R}(t)$ is the rotation that determines $\mathbf{e}_i(t)$. Then, the traction and the total relative displacement

$$\mathbf{t}(t) = \sum_i t_i(t)\hat{\mathbf{e}}_i(0), \quad \boldsymbol{\delta}(t) = \sum_i \delta_i(t)\hat{\mathbf{e}}_i(0), \tag{B.1}$$

may be transformed into the current configuration as

$$\tilde{\mathbf{t}}(t) = \frac{1}{J_a}\mathbf{R}(t)\mathbf{t}(t) = \frac{1}{J_a}\sum_i t_i(t)\hat{\mathbf{e}}_i(t), \tag{B.2}$$

$$\tilde{\boldsymbol{\delta}}(t) = \frac{1}{J_a}\mathbf{R}(t)\boldsymbol{\delta}(t) = \frac{1}{J_a}\sum_i \delta_i(t)\hat{\mathbf{e}}_i(t), \tag{B.3}$$

Here J_a stands for the area ratio of the current contacted area over that initial contacted area. We consider that we are given

1. $\tilde{\mathbf{t}}(t) = t_1(t)\hat{\mathbf{e}}_1(t) + t_2(t)\hat{\mathbf{e}}_2(t) + t_2(t)\hat{\mathbf{e}}_3(t)$,

2. $s^{(i)}(t)$,

3. $\gamma^{(1)}(t)$, $\gamma^{(2)}(t)$

4. $\Delta\tilde{\boldsymbol{\delta}} = \Delta\delta_1\hat{\mathbf{e}}_1(t) + \Delta\delta_2\hat{\mathbf{e}}_2(t) + \Delta\delta_3\hat{\mathbf{e}}_3(t)$,

5. $\Delta t = \tau - t$, and

6. $\mathbf{R}(t)$ which determines $\hat{\mathbf{e}}_i(t) = \mathbf{R}(t)\hat{\mathbf{e}}_i(0)$.

We need to calculate $\{\mathbf{t}(\tau), s^{(i)}(\tau), \gamma^{(1)}(\tau), \gamma^{(2)}(\tau), \}$, and march forward in time.

Step 1. Calculate the trial stress at the end of the step (components with respect to $\hat{\mathbf{e}}_i(t)$)

$$t_1^*(\tau) = t_1(t) + K_N\Delta\delta_1 \tag{B.4}$$

$$t_2^*(\tau) = t_2(t) + K_T\Delta\delta_2 \tag{B.5}$$

$$t_3^*(\tau) = t_3(t) + K_T\Delta\delta_3 \tag{B.6}$$

$$\tilde{\mathbf{t}}_T^*(\tau) = t_2^*(\tau)\hat{\mathbf{e}}_2(t) + t_3^*(\tau)\hat{\mathbf{e}}_3(t) \tag{B.7}$$

$$\bar{\tau}^*(\tau) = \sqrt{\tilde{\mathbf{t}}_T^*(\tau)\cdot\tilde{\mathbf{t}}_T^*(\tau)} = \sqrt{(t_2^*(\tau))^2 + (t_3^*(\tau))^2} \tag{B.8}$$

Step 2. Calculate $b^{(i)}$

$$b^{(1)} = \left\{t_1^*(\tau) - s^{(1)}(t)\right\} \tag{B.9}$$

$$b^{(2)} = \left(\bar{\tau}^*(\tau) + \mu t_1^*(\tau) - s^{(2)}(t)\right) \tag{B.10}$$

Step 3. Calculate $A^{(ij)}$

$$A^{(11)} = \left[K_N + h^{(11)}(t)\right] > 0 \tag{B.11}$$

$$A^{(12)} = \left[h^{(12)}(t)\right] \tag{B.12}$$

$$A^{(21)} = \left[K_N\mu + h^{(21)}(t)\right] \tag{B.13}$$

$$A^{(22)} = \left[K_T + h^{(22)}(t)\right] > 0 \tag{B.14}$$

Step 4. Calculate the plastic relative displacement increments

(a) If $b^{(1)} > 0$ and $b^{(2)} \leq 0$ then

$$x^{(1)} = \frac{b^{(1)}}{A^{(11)}} \tag{B.15}$$

$$x^{(2)} = 0 \tag{B.16}$$

(b) If $b^{(1)} \leq 0$ and $b^{(2)} > 0$ then

$$x^{(1)} = 0 \tag{B.17}$$

$$x^{(2)} = \frac{b^{(2)}}{A^{(22)}} \tag{B.18}$$

(c) If $b^{(1)} > 0$ and $b^{(2)} > 0$ then first calculate A^{-1}; recall that we have assumed that the matrix A is invertible. Then solve for the plastic strain increments

$$x^{(i)} = \sum_j (A^{-1})^{(ij)} b^{(j)} \tag{B.19}$$

Check if $x^{(i)} > 0$ then accept this solution. However, if $x^{(1)} > 0$ and $x^{(2)} < 0$ then

$$x^{(1)} = \frac{b^{(1)}}{A^{(11)}}, \qquad x^{(2)} = 0, \tag{B.20}$$

or if $x^{(2)} > 0$ and $x^{(1)} < 0$ then

$$x^{(2)} = \frac{b^{(2)}}{A^{(22)}}, \qquad x^{(1)} = 0. \tag{B.21}$$

Step 5. Update the traction

$$t_1(\tau) = t_1^*(\tau) - K_N\, x^{(1)} \tag{B.22}$$

$$\bar{\tau}(\tau) = \bar{\tau}^*(\tau) - K_T\, x^{(2)} \tag{B.23}$$

$$\tilde{\mathbf{t}}_T(\tau) = \frac{\bar{\tau}(\tau)}{\bar{\tau}^*(\tau)}\, \tilde{\mathbf{t}}_T^*(\tau) = \frac{\bar{\tau}(\tau)}{\bar{\tau}^*(\tau)}\, \{t_2^*(\tau)\hat{\mathbf{e}}_2(t) + t_3^*(\tau)\hat{\mathbf{e}}_3(t)\} \tag{B.24}$$

$$t_2(\tau) = \frac{\bar{\tau}(\tau)}{\bar{\tau}^*(\tau)}\, t_2^*(\tau) \tag{B.25}$$

$$t_3(\tau) = \frac{\bar{\tau}(\tau)}{\bar{\tau}^*(\tau)}\, t_3^*(\tau) \tag{B.26}$$

$$\tilde{\mathbf{t}}(\tau) = t_1(\tau)\hat{\mathbf{e}}_1(t) + t_2(\tau)\hat{\mathbf{e}}_2(t) + t_3(\tau)\hat{\mathbf{e}}_3(t) \tag{B.27}$$

$$\mathbf{t}(\tau) = \mathbf{R}(t)^\top \tilde{\mathbf{t}}(\tau) = t_1(\tau)\hat{\mathbf{e}}_1(0) + t_2(\tau)\hat{\mathbf{e}}_2(0) + t_3(\tau)\hat{\mathbf{e}}_3(0) \tag{B.28}$$

Step 6. Update the state variables

$$s^{(1)}(\tau) = s^{(1)}(t) + h^{(11)}(t)x^{(1)} + h^{(12)}(t)x^{(2)} \tag{B.29}$$

$$s^{(2)}(\tau) = s^{(2)}(t) + h^{(21)}(t)x^{(1)} + h^{(22)}(t)x^{(2)} \tag{B.30}$$

Step 7. Update $\gamma^{(1)}$ and $\gamma^{(2)}$:

$$\gamma^{(1)}(\tau) = \gamma^{(1)}(t) + x^{(1)} \tag{B.31}$$

$$\gamma^{(2)}(\tau) = \gamma^{(2)}(t) + x^{(2)} \tag{B.32}$$

Appendix C

Synthesis and mechanical properties of nc material: a brief review

Since the landmark paper of Gleiter (1989), lots of research efforts, from material synthesis, mechanical properties and deformation mechanism characterization, as well as physical modeling methods, have been conducted to better our understanding in nc materials, through which strong and ductile nc materials are desired. The world-wide research interest in nc materials has made tremendous progresses in this field in the last two decades. As generally accepted, the nature of the intercrystalline grain-boundary regions heavily depends on how the material has been processed. Powder-processed nc materials, for instance, inevitably contains more or less contaminations and porosity, which have a profound effect on the mechanical strength of nc materials, especially in tension. Hence it is of importance to connect the deformation and failure behavior of nc metals with their synthesis. In this part, a brief introduction to the synthesis and mechanical properties of nc materials is included.

C.1 Synthesis of nc materials

Researchers have put lots of effort to look for routes to synthesize high quality polycrystalline metals with grain sizes below 100nm, porosity free, and highly coherent grain boundaries. Most methods could be categorized into the following broadly applied routes: electrodeposition, severe plastic deformation (SPD) technique, crystallization from amorphous phases, and powder consolidation.

(i) Electrocrystallization (Erb et al. 1993, 2002) occurs either by the build up of existing crystals or the formation of new ones. These two processes are in competition with each other and are influenced by lots of factors. A schematic of pulsed electrodeposition set-up is shown in Fig. C-1, (Meyers et al. 2006). As the current spikes, the metal cations are deposited in crystalline and amorphous patches. Since grain size will grow with deposited thickness, thereby restricting the specimen geometry to thin sheets with thickness on the order of microns, to permit an average grain size in the nanoscale. Usually, electrodeposited nc materials do not require any further processing. Compared with other methods, electrodeposition could yield porosity-free finished product. Over the past two decades, the synthesis of nanostructured materials by electrodeposition has been advanced from a laboratory scale phenomenon to a practical industrial materials technology.

(ii) Severe plastic deformation (SPD) (Segal et al. 1981; Valiev and Tsenev 1991; Valiev et al. 1993, 1994) processing has been demonstrated to be an effective technique for the production of truly bulk, fully dense and contamination-free metals. It could produce polycrystalline metals with grain size in the submicron or nanometer range based on coarse grained bulk polycrystalline samples. Although any means of introducing large plastic strains in metals may lead to the reduction of the grain size, two principal methods for subjecting a material to severe plastic deformation have gained acceptance: these are known as equal-channel angular (ECA) pressing/extrusion and high-pressure torsion (HPT). The former is now a well established processing, in which an intense

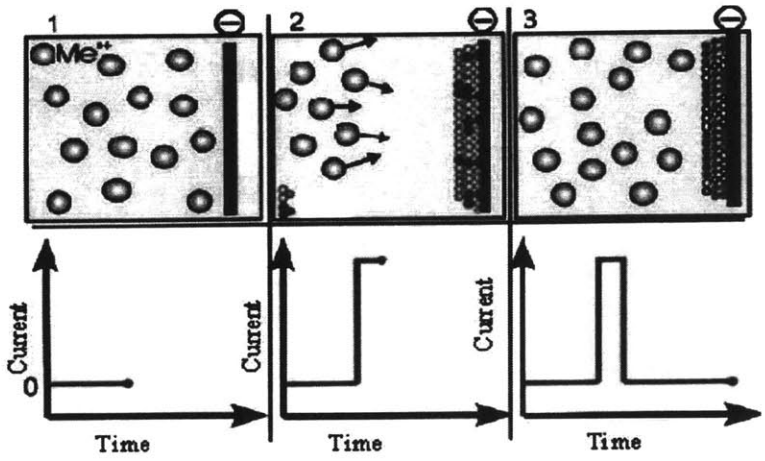

Figure C-1: Pulsed eletrodeposition set-up for synthesizing nc materials, Meyers et al. (2006).

plastic strain is introduced into a sample through simple shearing, as shown in Fig. C-2, (Iwahashi et al., 1998).

(iii) Amorphization of an alloy from the liquid state essentially involves the kinetic suppression of nucleation and growth from an undercooled melt. Versus vice, under appropriate heat treatments, thermally metastable amorphous metals could change to more stable states by generating dispersed crystallites in amorphous matrix, and eventually the amorphous phase crystallizes completely into a polycrystalline material with nanometer-sized crystallites (Yoshizawa et al. 1988; Lu et al. 1991). Such a process is believed to be able to enhance ductility of amorphous metals without losing of strength. Usually, amorphous metals have essential no plastic response in tension and a limited plastic deformation in compression not exceeding 2%. Nc materials produced out of them, however, exhibit substantial increase in ductility in both tension and compression. Also, the synthesis of nc metals through crystallization of amorphous metals has advantages in porosity-free product and easy control of synthesizing nc, intermetallic, supersaturated metallic solid solutions and composites (Meyers et al. 2006).

(vi) Powder consolidation (Groza 2002) is a compromising route for synthesis of bulk nc materials because of its relative simplicity, low cost, and the capability

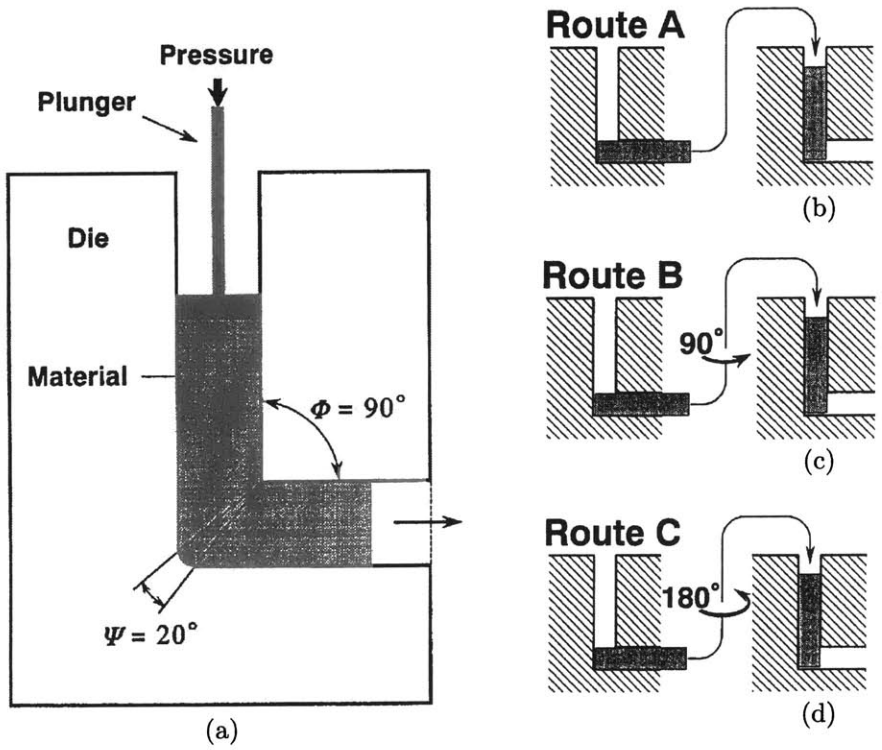

Figure C-2: Schematic illustration of the ECA pressing facility and corresponding routes, Iwahashi *et al.*, 1998. (a): One type of pressing facility showing the two angles Φ and Ψ being used. (b-d) broadly used processing routes used in current experiments.

to scale it up to tonnage quantities. Generally, steps for powder consolidation may include powder preparation, compaction, and sintering to obtain the final bulk materials. Heat treatment may be followed up to achieve better ductility. In each step, there could be several options (Groza 2002), e.g., powders could be prepared by inert gas condensation and mechanical milling. The success in nanopowder consolidation depends on the control of densification, coarsening and contamination. The densification process consists of solid particle bonding or neck formation followed by continuous closing of pores from a largely open porosity to essentially a pore-free body. To enhance particle bonding and remove possible pores during densification, high temperatures may be applied, which consequently induces undesirable grain coarsening. Therefore, people have to comprise between fully-dense and pore-free during the synthesis of powder-consolidated nc materials. Indeed, even the in-situ consolidated nc-Cu with high

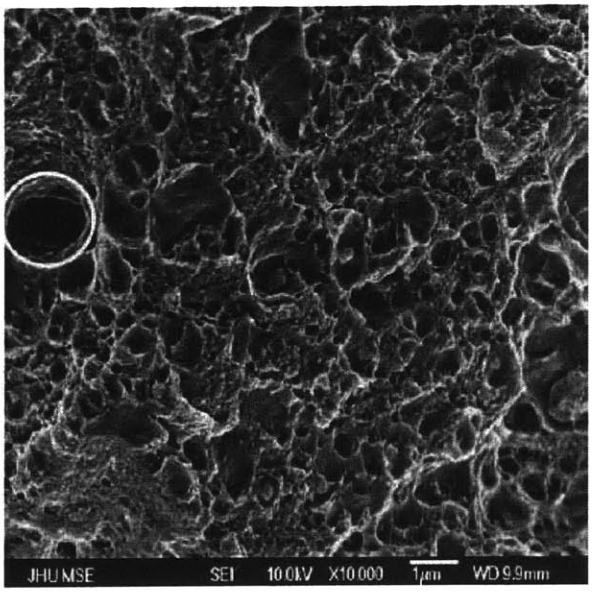

Figure C-3: Fracture surface of nc-Cu after tensile test to failure The white circle shows a pore possibly left-over after consolidation. From Cheng et al. (2005).

strength shows porosity, as seen in Fig. C-3. Another factor which may impair mechanical properties of powder-consolidated nc materials is contaminations, e.g., the uncontrolled presence of a secondary phase. Usually, powders obtained by mechanical attrition would be inevitably contaminated. For instance, oxides, nitrides and other compounds are often seen in consolidated materials made of attrition-milled nanopowders (Rawers et al. 1996; Perez et al. 1996), which might weaken the cohesion in grain boundaries.

C.2 Mechanical properties of nanocrystalline materials

The principal mechanical properties of nc metals which are of our interests include: strength, strain-rate sensitivity and ductility. As I emphasized at the beginning, grain boundary properties are of utmost importance to the mechanical behavior of nc materials. Therefore, to build up a sound structure-property relationship for nc materials, it is critical to make comparisons with materials synthesized in similar

environment and the same method, in which a close grain boundary properties might be derived. In reality, it is difficult to investigate a nc materials systematically with grain sizes ranging from micrometers to several nanometers. A brief overview of mechanical properties for nc materials is listed below, which is not specifically limited to nc materials synthesized by exclusive one method.

C.2.1 Strength

It is well established in the conventional coarse-grained metals that yield stress σ_y for polycrystalline materials with grain size d follows

$$\sigma_y = \sigma_0 + \frac{k}{\sqrt{d}}, \tag{C.1}$$

the Hall-Petch relation named after Hall (1951) and Petch (1953), in which σ_0 is the Peierls frictional stress for huge single crystals and k being a material constant. Since nanocrystalline materials were first reported by Birringer et al. (1984) and subsequent improvement in their processing became possible, researchers have been driving the limit of such a relation by reducing grain size to several nanometers, from which tremendous increasing of strength is expected if such a relation holds for grain size in that range. Most experiments, with averaged grain sizes down to tens of nanometers, have confirmed the validity of the Hall-Petch relation. The slope does departure from the Hall-Petch relationship when the grain size decreases to a certain critical value. For grain sizes below a certain value, about 10nm for the case of nc nickel shown in Fig. C-4, there is a softening for strength or a negative slope in the Hall-Petch plot[1]. While Chokshi et al. (1989) argued the negative Hall-Petch effect observed on their nc Cu and Pd samples made by Inert gas consolidation to diffusional creep, others attribute this softening trend to the presence of pre-existing flaws, such as impurities and porosity introduced during the processing of nanocrystalline materials. Indeed, if diffusion at room temperature is the dominant mechanism which accounts for the

[1]In the plot, for tests conducted by hardness measurement, Tabors law (Tabor, 1951) has been applied to estimate the corresponding yield strength which is approximately equal to one third of the hardness.

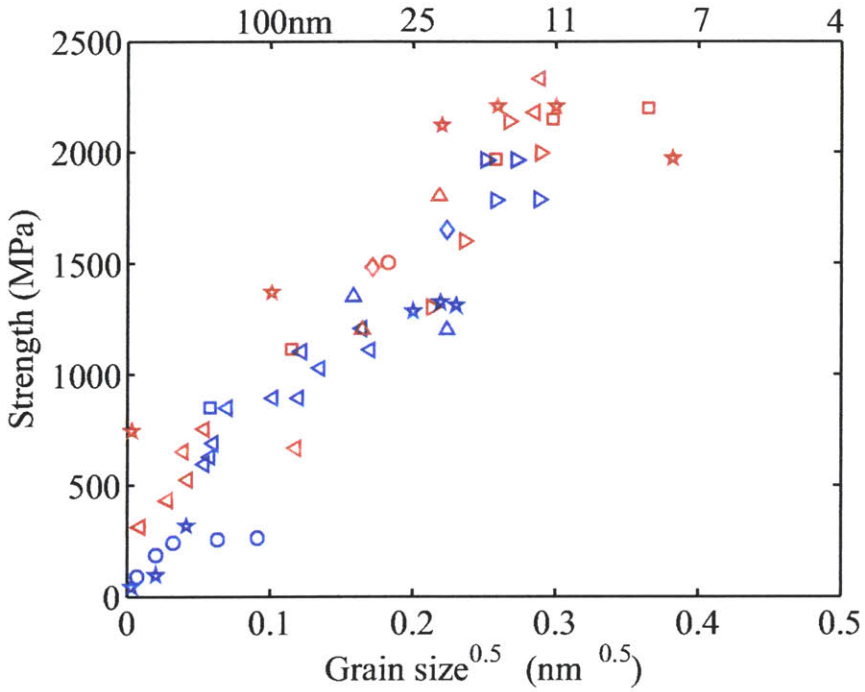

Figure C-4: Compiled yield strength versus grain size for f.c.c. Nickel from various sources ranging from conventional coarse grains to nanosized grains. The slope for Nickel fits quite well till a grain size down to about 12 nm.

□	El-Sherik et al. (1992)	□	Gray et al. (1997)
◁	Hughes et al. (1986)	◁	Ebrahami et al. (1999)
▷	Shuh et al. (2002)	▷	Torre et al. (2002)
△	Torre et al. (2005)	△	Wang et al. (1997)
★	Erb (1995)	★	Xiao et al. (2001)
○	Yin and Whang (2001)	○	Thompson (1975)
◇	Schwaiger et al. (2003)	◇	Zhu et al. (2005)

softening behavior observed in nc materials, a high strain rate sensitivity $m \approx 1$ is expected. m, the strain rate sensitivity parameter, is defined as

$$m = \frac{\partial \ln \sigma}{\partial \ln \dot{\epsilon}}. \tag{C.2}$$

Thus, the limit $m \to 0$ renders the case of flow stress being *rate-independent* and $m \to 1$ describes a Newtonian viscous flow rule. So far, for strain rates in the range of $10^{-6} - 10^{3}/s$ at room temperature, there is no experimental report on such a high strain rate dependence.

C.2.2 Strain-rate dependence

Even though a strain rate sensitive parameter $m \rightarrow 1$ has never been observed in nc materials at room temperature, an enhanced rate sensitivity behavior has been reported in f.c.c. nc materials, Fig. C-5 and h.c.p. nc magnesium, Fig. C-6 The pro-

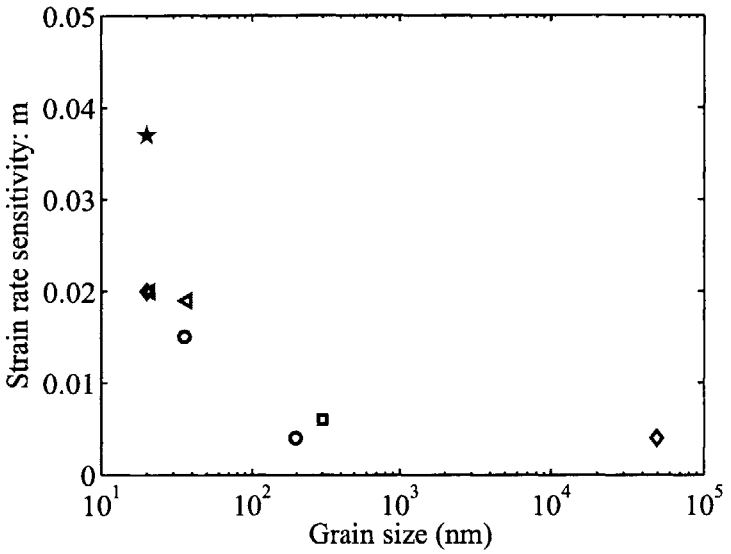

Figure C-5: Compiled strain rate sensitivity m versus grain size for f.c.c. Nickel from various sources ranging from hundreds of microns to nanosized grains. □ Gray et al. (1997); ◊ Torre et al. (2002); ◁ Torre et al. (2005) ○ Schwaiger et al. (2003) ★ Zhu et al. (2005).

found increasing strain rate sensitivity in f.c.c. and h.c.p. in nc materials is rationalized by the decrease in activation volume in nc regime. The dimensionless strain-rate sensitivity parameter m is suggested to be associated with activation volume v in the fashion of (Conrad, 1965; Wei et al., 2004a; Asaro and Suresh, 2005):

$$m = \frac{\sqrt{3}KT}{\sigma v}, \tag{C.3}$$

where K is the Boltzman constant, T the absolute temperature, and σ being the uniaxial flow stress. The activation volume for coarse grained f.c.c. metals is about several hundred to thousand, in unit of b^3, for b being the Burger's vector. It will reduce to be about $10 \sim 20$ as grain size reduces to tens of nanometer. For b.c.c. metals, instead of enhanced strain-rate sensitivity as grain size reduces, m decreases

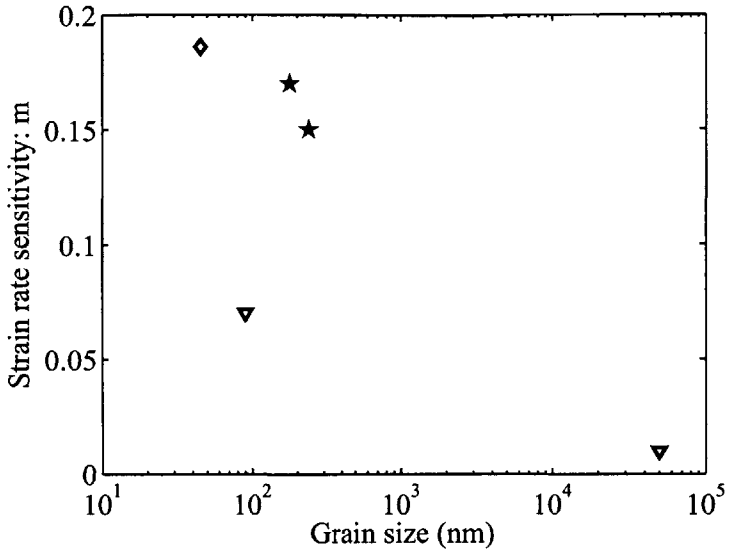

Figure C-6: Compiled strain rate sensitivity m versus grain size for h.c.p. Magnesium from various sources ranging from hundreds of microns to nanosized grains. ◊ Hwang et al. (2001); ▽ Wei and Anand (2006); ★ Zhang et al. (2002).

as grain size decreases, as shown in Fig. C-7. Even though the activation volume in b.c.c. metals is already low in the conventional grain-sized regime, the reduced strain-rate sensitivity at nano-grained regime for b.c.c. metals is not well understood. Obviously, grain boundary creep shouldn't be the dominant deformation mechanism in b.c.c. nc materials since it will give rise to enhanced strain-rate sensitivity as grain size becomes smaller.

C.2.3 Ductility

When grain size reduces to the nanoscale, one might expect a ductility increase if grain boundary diffusion is going to be the dominant inelastic deformation mechanism. In that case, a sufficiently large m is expected and could delay the onset of necking according to the Hart's criterion for a rate-sensitive material (Hart 1967; Wang and Ma 2004)

$$\frac{1}{\sigma}\left(\frac{\partial\sigma}{\partial\epsilon}\right)_{\dot{\epsilon}} - 1 + m \leq 0. \tag{C.4}$$

Therefore, tensile ductility is expected to improve correspondingly. However, a reduced ductility of $< 10\%$ for most f.c.c. and b.c.c. nc materials with grain size < 50

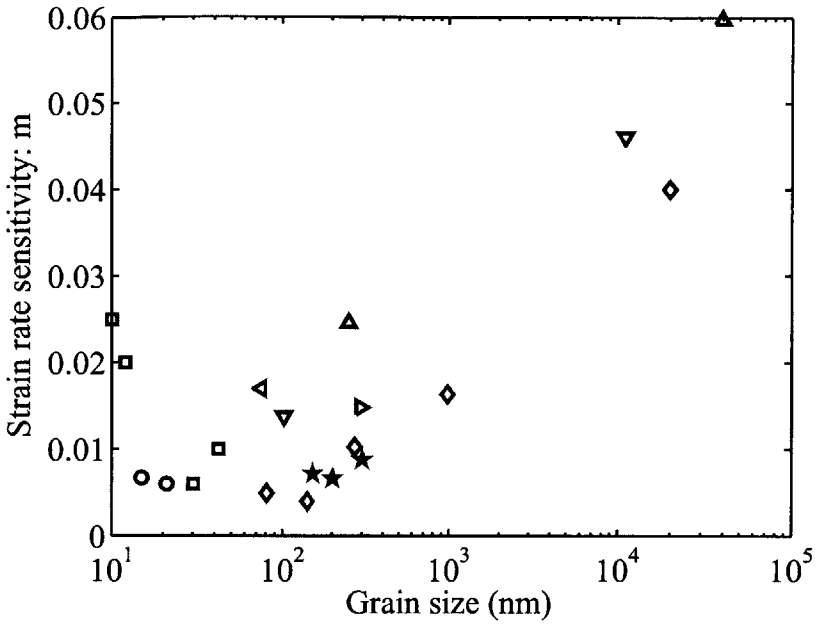

Figure C-7: Compiled strain rate sensitivity m versus grain size for b.c.c. Iron from various sources ranging from hundreds of microns to nanosized grains.

□	Jang and Atzmon (2003)	◊	Jia et al. (2003)
◁	Khan et al. (2000)	○	Malow and Koch (1998)
▷	Wei et al. (2004c)	★	Wei et al. (2004a)
△	Wei et al. (2003)	▽	Wei et al. (2004b)

nm is obtained while their conventional grain sized counterparts have tensile ductilities of $> 30\%$. For the moment, most ploycrystalline materials with grain size in the nanoscale deform inelastically by profuse inhomogeneous deformation in tension, either by necking or while deforming by a distributed cracking of grain-boundaries which are dominantly oriented perpendicular to the maximum principle tensile stress direction. In the tensile stress-strain curves, stresses harden and reach peaks quickly at low strains, then soften and fail at a relative low ductility. As to the stress-strain curves of those materials in compression, the stresses usually harden and then might soften at a certain amount of strain. After that, the stresses keep at a steady flow stress level without failure till a quite large amount of plastic deformation. It is of significance to improve the coherence of grain boundary to prevent premature failure behavior of nc materials in tension. Recent work by (Lu et al., 2004b, 2005) have shown that both ductility and strength could be improved dramatically by inducing

twinning boundaries in elelctrodeposited nc Cu.

Bibliography

Abaqus (2005). *Abaqus Reference Manuals.* Hibbit, Karlsson & Sorenson, Inc., Pawtucket, R.I.

Anand, L. (1980). Constitutive equations for rate-independent, isotropic elastic-plastic solids exhibiting pressure-sensitive yielding and plastic dilatancy. *J App Mech*, 47:439–441.

Anand, L. and Gurtin, M. E. (2003). A theory of amorphous solids undergoing large deformations, with applications to polymeric glasses. *Int. J. of Solids and Structures*, 40:1465–87.

Anand, L. and Kalidindi, S. R. (1994). The process of shear band formation in plane strain compression of fcc metals: effects of crystallographic texture. *Mechanics of Materials*, 17:223–43.

Anand, L. and Kothari, M. (1996). A computational procedure for rate-independent crystal plasticity. *Journal of the Mechanics and Physics of Solids*, 44:525–558.

Anand, L. and Su, C. (2005). A theory for amorphous viscoplastic materials undergoing finite deformations, with application to metallic glasses. *J. Mech. Phys. Solids*, 53:1362–96.

Asaro, R. J. (1983). Micromechanics of Crystals and Polycrystals. *Advances in Applied Mechanics*, 23:1–115.

Asaro, R. J., Krysl, P., and Kad, B. (2003). Deformation mechanism transitions in nanoscale FCC metals. *Philos. Mag. Lett.*, 83:733–43.

Asaro, R. J. and Needleman, A. (1985). Texture development and strain hardening in rate dependent Polycrystals. *Acta Metallurgica*, 33:923–953.

Asaro, R. J. and Suresh, S. (2005). Mechanistic models for the activation volume and rate sensitivity in metals with nanocrystalline grains and nano-scale twins. *Acta Mater.*, 53:3369–82.

Barenblatt, G. I. (1959). The formation of equilibrium cracks during brittle fracture: general ideas and hypotheses, axially symmetric cracks. *Applied Mathematics and Mechanics (PMM)*, 23:622–636.

Birringer, R., Gleiter, H., Klein, H. P., and Marquardt, P. (1984). Nanocrystalline materials: an approach to a novel solid structure with gas-like disorder? *Phys. Lett.*, 102A:365–9.

Bronkhorst, C. A., Kalidindi, S. R., and Anand, L. (1992). Polycrystalline plasticity and the evolution of crystallographic texture in FCC metals. *Philosophical transactions of the Royal Society of London A*, 341:443–477.

Camacho, G. T. and Ortiz, M. (1996). Computational modeling of impact damage in brittle materials. *International Journal of Solids and Structures*, 33:2899–2938.

Chen, M. W., Ma, E., Hemker, K. J., Sheng, H. W., Wang, Y. M., and Cheng, X. M. (2003). Deformation twinning in nanocrystalline aluminum. *Science*, 300:1275–77.

Cheng, S., Ma, E., Wang, Y. M., Kecskes, L. J., Youssef, K. M., Koch, C. C., Trociewitz, U. P., and Han, K. (2005). Tensile properties of in situ consolidated nanocrystalline cu. *Acta Materialia*, 53:1521–33.

Chokshi, A. H., Rosen, A., Karch, J., and Gleiter, H. (1989). On the validity of the HallPetch relationship in nanocrystalline materials. *Script. Metall.*, 23:1679–84.

Conrad, H. (1965). The cryogenic properties of metals. In Zackey, V. F., editor, *High Strength Materials*, pages 436–509. John Wiley & Sons, New York,.

Deng, D., Argon, A. S., and Yip, S. (1989). Simulation of plastic deformation in a two-dimensional atomic glass by molecular dynamics iv. *Philos. Trans. Roy. Soc. A*, 329:613–640.

Derlet, P. M. and Van Swygenhoven, H. (2002). The Role Played by Two Parallel Free Surfaces in the Deformation Mechanism of Nanocrystalline Metals: a Molecular Dynamics Simulation. *Philosophical Magazine A*, 82:1–15.

Dugdale, D. S. (1960). Yielding of steel sheets containing slits. *Journal of the Mechanics and Physics of Solids*, 8:100–104.

Duskardt, R. H., Lane, M., Ma, Q., and Krishna, N. (1998). Adhesion and debonding of multilayer thin-film structures. *Engineering Fracture Mechanics*, 61:141–162.

Ebrahami, F., Bourne, G. R., Kelly, M. S., and Matthews, T. E. (1999). Mechanical Properties of Nanocrystalline Nickel Produced by Electrodeposition. *Nanostructured Materials*, 11:343–350.

Ebrahami, F., Zhai, Q., and Kong, D. (1998). Deformation and Fracture of Electrodeposited Copper. *Scripta Materialia*, 39:315–321.

El-Sherik, A. M. and Erb, U. (1995). Synthesis of bulk nanocrystalline nickel by pulsed electrodeposition. *Journal of Materials Science*, 30:5743–9.

El-Sherik, A. M., Erb, U., Palumbo, G., and Aust, K. T. (1992). Deviations from Hall-Petch behavior in as-prepared nanocrystalline nickel. *Scripta Metall. Mater.*, 27:1185–8.

Erb, U. (1995). Electrodeposited nanocrystals: Synthesis, properties and industrial applications. *Nanostructured Materials*, 6:533–8.

Erb, U., Aust, K. T., and Palumbo, G. (2002). Electrodeposited Nanocrystalline Materials. In Koch, C. C., editor, *Nanocrystalline Materials - Processing, Properties and Potential Applications*, pages 179–222. William Andrew Publishing, Noyes.

Erb, U., El-Sherik, A. M., Palumbo, G., and Aust, K. T. (1993). Synthesis of bulk nanocrystalline nickel by pulsed electrodeposition. *Nanostruct. Mater.*, 2:383.

Farkas, D., Petegem, S. V., Derlet, P. M., and Van Swygenhoven, H. (2005). Dislocation activity and nano-void formation near crack tips in nanocrystalline ni. *Acta Materialia*, 53:3115–3123.

Farkas, D., Van Swygenhoven, H., and Derlet, P. M. (2002). Intergranular fracture in nanocrystalline metals. *Physical Review B*, 66:060101–1–4.

Fu, H. H., Benson, D. J., and Meyers, M. A. (2001). Analytical and computational description of effect of grain size on yield stress of metals. *Acta Materialia*, 49:2567–82.

Fu, H. H., Benson, D. J., and Meyers, M. A. (2004). Computational description of nanocrystalline deformation based on crystal plasticity. *Acta Materialia*, 52:4413–25.

Gleiter, H. (1989). Nanocrystalline materials. *Progress in Materials Science*, 33:223–315.

Gray, G. T., Lowe, T. C., Cady, C. M., Valiev, R. Z., and Aleksandrov, I. V. (1997). Influence of strain rate & temperature on the mechanical response of ultrafine-grained cu, ni and ai-4cu-0.5zr. *Nanostructured Materials*, 9:477–480.

Gross, D. and Li, M. (2002). Constructing microstructures of poly- and nanocrystalline materials for numerical modeling and simulation. *Applied Physics Letters*, 80:746–748.

Groza, J. R. (2002). Nanocrystalline powder consolidation methods. In Koch, C. C., editor, *Nanocrystalline Materials - Processing, Properties and Potential Applications*, pages 115–178. William Andrew Publishing, Noyes.

Hall, E. O. (1951). The deformation and aging of mild steel: III. Discussion of results. *Proc. Phys. Soc. London B*, 64:747–753.

Hart, E. W. (1967). Theory of the Tensile Test. *Acta Metall.*, 15:351–5.

Hill, R. (1965). Continuum Micro-Mechanics of Elastoplastic Polycrystals. *Journal of the Mechanics and Physics of Solids*, 13:89–101.

Hirth, J. P. and Lothe, J. (1992). *Theory of Dislocations*. Krieger Publishing, Malabar, UK, 2 edition.

Hughes, G. D., Smith, S. D., Pande, C. S., Johnson, H. R., and Armstrong, R. W. (1986). Hall-Petch strengtheningfor the microhardness of twelve nanometer grain diameterelectrodeposited nickel. *Scripta Metall.*, 20:93–97.

Hutchinson, J. W. and Evans, A. G. (2000). Mechanics of materials: top-down approaches to fracture. *Acta Materialia*, 48:125–135.

Hwang, S., Nishimura, C., and McCormick, P. G. (2001). Deformation mechanism of Nanocrystalline Magnesium in Compression. *Scripta mater.*, 44:1507–11.

Iwahashi, Y., Furukawa, M., Horita, Z., Nemoto, M., and Langdon, T. G. (1998). Microstructural characteristics of ultrafine-grained Aluminum produced using Equal-Channel Angular Pressing. *Metallurgical and Materials Transactions A*, 29A:2245–52.

Jang, D. and Atzmon, M. (2003). Grain-size dependence of plastic deformation in nanocrystalline Fe. *Journal of Applied Physics*, 93:9282–6.

Jeong, D. H., Gonzalez, F., Palumbo, G., Aust, K. T., and Erb, U. (2001). The Effect of Grain Size on the Wear Properties of Electrodeposited Nanocrystalline Nickel Coatings. *Scripta Materialia*, 44:493–499.

Jia, D., Ramesh, K. T., and Ma, E. (2003). Effects of nanocrystalline and ultrafine grain sizes on constitutive behavior and shear bands in iron. *Acta Materialia*, 51:3495–3509.

Kafkalidis, M. S. and Thouless, M. D. (2002). The effects of geometry and material properties on the fracture of single-lap-shear joints. *International Journal of Solids and Structures*, 39:4367–4383.

Kalidindi, S., Bronkhorst, C., and Anand, L. (1992). Crystallographic texture evolution in bulk deformation processing of FCC metals. *Journal of the Mechanics and Physics of Solids*, 40:536–569.

Khan, A. S., Zhang, H. Y., and Takacs, L. (2000). Mechanical response and modeling of fully compacted nanocrystalline iron and copper. *Int. J. of Plasticity*, 16:1459–76.

Kröner, E. (1960). Allgemeine kontinuumstheorie der versetzungen und eigenspannungen. *Archive for Rational Mechanics and Analysis*, 4:273 – 334.

Kumar, K. S., Suresh, S., Chisolm, M. F., Horton, J. A., and Wang, P. (2003). Deformation of electodeposited nanocrystalline nickel. *Acta Materialia*, 51:387–405.

Lagerlöf, K. P. D., Castaing, J., Pirouz, P., and Heuer, A. H. (2002). Nucleation and growth of deformation twins: a perspective based on the double-cross-slip mechanism of deformation twinning. *Philos. Mag. A*, 82:2841–54.

Lane, M., Duskardt, R. H., Vainchtein, A., and Gao, H. (2000). Plasticity contributions to interface adhesion in thin-film interconnect structures. *Journal of Materials Research*, 15:2758–2769.

Lee, E. H. (1969). Elastic plastic deformation at finite strain. *ASME J. Appl. Mech.*, 36:16.

Legros, M., Elliot, B. R., Rittner, M. N., Weertman, J. R., and Hemker, K. J. (2000). Microsample Tensile Testing Of Nanocrystalline Metals. *Philosophical Magazine A*, 80:1017–26.

Lu, K., Wang, J. T., and Wei, W. D. (1991). A new method for synthesizing nanocrystalline alloys. *J. Appl. Phys.*, 69:522 – 524.

Lu, L., Lai, M. O., Tan, S. K., and Raviprasad, K. (2004a). Nanostructured high strength Mg-5%Al-x%Nd Alloys prepared by mechanical alloying. *Rev. Adv. Mater. Sci.*, 6:28–32.

Lu, L., Li, S. X., and Lu, K. (2001). An Abnormal Strain Rate Effect on Tensile Behavior in Nanocrystalline Copper. *Scripta Materialia*, 45:1163–9.

Lu, L., Schwaiger, R., Shan, Z. W., Dao, M., Lu, K., and Suresh, S. (2005). Nano-sized twins induce high rate sensitivity of flow stress in pure copper. *Acta Materialia*, 53:2169–79.

Lu, L., Shen, Y. F., Chen, X. H., Qian, L. H., and Lu, K. (2004b). Ultrahigh strength and high electrical conductivity in copper. *Science*, 304:4226.

Lu, L., Sui, M. L., and Lu, K. (2000). Superplastic Extensibility of Nanocrystalline Copper at Room Temperature. *Science*, 287:1463–6.

Lund, A. C., Nieh, T. G., and Schuh, C. A. (2004a). Tensioncompression strength asymmetry in a simulated nanocrystalline metal. *Physical Review B*, 69:012101–1.

Lund, A. C., Nieh, T. G., and Schuh, C. A. (2004b). Tensioncompression strength asymmetry in a simulated nanocrystalline metal. *Physical Review B*, 69:012101–1.

Malow, T. R. and Koch, C. C. (1998). Mechanical properties, ductility, and grain size of nanocrystalline iron produced by mechanical attrition. *Metallurgical and Materials Transactions A*, 29A:2285–95.

Mandel, J. (1965). Generalization de la theorie de la plasticite de W.T. Koiter. *International Journal of Solids and Structures*, 1:273–295.

Mandel, J. (1972). *Plasticite Classique et Viscoplasticite. CISM Courses and Lectures No. 97.* Springer-Verlag, Berlin.

McFadden, S. X., Mishra, R. S., Valiev, R. Z., Zhilyaev, A. P., and Mukherjee, A. K. (1999). Low-Temperature Superplasticity in Nanostructured Nickel and Metal Alloys. *Nature*, 398:684–6.

Meyers, M. A., Mishra, A., and Benson, D. J. (2006). Mechanical properties of nanocrystalline materials. *Porgress in Materials Science*, page in press.

Needleman, A. (1990). An analysis of decohesion along an imperfect interface. *International Journal of Fracture*, 40:21–40.

Nieman, G. W., Weertman, J. R., and Siegel, R. W. (1989). Microhardness of nanocrystalline palladium and copper produced by inert-gas condensation. *Scripta Metall.*, 23:2013–8.

Perez, R. J., Huang, B., and Lavernia, E. J. (1996). Thermal stability of nanocrystalline Fe-10 wt.cryogenic mechanical alloying. *Nanostr. Mater.*, 7:565–572.

Petch, N. J. (1953). The cleavage strength of polycrystals. *J. Iron Steel Inst*, 174:2528.

Ranganathan, S., Divakar, R., and Ragunathan, V. S. (2001). . *Scripta Materialia*, 44:1169.

Rawers, J., Slavens, G., Govier, D., Dogan, C., and Doan, R. (1996). Microstructure and tensile properties of compacted, mechanically alloyed nanocrystalline Fe-Al. *Met. Mater. Trans. A*, 27:3126–34.

Rice, J. R. (1971). Inelastic Constitutive Relations for Solids: An Internal Variable Theory and its Application to Metal Plasticity. *Journal of the Mechanics and Physics of Solids*, 19:433–455.

Rudnicki, J. W. and Rice, J. R. (1975). Conditions for the localization of deformation in pressure-sensitivity and dilatant materials. *Journal of the Mechanics and Physics of Solids*, 23:371.

Sanders, P. G., Eastman, J. A., and Weertman, J. R. (1997). Elastic and Tensile Behavior of Nanocrystalline Copper and Palladium. *Acta Materialia*, 45:4019–25.

Sansoz, F. and Molinari, J. F. (2004). Incidence of atom shuffling on the shear and decohesion behavior of a symmetric tilt grain boundary in copper. *Scripta Materialia*, 50:12838.

Schiøtz, J., Tolla, F. D. D., and Jacobsen, K. W. (1998). Softening of Nanocrystalline metals at Very Small Grain Sizes. *Nature*, 391:561–563.

Schiøtz, J., Vegge, T., Tolla, F. D. D., and Jacobsen, K. W. (1999). Atomic-Scale Simulations for the Mechanical Deformation of Nanocrystalline Metals. *Physical Review B*, 60:11971–83.

Schwaiger, R., Moser, B., Dao, M., Chollacoop, N., and Suresh, S. (2003). Some critical experiments on the strain-rate sensitivity of nanocrystalline nickel. *Acta Mater.*, 51:5159–72.

Segal, V. M., Reznikov, V. I., Drobyshevsky, A. E., and Kopylov, V. I. (1981). Hall-Petch Breakdown Manifested in Abrasive Wear Resistance of Nanocrystalline Nickel. *Russ. Metall.*, 1:99–105.

Shuh, C., Nieh, T. G., and Yamasaki, T. (2002). Hall-Petch Breakdown Manifested in Abrasive Wear Resistance of Nanocrystalline Nickel. *Scripta Materialia*, 46:735–740.

Simmons, G. and Wang, H. (1971). *Single Crystal Elastic Constants and Calculated Aggregate Properties.* The M.I.T. Press, Cambridge.

Staroselsky, A. and Anand, L. (1998). Inelastic deformation of fcc materials by slip and twinning. *Journal of the Mechanics and Physics of Solids*, 46:671–96.

Su, C. and Anand, L. (2006). Plane strain indentation of a zr-based metallic glass: Experiments and numerical simulation. *Acta Mater.*, 54:179–189.

Su, C., Wei, Y. J., and Anand, L. (2004). An elastic-plastic interface constitutive model: application to adhesive joints. *International Journal of Plasticity*, 20:2063–81.

Suryanarayana, C. (1995). Nanocrystalline Materials. *International Metallurgical Reviews*, 40:41–46.

Tabor, D. (1951). *The Hardness of Metals*. Oxford University Press, London.

Taylor, G. (1938). Plastic Strain in Metals. *Journal of the Institute of Metals*, 62:307–324.

Teodosiu, C. (1970). A dynamic theory of dislocations and its applications to the theory of the elastic-plastic continuum. In Simmons, J. A., de Wit, R., and Bullough, R., editors, *Proc Conf on Fundamental Aspects of Dislocation Theory*, page 837. National Bureau of Standards Special Publication, 2 edition.

Teodosiu, C. and Sidoroff, F. (1976). A theory of finite elastoviscoplasticity of single crystals. *International Journal of Engineering Science*, 14:165–176.

Thompson, A. (1975). Yielding in nickel as a function of grain or cell size. *Acta Metall.*, 23:1337–42.

Torre, F. D., Sp atig, P., Sch aublin, R., and Victoria, M. (2005). Deformation behaviour and microstructure of nanocrystalline electrodeposited and high pressure torsioned nickel. *Acta Materialia*, 53:2337–49.

Torre, F. D., Van Swygenhoven, H., and Victoria, M. (2002). Nanocrystalline electrodeposited Ni: microstructure and tensile properties. *Acta Materialia*, 50:3957–70.

Tvergaard, V. and Hutchinson, J. W. (1992). The relation between crack growth resistance and fracture process parameters in elastic-plastic solids. *Journal of The Mechanics and Physics of Solids*, 40:1377–1397.

Tvergaard, V. and Hutchinson, J. W. (1996). Toughness of ductile adhesive joints. *Journal of The Mechanics and Physics of Solids*, 44:789–800.

Valiev, R. Z., Korznikor, A. V., and Mulyukov, R. R. (1993). Structure and properties of ultrafine-grained materials produced by severe plastic deformation. *Mater. Sci. Eng A*, 168:141.

Valiev, R. Z., Kozlov, E. V., Ivanov, Y. F., Lian, J., Nazarov, A. A., and Baudelet, B. (1994). Deformation behaviour of ultra-fine-grained copper. *Acta Metall. Mater.*, 42:2467–75.

Valiev, R. Z. and Tsenev, N. K. (1991). In Langdon, T. G., Merchant, H. D., Morris, J. G., and Zaidi, M. A., editors, *Hot Deformation of Aluminum Alloys*, pages 319–329. TMS, Warrendale, PA.

Van Swygenhoven, H., Derlet, P. M., and Frseth, A. G. (2004). Stacking fault energies and slip in nanocrystalline metals. *Nature Materials*, 3:399–403.

Van Swygenhoven, H., Derlet, P. M., and Hasnaoui, A. (2002). Atomic Mechanism for Dislocation Emission from Nanosized Grain Boundaries. *Physical Review B*, 66:024101–1–8.

Van Swygenhoven, H., Spaczer, M., and Caro, A. (1998). Role of Low and High Angle Grain Boundaries in the Deformation Mechanism of Nanophase Ni: a Molecular Dynamics Simulation Study. *Nanostructured Materials*, 10:819–828.

Van Swygenhoven, H., Spaczer, M., and Caro, A. (1999a). Microscopic Description of Plasticity in Computer Generated Metallic Nanophase Samples: A Comparision between Cu and Ni. *Acta Materialia*, 47:3117–26.

Van Swygenhoven, H., Spaczer, M., Caro, A., and Farkas, D. (1999b). Competing Plastic Deformation Mechanisms in Nanophase Metals. *Physical Review B*, 60:22–25.

Van Vliet, K. J., Tsikata, S., and Suresh, S. (2003). Model experiments for direct visualization of grain boundary deformation in nanocrystalline metals. *Applied Physics Letters*, 83:1441–3.

Wang, N., Wang, Z. R., Aust, K. T., and Erb, U. (1997). Room temperature creep behavior of nanocrystalline nickel produced by an electrodeposition technique. *Materials Science and Engineering A*, 237:150–158.

Wang, Y. M. and Ma, E. (2004). Three strategies to achieve uniform tensile deformation in a nanostructured metal. *Acta Mater*, 52:1699–1709.

Warner, D. H., Sansoz, F., and Molinari, J. F. (2006). Atomistic based continuum investigation of plastic deformation in nanocrystalline copper. *Int. J. of Plasticity*, 22:754.

Weber, G. and Anand, L. (1990). Finite deformation constitutive equations and a time integration procedure for isotropic, hyperelastic-viscoplastic solids. *Computer Methods In Applied Mechanics and Engineering*, 79:173–202.

Wei, Q., Cheng, S., Ramesh, K. T., and E., M. (2004a). Effect of nanocrystalline and ultrafine grain sizes on the strain rate sensitivity and activation volume: fcc versus bcc metals. *Mater. Sci. Eng. A*, 381:71–79.

Wei, Q., Jiao, T., Mathaudhu, S. N., Ma, E., Hartwig, K. T., and Ramesh, K. T. (2003). Microstructure and mechanical properties of tantalum after equal channel angular extrusion (ECAE). *Mater. Sci. Eng. A*, 358:266.

Wei, Q., Jiao, T., Ramesh, K. T., and Ma, E. (2004b). Nano-structured vanadium: processing and mechanical properties under quasi-static and dynamic compression. *Scripta Mater.*, 50:359–364.

Wei, Q., Kecskes, L., Jiao, T., Hartwig, K. T., and Ramesh, K. T. (2004c). Adiabatic shear banding in ultrafine-grained Fe processed by severe plastic deformation. *Acta Mater.*, 52:1859–67.

Wei, Y. J. and Anand, L. (2004). Grain-boundary sliding and separation in polycrystalline metals: application to nanocrystalline f.c.c. metals. *Journal of the Mechanics and Physics of Solids*, 52:2587–2616.

Wei, Y. J. and Anand, L. (2006). A constitutive model for powder-processed nanostructured copper and magnesium. *Acta Mater.*, pages , submitted.

Wolf, D., Yamakov, V., Phillpot, S. R., Mukherjee, S. R., and Gleiter, H. (2005). Deformation of nanocrystalline materials by molecular-dynamics simulation: relationship to experiments? *Acta Materialia*, 53:1–40.

Xiao, C. H., Mirshams, R. A., Whang, S. H., and Yin, W. M. (2001). Tensile behavior and fracture in nickel and carbon doped nanocrystalline nickel. *Materials Science and Engineering A*, 301:35–43.

Xu, X. P. and Needleman, A. (1994). Numerical simulations of fast crack growth in brittle solids. *Journal of the Mechanics and Physics of Solids*, 42:1397–1434.

Yamakov, V., Wolf, D., Phillpot, S. R., and Gleiter, H. (2002). Grain-boundary diffusion creep in nanocrystalline palladium by molecular-dynamics simulations. *Acta Mater.*, 50:61–73.

Yamakov, V., Wolf, D., Phillpot, S. R., Mukherjee, A. K., and Gleiter, H. (2004). Deformation-mechanism map for nanocrystalline metals by molecular-dynamics simulation. *Nature Materials*, 3:43–47.

Yamakov, V., Wolf, D., Salazar, M., Phillpot, S. R., and Gleiter, H. (2001). Length-scale effects in the nucleation of extended dislocations in nanocrystalline Al by molecular-dynamics simulation. *Acta Materialia*, 49:2713–22.

Yang, Q. D. and Thouless, M. D. (2001). Mixed-mode fracture analysis of plastically deforming adhesive joints. *International Journal of Fracture*, 110:175–187.

Yang, Q. D., Thouless, M. D., and Ward, S. M. (1999). Numerical simulation of adhesively-bonded beams failing with extensive plastic deformation. *Journal of The Mechanics and Physics of Solids*, 47:1337–53.

Yang, Q. D., Thouless, M. D., and Ward, S. M. (2000). Analysis of the symmetrical 90-degree peel test with extensive plastic deformation. *Journal of Adhesion*, 72:115–132.

Yin, W. M. and Whang, S. H. (2001). Creep in Boron-doped nanocrystalline nickel. *Scripta Materialia*, 44:569–574.

Yip, S. (2004). Nanocrystalline metals: Mapping plasticity. *Nature Materials*, 3:11–12.

Yoshizawa, Y., Oguma, S., and Yamauchi, K. (1988). New Fe-based soft magnetic alloys composed of ultrafine grain structure. *J. Appl Phys.*, 64:6044–6.

Youssef, K. M., Scattergood, R. T., Murty, K. L., and Koch, C. C. (2004). Ultratough nanocrystalline copper with a narrow grain size distribution. *Applied Phys. Lett*, 85:929–931.

Zhang, X., Wang, H., Scattergood, R. O., Narayan, J., Koch, C. C., V., S. A., and Mukherjee, A. K. (2002). Studies of deformation mechanisms in ultra-fine-grained and nanostructured Zn. *Acta Materialia*, 50:4823–30.

Zhu, B., Asaro, R. J., Krysl, P., and Bailey, R. (2005). Transition of deformation mechanisms and its connection to grain size distribution in nanocrystalline metals. *Acta Mater.*, 53:4825–38.